

Thesis for the Degree
of Doctor

Measurement of Sea - Quark Polarization for Proton
in $W/Z \rightarrow \mu^\pm$ Production
Using Longitudinally Polarized p + p Collisions
at $\sqrt{s} = 510$ GeV

by

Chong KIM

Department of Physics

Graduate School

Korea University

June 2015

洪炳軾 教授指導

博士學位論文

Measurement of Sea-Quark Polarization for Proton
in $W/Z \rightarrow \mu^\pm$ Production

Using Longitudinally Polarized p + p Collisions
at $\sqrt{s} = 510$ GeV

이 論文을 物理學 博士學位 論文으로 提出함

2015年 6月 2日

高麗大學校大學院

物理學科

金 聰 (印)

金聰의 物理學 博士學位論文 審查를 完了함

2015年 6月 2日

委 員 박 인규 (印)

委 員 안정근 (印)

Abstract

The flavor-separated spin contributions of quarks and anti-quarks to the proton yet have large uncertainties mostly originated from the fragmentation functions. The parity violating W production in the polarized proton collisions can provide stringent constraints on these uncertainties. Since only the left-handed quarks and the right-handed anti-quarks can produce W , the complete flavor-separation can be possible. In addition, the analysis results are independent of the fragmentation functions as the leptons are directly decayed from W . To estimate the longitudinal spin contributions of quarks and anti-quarks to the proton spin, the longitudinal single spin asymmetry (A_L) has been measured by using the high-transverse momentum (p_T) muons. The W^\pm/Z bosons are produced from the polarized proton collisions at $\sqrt{s} = 510$ GeV at RHIC. The dataset accumulated during the 2012 PHENIX Run has been used. During the data taking, the average beam polarizations were 0.536 ± 0.041 and 0.574 ± 0.043 , respectively, for each beam. The total integrated luminosity was 53.1 pb^{-1} . The muon candidates were selected by using the PHENIX Muon Arms, covering the acceptance of $1.2 < \eta < 2.2$ for south and $1.2 < \eta < 2.4$ for north with η the pseudorapidity in full azimuth. Only the muon candidates with $16 < p_T < 60$ GeV/c were further analyzed for effective background reduction. The final longitudinal single spin asymmetries for W^\pm/Z were determined as follows:

$$\begin{aligned} A_L^{\mu^-} (\text{FW}) &= 0.096 {}^{+0.445}_{-0.449} \text{ (stat)} \pm 0.079 \text{ (syst)} & \langle \eta \rangle &= 1.76 \\ A_L^{\mu^-} (\text{BW}) &= -0.057 {}^{+0.429}_{-0.436} \text{ (stat)} \pm 0.140 \text{ (syst)} & \langle \eta \rangle &= -1.76 \\ A_L^{\mu^+} (\text{FW}) &= 0.252 {}^{+0.324}_{-0.332} \text{ (stat)} \pm 0.193 \text{ (syst)} & \langle \eta \rangle &= 1.73 \\ A_L^{\mu^+} (\text{BW}) &= -0.086 {}^{+0.302}_{-0.303} \text{ (stat)} \pm 0.062 \text{ (syst)} & \langle \eta \rangle &= -1.73 \end{aligned}$$

Contents

Abstract

Contents	i
List of Figures	iii
List of Tables	ix
1 Introduction	1
1.1 Composition of the thesis	1
1.2 Physics Motivation	2
1.2.1 Structure of the Proton	2
1.2.2 Probing Sea Quark Polarization in p + p Collisions	4
2 Apparatus	11
2.1 RHIC	11
2.1.1 Beam Acceleration	11
2.1.2 Beam Polarization	13
2.2 PHENIX	19
2.2.1 Overview	19
2.2.2 Subsystems	22
2.3 Data Acquisition	35
2.3.1 DAQ System	35
2.3.2 Triggers	37
2.3.3 Track Reconstruction	44
3 Dataset	45
3.1 Overview	45
3.2 Integrated Luminosity	46
3.3 Hit Efficiency	48

3.3.1	MuID	48
3.3.2	MuTr	50
3.3.3	RPC	52
3.4	Trigger Efficiency	54
4	Analysis	55
4.1	Overview	55
4.2	Signal Extraction	58
4.2.1	Analysis Variables	58
4.2.2	Type of Muon Candidates	62
4.2.3	Backgrounds Filtering	72
4.2.4	Overall trigger efficiency	85
4.2.5	Signal to Backgrounds Estimation	93
4.3	Single Spin Asymmetry Estimation	103
4.3.1	Introduction	103
4.3.2	A_L Estimation	107
4.3.3	Systematic Uncertainties	114
4.3.4	Results	122
4.4	Discussion and Conclusion	125
4.4.1	Discussion	125
4.4.2	Conclusion	127
Bibliography		128
Acknowledgement		

List of Figures

1.1	Results of global fit by DSSV group. [1]	3
1.2	Production and decay of W^+ (left) and W^- (right) with its helicity	6
1.3	W^+ production in polarized $p + p$. In this case u is being probed. The colored superscript sign of u and \bar{d} indicates corresponding quark or anti-quark's helicity while The colored subscript sign of u indicates helicity of the beam.	8
1.4	W^+ production in polarized $p + p$, In this case \bar{d} is being probed. Same notation to the Fig. 1.3 holds for the colored superscripts and subscripts.	8
1.5	Results of DSSV global fit for $\Delta\bar{u}$ (x, Q^2) and $\Delta\bar{d}$ (x, Q^2) at $Q^2 = 10$ GeV 2 before (top) and after (bottom) adding the replica of the RHIC W results. The total integrated luminosity of the replica is 200 pb $^{-1}$ [2].	10
2.1	RHIC accelerator complex [3]	12
2.2	180° flip in polarization direction by a full Siberian Snake [4].	14
2.3	Positions of Siberian Snakes and Spin Rotators in RHIC [5]	15
2.4	A_N for pC (left) and pC/pp (right) elastic scattering in the CNI re- gion. Left figure shows actual measurement result with 21.7 GeV proton beam at AGS (left) [6] while Right figure shows calculated dis- tributions for a carbon ($Z = 6, \sigma_{tot} = 330$ mb) and proton ($Z = 1, \sigma_{tot}$ $= 35$ mb) target with 250 GeV proton beam [5].	16
2.5	Geometrical layout of Local polarimeter (ZDC, SMD) at PHENIX [7]	18
2.6	Cartesian coordinates at PHENIX	19
2.7	Geometrical acceptance of PHENIX detector system	20
2.8	Layout of PHENIX detectors in 2012. Central Arms in the beam view (top) and Muon Arms in the sideview (bottom)	21

2.9	A BBC supermodule's picture (left) and its layout in beam view (right). A couple of blank circles in layout's middle layer indicate the positions of laser sources for calibration.	24
2.10	3D layout (left) and a picture (right) of the completed half-detector of combined FVTX/VTX.	25
2.11	Sideview of PHENIX magnets. The dumbbell shaped structure in center is the Central Magnet and two truncated cone shaped structures in left and right are the Muon Magnets. The tapered pillar like structure inside Muon Magnet indicates Muon Piston.	26
2.12	Structure of a MuID <i>panel</i> composed of a pair of <i>two-packs</i> (top) and Cross section of a <i>two-pack</i> (bottom).	27
2.13	Structure of the MuID in beam view with <i>panel</i> numbering scheme (top)[8] and Structure of the MuID in sideview with <i>gap</i> numbering scheme (bottom)[7]. The numbering of the <i>gaps</i> start from 1 and increases with distance from the collision vertex. The hatched materials in sideview indicate steel wall absorbers. The bottom figure is quoted from [7].	28
2.14	Schematic diagrams MuTr. Left figure shows whole MuTr South and Right figure shows <i>quadrants (half octants)</i> structure of MuTr St.1	29
2.15	Alternating structure of the anode plane (left) and <i>non-stereo/stereo</i> structure of the cathode planes (right). The black lines indicate <i>non-stereo</i> plane and the blue lines indicate <i>stereo</i> plane. These figures are quoted from [7].	30
2.16	Cross-sectional layout of a RPC module.	32
2.17	Layout of RPC1 and RPC3 in sideview. RPC3's ring-like structure with different colors indicates 3 different types of module of RPC3 (ex. innermost green ring indicates <i>RPC3A</i>).	33
2.18	Mechanical desing of the ZDC: a layer of optical fibers (top), sideview of a hadronic calorimeter module (bottom left), and beam view of a hadronic calorimeter module (bottom right), respectively. All units are mm. This plot is quoted from [9].	34
2.19	Data acquisition process	36
2.20	Schematic diagram of ERT triggers	39
2.21	Example of MuID <i>symsets</i> . The tubes (<i>two-packs</i>) along same <i>symset</i> share same index (ex. <i>a</i> , <i>z</i> , <i>t</i> , <i>l</i>).	40
2.22	Logic diagram of MuID1D (top) and MuID1H (bottom). Note that the number of each diagram indicates MuID gaps (ex. 0 for gap 1).	41
2.23	Signal process of MuTRG-FEE.	42
2.24	Schematic diagrams of MuTRG trigger	43

3.1	Integrated luminosity (left) and its Figures of Merit (right) in Run 12 [10]	45
3.2	HV groups of horizontal <i>plane</i> (left) and vertical <i>plane</i> (right) of MuID. A large <i>plane</i> has 3 HV groups and A small <i>plane</i> has 2 groups. This plot is quoted from [8].	49
3.3	Hit efficiency of MuID south <i>gap</i> 0 horizontal <i>plane</i> vs. BBC rate (MHz). Each histogram corresponds to the HV group in the position. This plot is quoted from [8].	49
3.4	<i>run</i> by <i>run</i> p_1 (top left) and p_2 (top right) of MuTr vs. BBC rate (MHz) and Correlation between <i>gap</i> efficiency and <i>plane</i> efficiency (bottom). The Blue solid line indicates full correlation between two efficiencies while The Blue dashed line indicates no correlation. Red dots indicates MuTr south and Black dots indicate MuTr north. These plots are quoted from [8].	51
3.5	RPC efficiencies for unlike-sign events (top) and like-sign events (middle and bottom). Each column shows results of RPC3 south (left) and north (right).	53
4.1	p_T vs. η distribution of leptons from W^- (left) and W^+ (right). The bottom left plot shows the projections vs. p_T in $ \eta < 1.0$ and The bottom right plot shows the projections vs. p_T in $1.2 < \eta < 3.0$. Color of dashed lines indicate charge of the leptons (green for positive, red for negative). This plot is quoted from [11].	56
4.2	Schematic diagrams of analysis variables. The numbers at the bottom of the Top figure indicate accumulated nuclear interaction length of south (north) Muon Arm. Polar angle (θ) in bottom right indicates particular condition for dw_{23} . Note that not all analysis variables are displayed.	60
4.3	Several frequently used kinematic variables' distributions by each type of muon candidate. All MC distributions are a sum of multiple processes. Especially signal and muonic BG distribution is obtained under <i>high</i> multiple collision condition. Note that each sample is arbitrary scaled for the comparison. These distributions are obtained from south, negative charged muons.	61
4.4	Real muon cross sections from Pythia Tune A with k factor of 1.5. All subprocess displayed individually (top) or stacked (bottom), for negative charge (left) or positive charge (right). This plot is quoted from [11].	63

4.5 Hadron cross sections of π^\pm and K^\pm based on UA1 experiment (red continuous lines) and NLO perturbative QCD calculations (blue continuous lines), displayed individually (top) or stacked (bottom) for negative charge (left) or positive charge (right). Hadrons from muonic subprocesses in Table 4.2 are displayed as well. This plot is quoted from [11].	66
4.6 Stacked cross sections including both muonic and hadronic processes, after 1st backgrounds filtering by <i>Basic cut</i> in section 4.2.3. Each subprocess scaled to the luminosity of the data. Note that $Z \rightarrow \mu$ process subtracted from Z/DY to prevent double counting.	70
4.7 Stacked cross sections with same condition to previous Fig. 4.6 including p_T range. Some kinematic variables from south, negative muons are selectively displayed but the other conditions (side, charge or variable) also show reasonable match as well.	71
4.8 Distributions (left) and Efficiencies (right) of $Wness$ for all three types of muon candidates. Note that MC distributions for certain type of muon candidates are a stack of multiple subprocess after luminosity scaling. Especially for muonic backgrounds additional scaling factors in later section 4.2.5 are applied as well. All multiple collision conditions are considered by using the fractions in Table 4.4.	75
4.9 Fraction of each multiple collision condition in the data after <i>2nd filtering</i> . Left plot shows number of events and Right plot shows their fraction to the whole.	76
4.10 Normalized yields of W MC with different multiple collision condition (left) and Its efficiency versus $Wness$ (right).	77
4.11 Example of <i>Significance</i> test by using signal MC and backgrounds MC for each multiple collision condition. Left plot shows results versus muonic backgrounds and Right plot shows results versus hadronic backgrounds.	78
4.12 $Hness$ vs. $Wness$ for data (left), signal MC (middle), and hadronic MC (right). Each MC is scaled by luminosity. Hadronic MC is a sum of all subprocesses and p_T bins.	80
4.13 Finding optimal $Hness$ cut by using signal MC. Left column shows signal MC distributions vs. $Hness$ with $Wness > 0.92$ condition and Right column shows its efficiency vs. $Hness$. Dashed lines in right column indicate $Hness$ for 5 % signal efficiency.	81

4.14 Optimal H_{ness} vs. W_{ness} for each Arm and Charge. Each colored lines indicate optimal H_{ness} for each multiple collision condition and A black line indicates multiple collision fraction weighted final optimal H_{ness}	82
4.15 Distributions (left) and Efficiencies (right) of H_{ness} for all three types of muon candidates. The other conditions are same to Fig. 4.8.	84
4.16 Number of triggers simultaneously fired for an event, for south (left) and north (right). The pattern is similar to the positive charged muon candidates as well.	86
4.17 $ \eta $ acceptance of 50 trigger combination. The black filled boxes indicate each trigger combination's effective acceptance and The dashed lines at 1.0 or 2.6 indicate physical limit of reconstructed tracks. Blank columns mean there's no event fired by corresponding trigger combination in the $W_{ness} > 0.1$ condition.	88
4.18 Example of the estimation procedures for a trigger combination's efficiency at <i>Tight candidates</i> . First five turn-on plots show extraction of plateau efficiency vs. p_T for each W_{ness} window. Bottom linear plot shows linear fit on plateau efficiencies and its 1σ CL extrapolation. Both p_T and W_{ness} windows set arbitrary to acquire enough statistics.	90
4.19 Results of $\epsilon_{trig,OA}$ estimation by using ERT sample. trigger combination with no efficiency point means its fraction in <i>Final candidate</i> is 0.	92
4.20 Distributions of fit variables in <i>Tight candidates</i> condition. Each row shows different type of muon candidates: data, signal MC, muonic backgrounds MC and hadronic backgrounds MC, respectively. The 2nd and 3rd column is a projection of 1st column's distribution onto each variable. Note that all MC is a stack of related subprocesses after scaling.	94
4.21 Final di-muon fit results by Sanghwa Park. Left column shows low mass region triggered by MUID1D (MU1D) and Right column shows high mass region by R12W1 (SG1D). This plot is quoted from [11].	98
4.22 Unbinned maximum likelihood fit on data at $W_{ness} > 0.92$ and optimal H_{ness} . Each plot indicates a 2D fit's projection onto η (left) or dw_{23} (right). The dashed lines in dw_{23} projections indicate sidebands cut condition.	100
4.23 NLL contours of the unbinned max. likelihood fit in Fig. 4.22. Solid, Dashed, and Dotted line indicates 1σ , 2σ , and 3σ deviataion, respectively.	101
4.24 Map of the Spin patterns	103

4.25 Statistical fraction under <i>Tight candidates</i> condition and Polarization of each beam.	107
4.26 Pileup corrected BBC _{noVtx} yields by Spin pattern. Left plot shows raw yields and Right plot shows scaled yields by 1/(total yields \times 0.25).	108
4.27 Parameters of the <i>Wness</i> scan for each Arm and Charge. Left column shows number of muon candidates (scaled) and its average $ \eta $ and Right column shows S/BG ratio, $\epsilon_{L,B}$, $\epsilon_{L,Y}$, and ϵ_{LL} , repectively.	110
4.28 Results of the <i>Wness</i> scan for each Arm and charge. Left column shows A_L of both beams with combined error in Eq. 4.20and Right column shows FoM defined by Eq. 4.21. Note that systematic uncertainties are not included in the combined errors.	111
4.29 EUML fit results for the conditions at maximum FoM.	112
4.30 Comparison of muon yields by its spin pattern: in backgrounds dominant condition (Blue) and in <i>Final candidates</i> condition (Red), respectively.	113
4.31 Results of transverse momentum smearing ($\sigma \Delta p_T$) study by cosmic muons collected in Run 11. Left plot shows result for the negative charged muons and Right plot shows result for the positive charged muons. These plots are quoted from [12].	115
4.32 EUML fit results by hadronic backgrounds PDF composed of hadronic MC samples. The other conditions are same to the Fig. 4.29.	119
4.33 Results of spin pattern shuffling to the <i>Final candidates</i> . Each column shows shuffled $\frac{A_{L,B}}{\Delta A_{L,B}}$ (left), $\frac{A_{L,Y}}{\Delta A_{L,Y}}$ (middle), and $\frac{A_{LL}}{\Delta A_{LL}}$ (right), respectively.	121
4.34 Final beam separated A_L results. The sign of horizontal axis indicates the asymmetry measured in either forward (positive) or backward (negative) with respect to the beam going direction.	123
4.35 Final combined A_L results. The sign of horizontal axis indicates the asymmetry measured in either forward (positive) or backward (negative) with respect to the beam going direction.	124

List of Tables

1.1	Decay modes and Branching ratio of W^+ . [13]	6
2.1	Achieved beam parameters for Run 12 p + p at 510 GeV [14]	12
2.2	Spin patterns in Run 12 p + p at 510 GeV	13
2.3	Summary of detectors related to this analysis. Detectors in this table are lined up by the distance from the collision vertex (Δd). Note that all Δd indicate mean z position of the detector or a station of the detector. The values without brackets indicate common or Muon Arm South while values with brackets indicate Muon Arm North.	22
2.4	Summary of absorbers in forward rapidity. The informations of materials and their thickness are quoted from [7] and The informations of Radiation length (X_0) and Nuclear interaction length (λ_0) are quoted from [15]. The X_0 and λ_n of the steel is calculated by ^{26}Fe only and the SS310 is calculated in the ratio of $^{24}\text{Cr} : ^{26}\text{Fe} : ^{28}\text{Ni} = 0.25 : 0.55 : 0.20$. The values without brackets indicate common or Muon Arm South while values with brackets indicate Muon Arm North.	23
2.5	Summary of FVTX design parameters	25
2.6	Summary of major parameters of Muon Magnets	26
2.7	Segmentation of MuTr. The z distances without brackets indicate common or MuTr South while values with brackets indicate MuTr North.	29
2.8	The ϕ angle offset of <i>stereo</i> cathode planes with respect to their corresponding <i>non-stereo</i> planes.	31
2.9	Design criteria of the PHENIX RPC [16][17]	32
2.10	Table of triggers for Run12 p + p at 510 GeV	38
4.1	Reference conditions for MC production. Quoted from [8]. μ is a parameter for the multiple collision condition.	65
4.2	Table of summary for signal MC and muonic backgrounds MC.	65

4.3	Table of summary for hadron MC	68
4.4	Fraction of events with each multiple collision condition after <i>2nd filtering</i> . The first bin around $W_{ness} \sim 0.01$ is omitted in the fraction calculation.	76
4.5	Summary of <i>Significance</i> test with various conditions. The average values in the last column are calculated by weighting the fraction of each multiple collision condition in Table 4.4, especially with the fraction at $0 \leq W_{ness} \leq 1$	78
4.6	Optimal H_{ness} for several W_{ness} conditions.	82
4.7	Yields of single muon candidates after each filtering condition. Note that the applied $H_{ness_{opt}}$ at 4th filter is the optimal value for $W_{ness} = 0.92$	83
4.8	Simplified list of triggers for Run12 p + p at 510 GeV (Full list in Table 2.10). Triggers tagged as Muon are the triggers for the muon candidates. Especially triggers with abbreviation R12W are main W triggers for the Run12.	85
4.9	Table of 50 trigger combinations. Roman numbers indicate the order of the combination and Italicized numbers indicate the member triggers for corresponding trigger combination. The relationship between the actual member trigger and the italicized number can be seen in Table 4.8. A trigger combination with more than two triggers means all member triggers fired simultaneously for an event. For instance, trigger combination 19 indicates both trigger 18 (R12W1) and trigger 26 (R12W2_S) is fired at the same time.	87
4.10	Overall trigger efficiency at $W_{ness} > 0.92$. Note that MPC sample's statistics is $\sim 50\%$ to ERT after loose cut for independent muon candidates.	91
4.11	Relevant informations of di-muon scaling factors. Note that the trigger efficiencies are obtained in Run 11.	97
4.12	Correlation among di-muon processes in the least-squares fit on the di-muon spectrum.	97
4.13	Integrated probability density of each type of PDF after dw_{23} sidebands removal. The conditions are same to Fig. 4.22 and Fig. 4.23. .	102
4.14	Estimated number of signals and backgrounds. Note that Entries and S/BG are the values after sidebands cut. The other conditions are same to Fig. 4.22 and Fig. 4.23.	102
4.15	Average polarization in Run 12. First type of error indicates standard deviation of the mean and Second type of error indicates propagated average of the Fill by Fill polarization error.	107

4.16 Parameters at <i>Final candidates</i> condition. Systematic uncertainties are not included.	113
4.17 Systematic errors in <i>Final candidates</i> condition induced by $\sigma \Delta p_T^{reco}$	116
4.18 Systematic errors in <i>Final candidates</i> condition induced by muonic backgrounds scaling factors.	117
4.19 Systematic errors in <i>Final candidates</i> condition induced by the method of hadronic backgrounds PDF composition.	118
4.20 Net remaining beam polarization in the A_L estimation.	120
4.21 Summary of studied systematic errors.	122
4.22 Final A_L with systematic uncertainty.	122

Chapter 1

Introduction

1.1 Composition of the thesis

This goal of the analysis in this thesis is a rigorous constraint of sea-quark polarization's contribution to the proton spin $\frac{1}{2}$.

This thesis is composed of four chapters: the first chapter explains motivation and analysis method in the point of view of physics, the second chapter explains the apparatus used for the measurement, the third chapter explains the relevant information of the dataset, and the fourth and final chapter explains technical procedures for the measurement with final results, respectively. Some critical informations related to this analysis are summarized in following list.

- Physics variable: longitudinal single spin asymmetry (A_L)
- Channel: $W^\pm/Z \rightarrow \mu^\pm$
- Collision species and Energy: polarized p + p at $\sqrt{s} = 510$ GeV
- Average beam polarization: $\langle P_B \rangle = 0.536 \pm 0.041$, $\langle P_Y \rangle = 0.574 \pm 0.043$
- Detector acceptance: $1.2 < \eta < 2.2$ (S), $1.2 < \eta < 2.4$ (N) with 2ϕ in azimuth
- $\int L dt = 53.1$ (pb $^{-1}$)
- $16 < \text{reconstructed } \mu p_T < 60$ (GeV/c)

1.2 Physics Motivation

1.2.1 Structure of the Proton

A proton is bound state of three valence quarks. It is one of most basic baryons with neutrons and compose every materials on the universe in the form of nuclei.

In nowdays it is a well known knowledge that a proton is not a simple spin $\frac{1}{2}$ Dirac particle but is a particle with substructure. However the way to probe its substructure is not very different from the first inclusive DIS (deep inelastic scattering) experiment at SLAC (Stanford linear accelerator) in essence: hit the proton by injecting electron beams on it and measuring scattered off electrons. As higher momentum transfer (Q^2) is equivalent to higher probing resolution ($\lambda \sim \frac{1}{\sqrt{Q^2}}$) of the virtual photons (γ^*), if high enough momentum is delivered on proton the scattered electrons will reveal its internal structure. In succession by selecting the detection angle the control of transferred momentum is possible: in other words, the internal structure of the proton for given momentum fraction (the Bjorken x) can be controled, which means the parton distribution function (PDF) of the proton can be measured.

Measuring spin dependent parton distribution requires a little additional setup: since the virtual photons can only couple with quarks of opposite helicity, by controlling the polarization of electron beam and proton target the spin dependent parton distribution, namely polarized PDF can be estimated as well. This type of experiments called as polarized inclusive DIS.

Both inclusive DIS and polarized inclusive DIS measure the scattered off electrons: therefore the measurement cannot distinguish which quark or anti-quark is participated in the interaction. To separate the contribution from quarks or anti-quarks additional detection of final state hadron is required. This type of experiments called as semi-inclusive DIS (SIDIS). As SIDIS requires fragmentation function in hadron's detection, the precision of the measurement is limited by the precision of fragmentation function. This is the main source of uncertainty in current understanding of flavor-separated quarks or anti-quarks spin contribution, which this thesis aims to constrain.

Lastly, the complete map of PDFs and polarized PDFs can be obtained by using fundamental theorems of quantum chromodynamics (QCD) with PDFs obatained so far. This global analysis is the only way to relate measured cross sections to the underlying physics rigorously and the results of this analysis will provide a point to constrain anti-quarks' PDF on the global analysis fit.

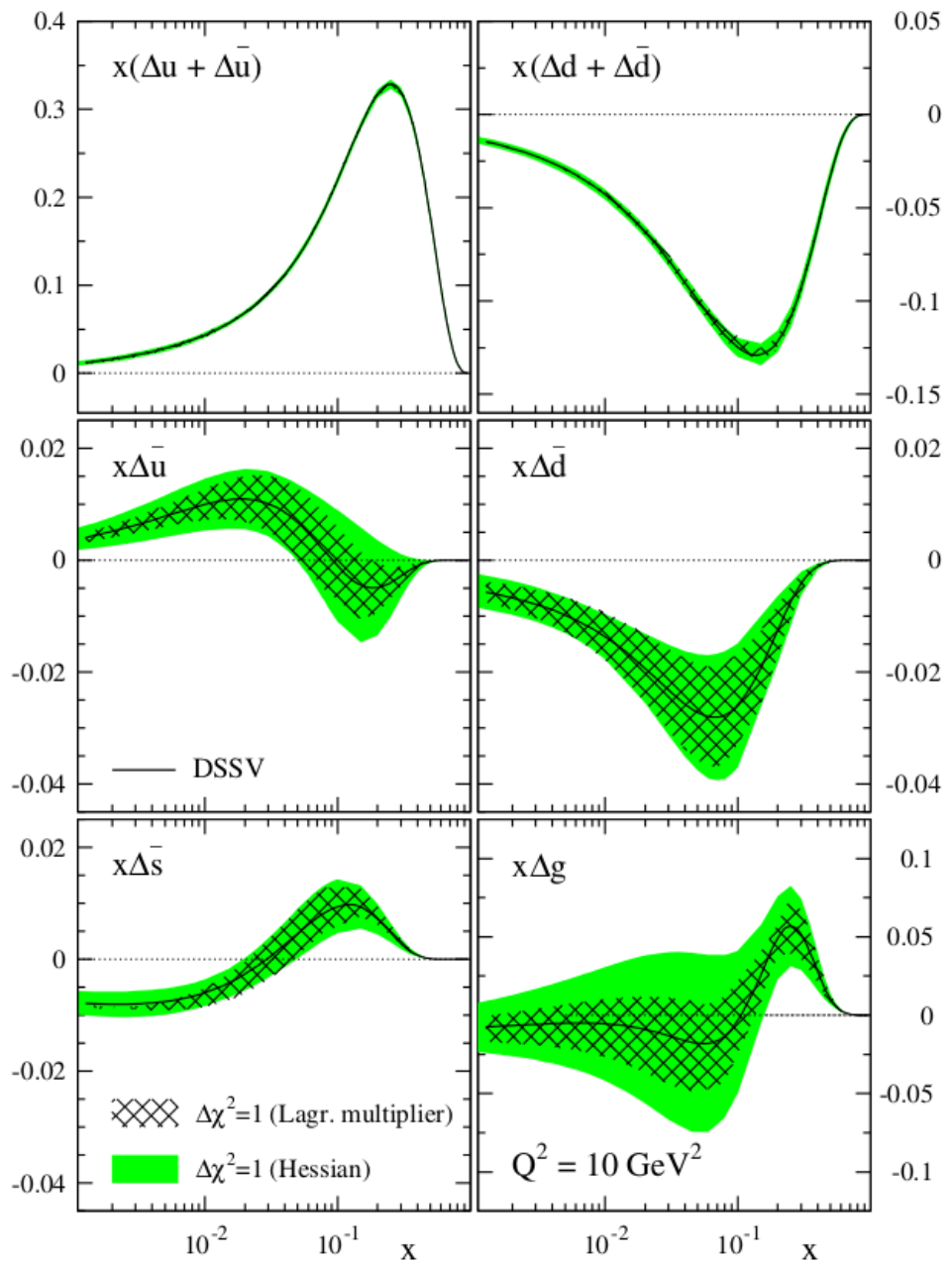


Figure 1.1: Results of global fit by DSSV group. [1]

1.2.2 Probing Sea Quark Polarization in $p + p$ Collisions

As Fig. 1.1 shows the parton distributions of $\Delta\bar{u}$ and $\Delta\bar{d}$ along the x have large uncertainties. Main source of these uncertainties is the anti-quarks' fragmentation functions. Due to the current SIDIS experiments' inseverable dependence on those fragmentation functions, there exist a limit in the precision of the measurement.

The W bosons are composed of a pair of quark and anti-quark. Due to its nature of maximal parity violation only the quarks with negative helicity (left-handed) and anti-quarks with positive helicity (right-handed) can produce a W boson. Therefore by neglecting small contribution from the \bar{s} one can clearly know the helicity and electrical charge of the W 's parent quarks ($u\bar{d}$ for W^+ and $\bar{u}d$ for W^-): in other words, it means a complete flavor separated measurement is possible. In addition some decay modes of the W directly decays into leptons in $\sim 10\%$ branching ratio: by measuring these leptons decayed from W s, a measurement independent of fragmentation function is possible.

This analysis uses $W^\pm \rightarrow \mu^\pm$ detected in forward rapidity which produced in polarized $p + p$ collisions at RHIC. Therefore hadronic production process and leptonic decay of the W are the subjects of interest in this analysis. The observable of the measurement is longitudinal single spin asymmetry (A_L) which reflects the longitudinal spin dependent parton distribution of the proton.

Hadronic production of W bosons The dominant hadronic production subprocess of the W is a pair of quark and anti-quark:

$$q_i\bar{q}_j \rightarrow W$$

where q_i and \bar{q}_j indicate quarks and anti-quarks, respectively. For instance, for the case of W^+ production q_i corresponds to u , c , and t , while \bar{q}_j corresponds to \bar{d} , \bar{s} , and \bar{b} . This hadronic production cross section subprocess can be expressed as follows:

$$\hat{\sigma}(q_i\bar{q}_j \rightarrow W) = 2\pi \left| V_{ij} \right|^2 \frac{G_F}{\sqrt{2}} M_W^2 \delta(\hat{s} - M_W^2) \quad (1.1)$$

where $|V_{ij}|$ is Cabibbo - Kobayashi - Maskawa (CKM) matrix element for q_i and \bar{q}_j , G_F is Fermi coupling constant (1.16637×10^{-5} GeV $^{-2}$), M_W is W mass (80.385 ± 0.015 GeV), and $\hat{s} = (p_1 + p_2)^2$ is square of center of mass energy of the subprocess, respectively. By using the QCD factorization theorem the total cross section of W in $p + p$ collision at leading order (LO) can be written as follows.

$$\sigma(pp \rightarrow W) = \frac{K}{3} \int dx_1 dx_2 \sum_{i,j} q_i(x_1, M_W^2) \bar{q}_j(x_2, M_W^2) \hat{\sigma}(q_i \bar{q}_j \rightarrow W) \quad (1.2)$$

where 3 is degrees of freedom of color, K is a factor includes first order QCD corrections, and $q(x, Q^2)$ is PDF at given x and Q^2 , respectively. As a next step let's consider the *rapidity* of the produced W (y_W) to express it in differential form. Following relation holds for the momentum fraction x and W 's kinetic energy and *rapidity* (y_W).

$$dx_1 dx_2 = \frac{d\hat{s}}{s} dy_W$$

$$y_W = \frac{1}{2} \ln \left(\frac{E_W + p_Z^W}{E_W - p_Z^W} \right) = \frac{1}{2} \ln \left(\frac{x_1}{x_2} \right) \quad (1.3)$$

By using this relation the integral form of cross section in Eq. 1.2 transformed into the differential cross section to the y_W :

$$\frac{d\sigma}{dy_W}(pp \rightarrow W) = K \frac{\sqrt{2}\pi G_F}{3} \sum_{i,j} \left| V_{ij} \right|^2 x_1 x_2 q_i(x_1, M_W^2) \bar{q}_j(x_2, M_W^2) \quad (1.4)$$

For the case of W^+ production, above Eq. 1.4 can be approximated again as follows.

$$\begin{aligned} \frac{d\sigma}{dy_{W^+}}(pp \rightarrow W^+) &\simeq K \frac{\sqrt{2}\pi G_F}{3} x_1 x_2 \left[\cos^2 \theta_c \{u(x_1)\bar{d}(x_2) + \bar{d}(x_1)u(x_2)\} + \sin^2 \theta_c \{u(x_1)\bar{s}(x_2) + \bar{s}(x_1)u(x_2)\} \right] \quad (1.5) \\ &\sim K \frac{\sqrt{2}\pi G_F}{3} x_1 x_2 \cos^2 \theta_c \{u(x_1)\bar{d}(x_2) + \bar{d}(x_1)u(x_2)\} \end{aligned}$$

where θ_c is Cabibbo angle. The second approximation of Eq. 1.5 is based on strong suppression by θ_c . One can obtain W^- similarly by taking Hermitian conjugate of Eq. 1.5.

Leptonic decay of W bosons Table 1.1 shows several decay modes of W^+ with its branching ratio. Note that W^- modes are each mode's charge conjugates. The W bosons are usually probed by using leptonic decay mode as they provides cleaner channel: though the hadronic decay mode is most abundant, due to the existence of huge QCD backgrounds (ex. jets) it is more difficult to probe. Fig. 1.2 shows production and leptonic decay of W^\pm .

W^+ decay modes	Branching Ratio
$e^+ \nu$	$(10.75 \pm 0.13) \%$
$\mu^+ \nu$	$(10.57 \pm 0.15) \%$
$\tau^+ \nu$	$(11.25 \pm 0.20) \%$
hadrons	$(67.60 \pm 0.27) \%$

Table 1.1: Decay modes and Branching ratio of W^+ . [13]

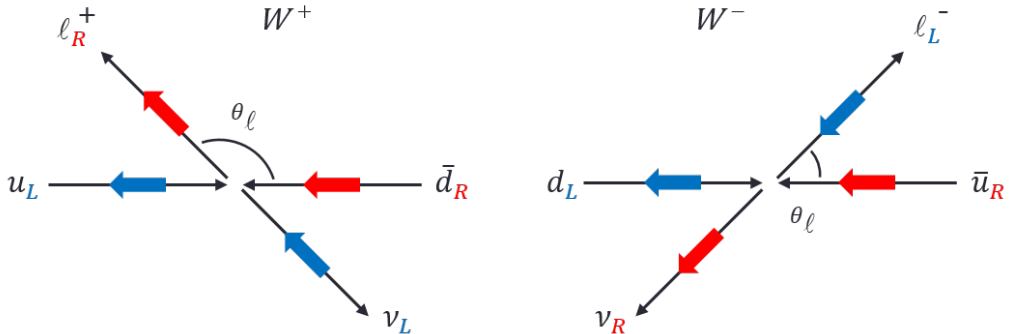


Figure 1.2: Production and decay of W^+ (left) and W^- (right) with its helicity

Only the quark with positive helicity (right-handed) and anti-quark with negative helicity (left-handed) can produce a W boson: considering this maximal parity violating nature, a couple of conclusions can be extracted regarding leptons' emission direction. For the W production $p + p$ collision, most of the quarks involved in the interaction should be the valence quarks while most of the anti-quarks should be the sea quarks. One can expect the quarks will carry significantly larger momentum fraction (x) compared to the sea quarks: thus the W bosons' longitudinal momentum direction will be same to the quarks' direction. As a result, rapidity of the W^+ ($u\bar{d}$) tend to be aligned with u-quark direction and rapidity of the W^- ($\bar{u}d$) tend to be

aligned with d-quark direction. Therefore the l^+ from the W^+ tend to be produced in opposite direction to the W^+ momentum (backward) while the l^- from the W^- tend to be produced in same direction to the W^- momentum (forward).

Related to the angle of leptonic decay following proportional relation holds: note that the factor $(1 \pm \cos \theta_l)^2$ is the direct results of parity violation.

$$\begin{aligned} \frac{d\sigma}{dcos\theta} (u\bar{d} \rightarrow W^+ \rightarrow l^+ \nu_l) &\propto (1 - \cos \theta_l)^2 \\ \frac{d\sigma}{dcos\theta} (\bar{u}d \rightarrow W^- \rightarrow l^- \nu_l) &\propto (1 + \cos \theta_l)^2 \end{aligned} \quad (1.6)$$

Then the differential cross section for the given y_W and the given lepton scattering angle θ_l can be expressed as:

$$\begin{aligned} \left(\frac{d^2\sigma}{dy_W dcos\theta_l} \right)_{W^+} &\sim u(x_1)\bar{d}(x_2)(1 - \cos \theta_l)^2 + \bar{d}(x_1)u(x_2)(1 + \cos \theta_l)^2 \\ \left(\frac{d^2\sigma}{dy_W dcos\theta_l} \right)_{W^-} &\sim \bar{u}(x_1)d(x_2)(1 - \cos \theta_l)^2 + d(x_1)\bar{u}(x_2)(1 + \cos \theta_l)^2 \end{aligned} \quad (1.7)$$

Also the x_1 and x_2 can be expressed in y_W as follows.

$$x_1 = \frac{M_W}{\sqrt{s}} e^{y_W}, \quad x_2 = \frac{M_W}{\sqrt{s}} e^{-y_W} \quad (1.8)$$

Longitudinal single spin asymmetry (A_L) The A_L is the observable of the $W^\pm \rightarrow l^\pm$ in longitudinally polarized p + p collisions. It reflects spin dependent longitudinal parton distribution of the proton. Under the assumption of the protons of the beam is polarized in 100 % efficiency (completely aligned to the direction of beam polarization) the definition of A_L can be written as follows.

$$A_L = \frac{\sigma_+ - \sigma_-}{\sigma_+ + \sigma_-} \quad (1.9)$$

where σ indicates the longitudinal cross section and each subscript sign indicates the helicity direction. + sign indicates its helicity direction is positive (right-handed) and vice versa. This A_L is being measured by collecting leptons decayed from W bosons. Following Fig. 1.3 and Fig. 1.4 shows all possibilities producing W^+ .

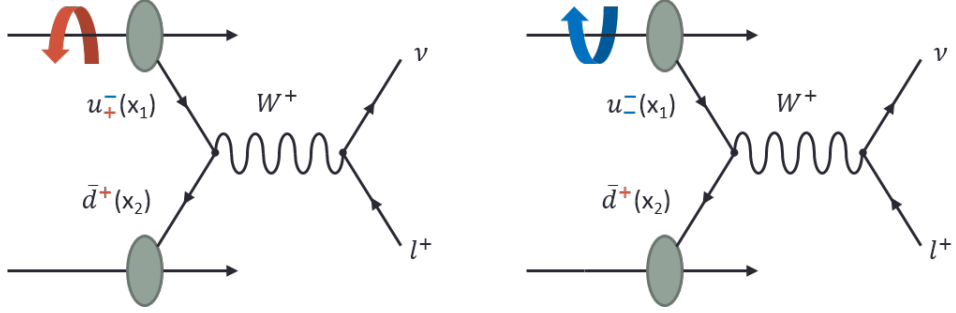


Figure 1.3: W^+ production in polarized $p + p$. In this case u is being probed. The colored superscript sign of u and \bar{d} indicates corresponding quark or anti-quark's helicity while The colored subscript sign of u indicates helicity of the beam.

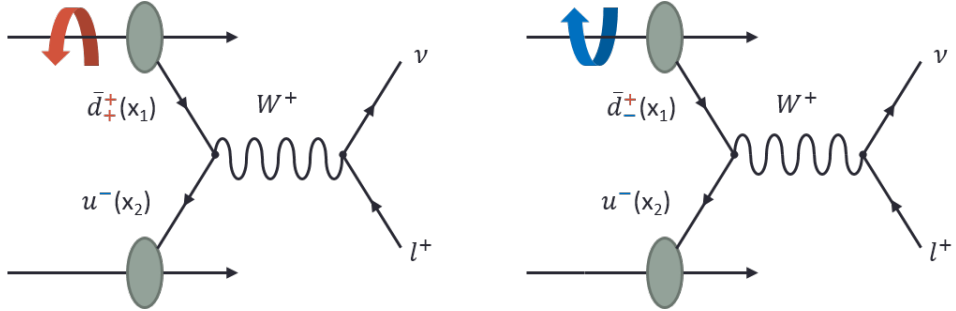


Figure 1.4: W^+ production in polarized $p + p$, In this case \bar{d} is being probed. Same notation to the Fig. 1.3 holds for the colored superscripts and subscripts.

The A_L^{W+} measured in the case of Fig. 1.3 and Fig. 1.4 are as follows:

$$A_L^{W+} = \frac{u_-(x_1)\bar{d}^+(x_2) - u_+(x_1)\bar{d}^+(x_2)}{u_-(x_1)\bar{d}^+(x_2) + u_+(x_1)\bar{d}^+(x_2)} \quad (1.10)$$

$$A_L^{W+} = \frac{\bar{d}_-(x_1)u^+(x_2) - \bar{d}_+(x_1)u^-(x_2)}{\bar{d}_-(x_1)u^+(x_2) + \bar{d}_+(x_1)u^-(x_2)} \quad (1.11)$$

However, in reality one cannot know which type of interaction produced the W^+ in $p + p$ collisions. Therefore what actually measured is the statistical ensemble of above two cases:

$$A_L^{W+} = -\frac{\Delta u(x_1)\bar{d}(x_2) - \Delta\bar{d}(x_1)u(x_2)}{u(x_1)\bar{d}(x_2) + \bar{d}(x_1)u(x_2)} \quad (1.12)$$

Similary, for the case of W^- measurement:

$$A_L^{W-} = \frac{\Delta\bar{u}(x_1)d(x_2) - \Delta d(x_1)\bar{u}(x_2)}{\bar{u}(x_1)d(x_2) + d(x_1)\bar{u}(x_2)} \quad (1.13)$$

As actual measurement is performed by collecting leptons decayed from Ws , considering the lepton scattering angle (θ_l) in Eq. 1.7 the above equations modified as follows.

$$\begin{aligned} A_L^{W+} &= -\frac{\Delta u(x_1)\bar{d}(x_2)(1 - \cos\theta_l)^2 - \Delta\bar{d}(x_1)u(x_2)(1 + \cos\theta_l)^2}{u(x_1)\bar{d}(x_2)(1 - \cos\theta_l)^2 + \bar{d}(x_1)u(x_2)(1 + \cos\theta_l)^2} \\ A_L^{W-} &= \frac{\Delta\bar{u}(x_1)d(x_2)(1 - \cos\theta_l)^2 - \Delta d(x_1)\bar{u}(x_2)(1 + \cos\theta_l)^2}{\bar{u}(x_1)d(x_2)(1 - \cos\theta_l)^2 + d(x_1)\bar{u}(x_2)(1 + \cos\theta_l)^2} \end{aligned} \quad (1.14)$$

Note that both A_L^{W+} and A_L^{W-} in Eq. 1.14 are convoluted sum of quarks and anti-quarks. Therefore perfectly pure anti-quark PDF cannot be extracted unlike the first argument. However under the following conditions anti-quark PDFs can be extracted with very high purity. For the case of $W^- \rightarrow l^-$, let's consider the condition $x_1 \ll x_2$. It is correponds to the condition of large negative y_W and $\theta_l \sim \pi$. Under this circumstance the convolution over x_1 and x_2 is almost separated then second term in Eq. 1.14 will be strongly suppressed. Then, as a result,

$$A_L^{W-}(x_1 \ll x_2) \approx \frac{\Delta\bar{u}(x_1)}{\bar{u}(x_1)} \quad (1.15)$$

almost pure $\Delta\bar{u}$ can be estimated in small x (~ 0.05). On the other hand, let's consider the reverse condition of $x_1 \gg x_2$: this condition corresponds to large positive y_W and $\theta_l \sim 0$.

$$A_L^{W-}(x_1 \gg x_2) \approx \frac{\Delta d(x_1)}{d(x_1)} \quad (1.16)$$

In this condition almost pure Δd can be estimated in large x (~ 0.4). Unlike the $W^- \rightarrow l^-$ case, for the case of $W^+ \rightarrow l^+$ the convolution over each x_1 and x_2 does not separate clearly no matter how the rapidity condition is. Thus clear measurement of anti-quark PDF cannot be expected. This entangled convolution mainly comes from the preference of the decay direction of l^+ from W^+ .

Physics impact Following Fig. 1.5 shows the expected impact on DSSV global analysis by $W^\pm \rightarrow l^\pm$ at RHIC. Top two plots are current DSSV global fit results and Bottom two plots are expected global fit after using the replica of $200 \text{ pb}^{-1} W$ data at RHIC. As it shows, clear improvements in uncertainty can be found in the range of $x < 10^{-1}$.

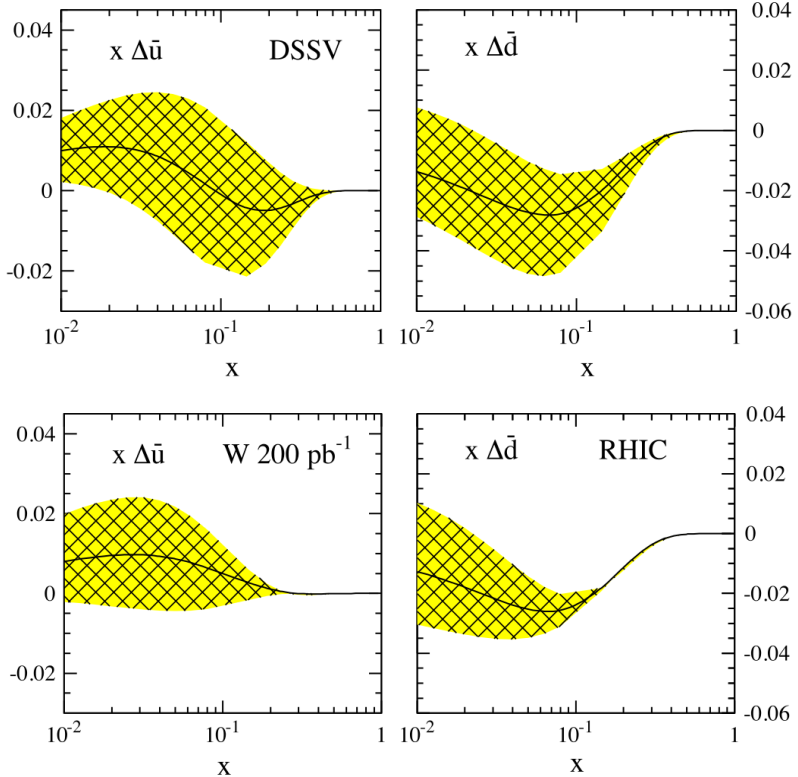


Figure 1.5: Results of DSSV global fit for $\Delta \bar{u}$ (x, Q^2) and $\Delta \bar{d}$ (x, Q^2) at $Q^2 = 10 \text{ GeV}^2$ before (top) and after (bottom) adding the replica of the RHIC W results. The total integrated luminosity of the replica is 200 pb^{-1} [2].

Chapter 2

Apparatus

This analysis utilizes RHIC accelerator facility and PHENIX detector system as the apparatus of the measurement. This chapter composed of 3 main sections: first section explains operation of polarized proton source and its polarization control at RHIC, second section explains composition of PHENIX detector system, and third and last section explains process of online data acquisition at PHENIX, respectively.

2.1 RHIC

For the polarized proton operations, RHIC (Relativistic Heavy Ion Collider) accelerator complex is capable of boosting injected proton bunch's energy up to 510 GeV in the center of mass as well as maximum 65 % of its polarization is conserved.

2.1.1 Beam Acceleration

Polarized proton source The polarized proton source in RHIC is Optically-Pumped Polarized H⁻ Ion Source (OPPIS), which provides 1.5×10^{12} H⁻ ions with ~ 80 % polarization at a repetition rate of 7.5 Hz [18][5].

LINAC, Booster Synchrotron, and AGS The produced H⁻ ions injected into RFQ (Radio-Frequency Quadrupole) followed by 200 MHz LINAC. At this stage the ions accelerated up to 200 MeV and strips electrons away by pass through stripping foil. As a next step, the Booster Synchrotron accepts transferred ions and shapes them into a single proton bunch as well as accelerate it up to 1.5 GeV. Then the proton bunch fed into AGS (Alternating Gradient Synchrotron) and accelerated again up to 24.3 GeV, and finally injected to the RHIC.

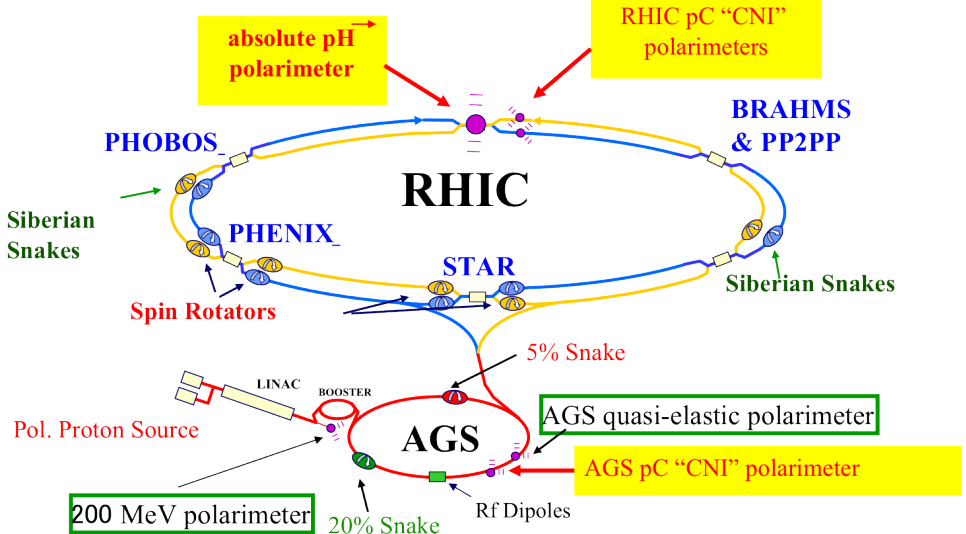


Figure 2.1: RHIC accelerator complex [3]

RHIC In the RHIC rings, the proton bunch transferred from AGS accelerated to the target collision energy, then collide to each other in each intersection point. In actual $p + p$ operations each of the rings denoted as *Blue* (circulate clockwise) and *Yellow* (circulate counter-clockwise) (Fig. 2.1) and is capable of run maximum 120 bunches for a fill, which corresponds to 106.572 ns of bunch crossing time. Table 2.1 shows some beam condition parameters for the Run 12 $p + p$ (proton - proton data taking period in 2012).

Parameter	Value
Beam energy [GeV]	254.9
β^* [m]	0.65
Int. L (total delivered) [pb^{-1}]	133
L_{average} [$\text{cm}^{-2}\text{s}^{-1}$]	1.05×10^{32}
L_{peak} [$\text{cm}^{-2}\text{s}^{-1}$]	1.65×10^{32}
No. of bunches	109
No. of ions/bunch	1.70×10^{11}
RMS emittance [μm]	3.5 → 4.2

Table 2.1: Achieved beam parameters for Run 12 $p + p$ at 510 GeV [14]

2.1.2 Beam Polarization

Spin direction and Spin pattern The direction of each proton bunch's polarization, or spin direction is set during the production at the source. Its nominal direction is either vertical-up (+) or vertical-down (-). Once the beam is injected into the RHIC rings spin direction can be adjusted again by using Spin Rotators at the front and the rear of each interaction (collision) points (Fig. 2.1). At this point the direction can be either longitudinal (spin aligned along the beam direction) or transverse (spin aligned perpendicular to the beam direction).

The term Spin pattern indicates series of pre-determined combination of spin direction for proton bunches in each ring. In principle any kind of combination is available, however, all possible four combinations (++, +-, -, --) in equal ratio is typically used to minimize systematic uncertainties originated from beam conditions. Table 2.2 shows summary of Spin patterns used in Run 12.

Spin pattern	Blue (cw)	Yellow (ccw)
p1	+- + - - + +	++ - - + + - -
p2	- + - + + - +	++ - - + + - -
p3	+- + - - + - +	- - + + - - + +
p4	- + - + + - +	- - + + - - + +

Table 2.2: Spin patterns in Run 12 p + p at 510 GeV

Although a ring can operate maximum 120 bunches for a fill, not all of bunches filled in typical operation. First, last 9 bunches out of 120 (111 - 119) is reserved for abort operation time for the case of beam dump (abort gap). Second, a couple of bunches in a ring (38 and 39 for the Blue, 78 and 79 for the Yellow) is reserved to be empty to crosscheck the patterns.

Polarization control and Siberian snakes [5][19] To achieve polarized deep inelastic scattering (pDIS) events the polarization of a proton bunch must be conserved until it reaches interaction point. Following paragraphs explain major source of degradation in overall polarization and its countermeasure.

The evolution of the spin direction of polarized protons in external magnetic field can be described by the Thomas-BMT equation [20],

$$\frac{d\vec{P}}{dt} = -\left(\frac{e}{\gamma m}\right) [G\gamma\vec{B}_\perp + (1+G)\vec{B}_\parallel] \times \vec{P} \quad (2.1)$$

where \vec{P} is polarization vector, γ is E/m , G_γ is number of spin precession per revolution (also called as spin tune, ν_{sp}), \vec{B} is external magnetic field, and $G = 1.7928$ is anomalous magnetic moment of the proton, respectively. Since nominal direction of holding magnetic field in RHIC is vertical, the equation can be simplified as follows under the assumption of holding field is purely vertical.

$$\frac{d\vec{P}}{dt} = -\left(\frac{e}{\gamma m}\right)[G_\gamma \vec{B}_\perp] \times \vec{P} \quad (2.2)$$

This simplified Thomas-BMT equation can be interpreted as the Lorentz equation for orbital motion of a charged particle in external magnetic field \vec{B}_\perp with factor G_γ . It means the spin rotates G_γ times faster than the orbital motion (a revolution with respect to the ring). At maximum RHIC energies the G_γ reaches about 400.

The depolarization happens when the spin precession frequency G_γ of the beam equals to the frequency of the spin-perturbing magnetic field and resonance occur. If $G_\gamma = n$ ($n = 1, 2, 3, \dots$) under the existence of spin-perturbing magnetic field, the protons will periodically encounter perturbation in their precession which constructively build up over multiple revolution. As a result, this accumulated perturbation lead to degradation in overall beam polarization. There are mainly two types of depolarization resonances: *imperfection resonances* driven by magnet errors or misalignment, and *intrinsic resonances* driven by the focusing field.

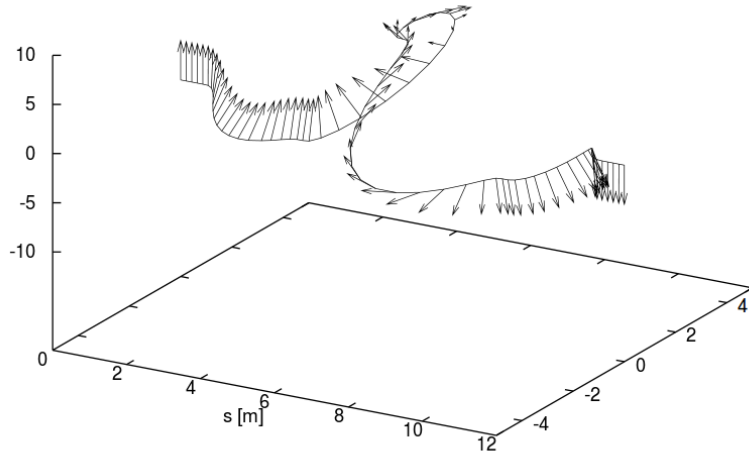


Figure 2.2: 180° flip in polarization direction by a full Siberian Snake [4].

The Siberian Snakes are a countermeasure of this depolarization phenomena. A Snake is a series of helical dipoles which creates a magnetic field perpendicular to the polarization vector, causing it to rotate with respect to the horizontal axis. A full Snake is capable of flipping polarization vector by 180° and enables spin direction remains unperturbed. In a G_γ point of view, the G_γ with the Siberian Snakes is a half integer and energy independent thus occurrence of depolarizing resonance itself is prevented. There are two types of Siberian Snakes in RHIC accelerator complex: a 5 % partial Snake in AGS (rotate 9°) and a couple of full Snakes in each RHIC ring. Fig. 2.3 shows positions of Siberian Snakes in RHIC rings.

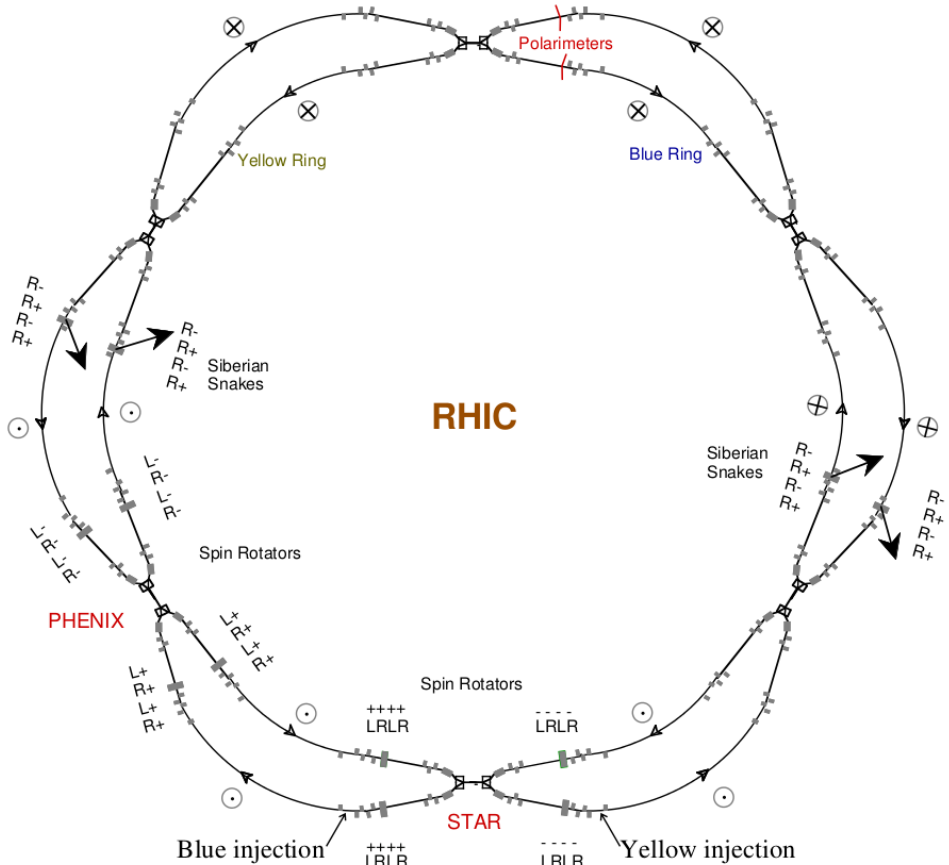


Figure 2.3: Positions of Siberian Snakes and Spin Rotators in RHIC [5]

CNI Polarimetry The preserved polarization at RHIC can be measured via 2 global polarimeters and 1 local polarimeter. The first two, p-C (proton-carbon) and H-jet (hydrogen jet) is located in 12 o' clock position at RHIC rings and measures global beam polarization, while the last local polarimeter is located at 8 o' clock position (PHENIX) and measures delivered polarization at PHENIX.

All 3 polarimeters are based on same principle of elastic scattering in the Coulomb-Nuclear Interference (CNI) region. The observable is single transverse spin asymmetry (A_N) from the scattering of polarized proton and unpolarized target. The relation between the beam polarization and the A_N can be expressed as follows:

$$\epsilon_N = \frac{N_L - N_R}{N_L + N_R} = P_b A_N \quad (2.3)$$

Where ϵ_N denotes measured raw asymmetry, N_L (N_R) denotes number of hadrons scattered to the left (right) with respect to the beam axis, and P_b denotes beam polarization. Note that the A_N is also called as ‘analyzing power’ and can be obtained by either experiment or theory.

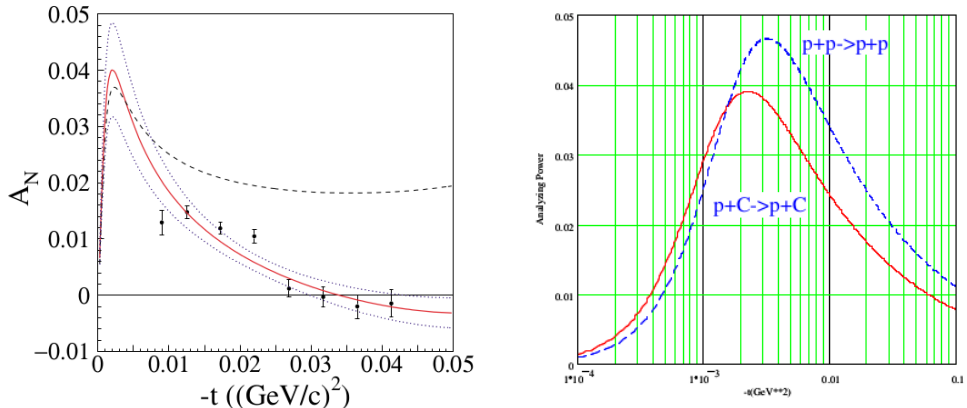


Figure 2.4: A_N for pC (left) and pC/pp (right) elastic scattering in the CNI region. Left figure shows actual measurement result with 21.7 GeV proton beam at AGS (left) [6] while Right figure shows calculated distributions for a carbon ($Z = 6$, $\sigma_{tot} = 330$ mb) and proton ($Z = 1$, $\sigma_{tot} = 35$ mb) target with 250 GeV proton beam [5].

p-C polarimeter uses ultrathin microribbon carbon as a target and measures ϵ_N via 0.1 - 1 MeV recoil carbons from $p^\uparrow + C \rightarrow p + C$. Actual measurement is performed by inserting ribbon target into the beam, and then recoil carbons are detected by 6 silicon strip detectors installed in 90° positions with respect to the beam axis. The large cross section of the pC elastic scattering enables statistically rich measurement, thus high precision can be achieved in limited data acquisition time (~ 1 minute for a scanning). However, as Figure 2.4 suggests there exist clear discrepancy between the A_N^{pp} and the A_N^{pC} . Therefore the beam polarization measured by p-C polarimeter is only valid in the manner of relative polarization and must be calibrated by using A_N^{pp} in following paragraphs.

$$P_b = \epsilon_N / A_N^{pC} \quad (2.4)$$

H-jet polarimeter uses dilute gas jet of vertically polarized hydrogen as a target. The actual measurement is performed by silicon detectors similar to p-C polarimeter, however, H-jet measures scattered protons from both beam and target unlike previous case. The major advantage of H-jet polarimeter comes from particle identity between the beam and the target. By this identity A_N of both beam and target are same, therefore the polarization of the beam can be expressed as follows.

$$\begin{aligned} A_N^{pp} &= \epsilon_N^b / P_b \\ &= \epsilon_N^t / P_t \quad \implies \quad P_b = P_t \frac{\epsilon_N^b}{\epsilon_N^t} \end{aligned} \quad (2.5)$$

Here P_t indicates the polarization of the target and is given by independent Breit-Rabi polarimeter. As a result the absolute beam polarization can be measured explicitly. This measurement does not affect RHIC beams due to its small target thickness ($\sim 10^{12}$ atoms/cm²)[21] thus can be performed continuously, however, its statistics is limited by the same reason. In conclusion, the H-jet polarimeter is appropriate for the determination of absolute beam polarization, however, is not appropriate for the purpose of beam monitoring. Therefore RHIC utilizes both p-C and H-jet polarimeter to make up each other's weakness.

Unlike previous global polarimeters Local polarimeter is only related to the regional beam polarization at PHENIX, especially for the longitudinally polarized spin runs. As mentioned above the nominal spin direction in the RHIC rings is vertical. However, for the case of longitudinal spin runs the spin direction is adjusted to parallel (antiparallel) to beam axis by Spin Rotators. In this case the Local polarimeter provides quality information of the longitudinal polarization of the beam by measuring residual transverse spin asymmetry (A_N) from direct neutrons. Local polarimeter is composed of SMD (Shower Maximum Detector) and ZDC (Zero Degree Calorimeter).

SMD is an array of scintillators located in front of ZDC and used for the position reconstruction of the neutrons, while ZDC is a calorimeter of 6 nuclear interaction length (λ_n). It is positioned behind DX dipole magnet at 18 m distance from the collision point and covers ± 2.8 mrad solid angle around zero scattering angle (Figure 2.5). Considering the effect of the DX magnet (prevent charged particle contamination) and the nature of longitudinal spin asymmetry (parity-violating), the measured A_N can be regarded as it solely originated from the collisions.

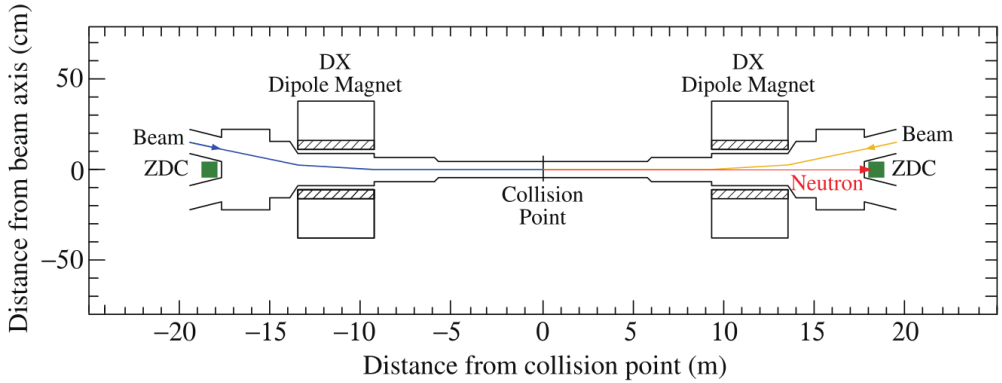


Figure 2.5: Geometrical layout of Local polarimeter (ZDC, SMD) at PHENIX [7]

2.2 PHENIX

The PHENIX detector is located in the 8 o'clock interaction point at RHIC.

2.2.1 Overview

The Cartesian coordinates at PHENIX is determined by its collision point and clockwise running beam's (*Blue*) outgoing direction. The collision point (primary vertex) is the zero point of entire coordinate system. From the point of view of collision point, the *Blue* beam incident from south and then escape to north. The coordinates at PHENIX set the *Blue* beam's outgoing as $+z$ direction. Thus $+z$ in PHENIX corresponds to north and $+x$ corresponds to west.

The entire PHENIX detector system can be decomposed into two main parts: a pair of spectrometers installed along z axis (beam direction) called as Muon Arms and a pair of spectrometers installed perpendicular to z axis called as Central Arms, respectively.

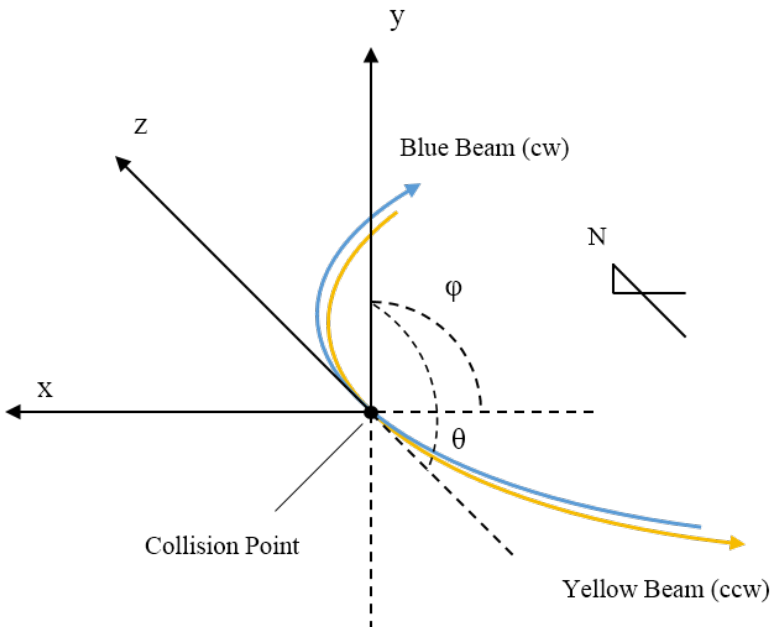


Figure 2.6: Cartesian coordinates at PHENIX

As its name suggests Muon Arms are specialized in the measurement of muons. Each Muon Arm is denoted as Muon Arm South (-z) or Muon Arm North (+z) by its geometrical position with respect to the PHENIX coordinate system. The Muon Arms cover acceptance of $1.2 < |\eta| < 2.2$ (S)/ 2.4 (N) in pseudorapidity with 2π in azimuth. Note that the size of each Muon Arm is not same: Muon Arm South is smaller than the North due to service purpose. Also note that each Muon Arm's η is distinguished by sign: typically Muon Arm South is denoted by negative η (ex. $-2.2 < \eta < -1.2$) while Muon Arm North is denoted by positive η . A Muon Arm includes following detectors: FVTX (Forward Silicon Vertex Trackers), MuTr (Muon Trackers), MuID (Muon Identifiers), and RPC (Resistive Plate Counters).

On the other hand, Central Arms are designed for the measurement of photons, electrons, neutral pions and charged hadrons. Similar to the Muon Arms each Central Arm denoted as West Carriage (+x) or East Carriage (-x) and covers acceptance of $|\eta| < 0.35$ in pseudorapidity with $\pi/2$ in azimuth. A Central Arm includes following detectors: VTX (Silicon Vertex Trackers), DC (Drift Chambers), PC (Pad Chambers), RICH (Ring Imaging Cherenkov detector), Aerogel, ToF (Time of Flight), and EMCal (Electromagnetic calorimeters: PbSc and PbGl).

Aside from above two main parts, there exist a couple of global detectors (BBC (Beam Beam Counters) and ZDC (Zero Degree Calorimeters)) in addition to a calorimeter in very forward pseudorapidity ($3.1 < |\eta| < 3.7$) named MPC (Muon Piston Calorimeter). Note that the details of Central Arms and MPC will be skipped or least mentioned as this analysis utilizes single muons measured in the Muon Arms.

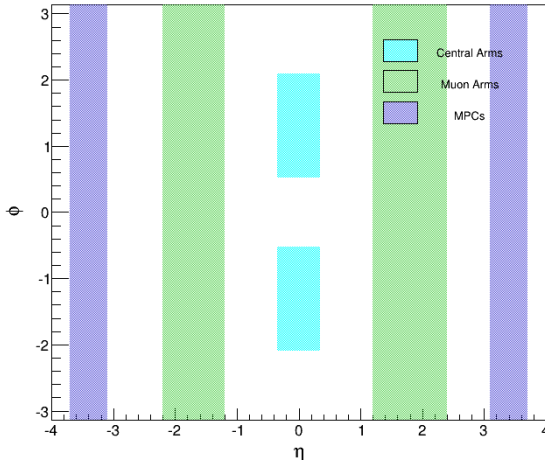


Figure 2.7: Geometrical acceptance of PHENIX detector system

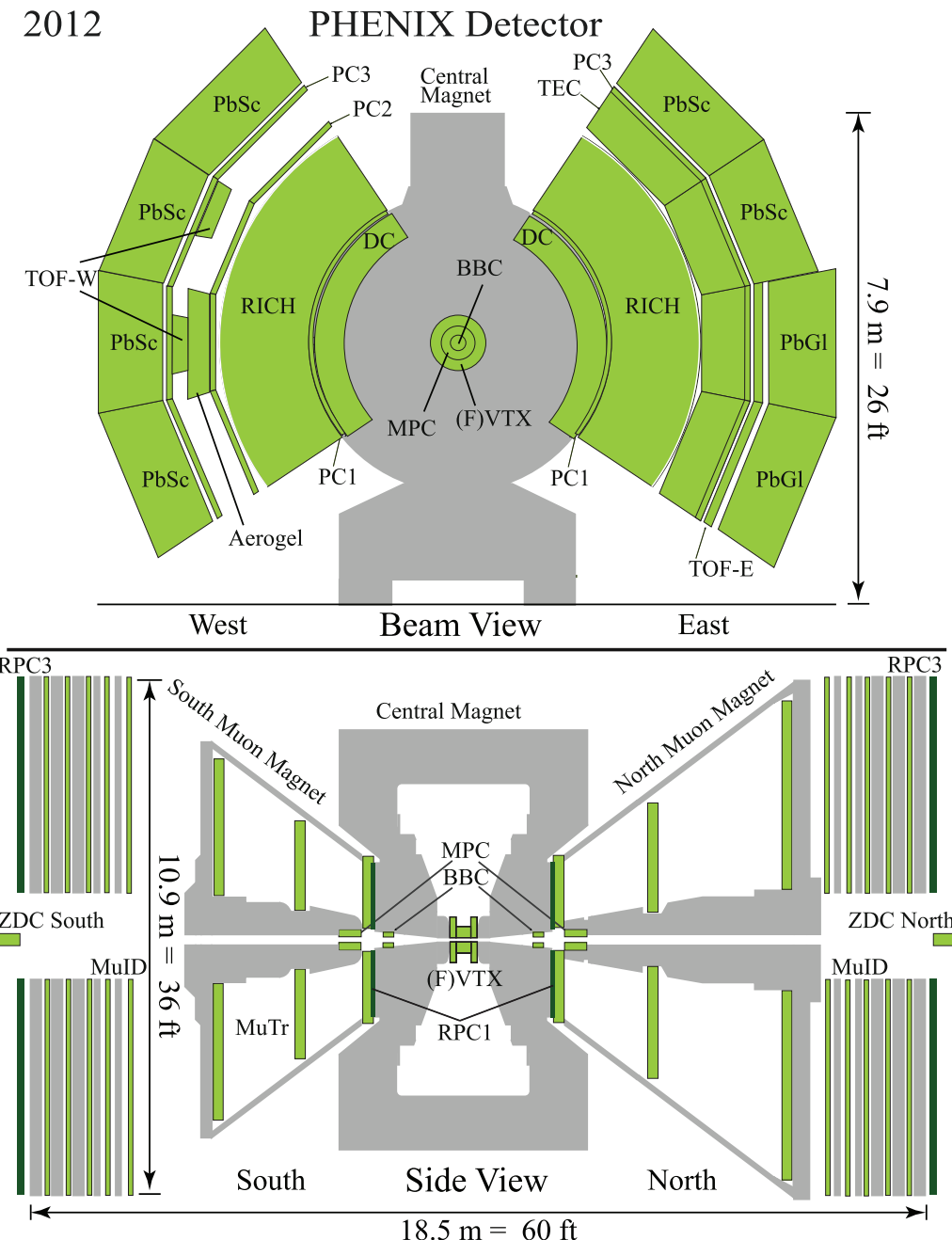


Figure 2.8: Layout of PHENIX detectors in 2012. Central Arms in the beam view (top) and Muon Arms in the sideview (bottom)

2.2.2 Subsystems

Several subsystems' detailed informations will be presented in this section. Note that the term subsystem in this thesis indicates all related experimental apparatus including absorbers and magnets, while the term detector indicates only a device for detection (count/trigger), tracking, and identification of high-energy particles.

Note that not all of subsystems in PHENIX are included in this section: only the subsystems related to this analysis will be presented in alphabetical order.

	Type	Δd (cm)	$ \eta $	$\Delta\phi$	Purpose
FVTX ¹	Muon	20.11	1.2 - 2.2	2π	Tracking Vertex
		26.14			
		32.17			
		38.20			
BBC	Global	144.35 ²	3.1 - 3.9	2π	Fast/Rough vertex Luminosity monitor Minimum bias trigger Start timing
RPC1 ¹	Muon	155.75	1.18 - 2.06	2π	Triggering
Upstream absorber ³					
MuTr	Muon	189.0	1.15 - 2.25	2π	Tracking Triggering
		313.5 (363.5)	(1.15 - 2.44)		
		448.5 (595.4)			
MuID	Muon	701.1	1.15 - 2.25	2π	Particle ID Triggering
		740.9	(1.15 - 2.44)		
		779.0			
		824.5			
		870.0			
Downstream absorber ³					
RPC3	Muon	908.05	1.39 - 2.56	2π	Triggering
ZDC	Global	1800	± 2 mrad	2π	Minimum bias trigger Local polarimetry

¹ Commissioned during Run 12

² Inner edge of the BBC (not a mean z position)

³ Unofficial convention (only used in this thesis)

Table 2.3: Summary of detectors related to this analysis. Detectors in this table are lined up by the distance from the collision vertex (Δd). Note that all Δd indicate mean z position of the detector or a station of the detector. The values without brackets indicate common or Muon Arm South while values with brackets indicate Muon Arm North.

Absorbers For the efficient muon measurements other types of charged particles should be suppressed as strongly as possible. There are mainly two sets of absorber materials in PHENIX Muon Arms: a set of materials after the collision vertex and before the MuTr station 1 and another set of materials after the MuTr station 3 and before the RPC3, respectively. Hereafter the former will be denoted as the Upstream absorber and the latter will be denoted as the Downstream absorber. Each absorber's components and absorption effectiveness can be found in following Table 2.4.

Type	Item	Material	THK (cm)	$X_0/\cos\theta$	$\lambda_n/\cos\theta$
Upstream	Nose cone	Copper	20	13.93	1.31
	Central Magnet	Steel	60	34.15	3.58
	SS310 absorber	Steel *	35	20.08	2.10
Sum before MuTr			115	68.15	6.98
Downstream	Muon Magnet yoke	Steel	20 (30)	11.38 (17.07)	1.19 (1.79)
	MuID wall 1st	Steel	10	5.69	0.60
	MuID wall 2nd	Steel	10	5.69	0.60
	MuID wall 3rd	Steel	20	11.38	1.19
	MuID wall 4th	Steel	20	11.38	1.19
	MuID wall 5th	Steel	20	11.38	1.19
	Sum before RPC3		215 (225)	125.07 (130.76)	12.94 (13.54)

* $^{24}\text{Cr} - {}^{28}\text{Ni}$ enriched stainless steel

Table 2.4: Summary of absorbers in forward rapidity. The informations of materials and their thickness are quoted from [7] and The informations of Radiation length (X_0) and Nuclear interaction length (λ_0) are quoted from [15]. The X_0 and λ_n of the steel is calculated by ^{26}Fe only and the SS310 is calculated in the ratio of $^{24}\text{Cr} : {}^{26}\text{Fe} : {}^{28}\text{Ni} = 0.25:0.55:0.20$. The values without brackets indicate common or Muon Arm South while values with brackets indicate Muon Arm North.

The accumulated nuclear interaction length of the Upstream absorber is $\sim 7.0/\cos\theta$, therefore the hadrons produced before the Upstream absorber will be suppressed in the scale of $\sim 10^{-3}$ before they reach MuTr.

On the other hand, in order to penetrate through the Upstream absorber, a muon must have at least $1.9 \text{ GeV}/\cos\theta$ of energy at the vertex. Similarly, in order to penetrate through all absorbers in forward rapidity, a muon must have at least $2.7 \text{ GeV}/\cos\theta$ of energy at the vertex [22]. Note that newly installed SS310 absorber didn't considered for these values thus the actual required energy for the penetration will be higher.

BBC (Beam Beam Counters) [23] The BBC is one of two global detectors with ZDC. The BBC performs following roles in online data taking: minimum bias trigger with ZDC, fast but rough z-vertex determination, start timing (t_0) for the time-of-flight measurement, and luminosity monitoring, respectively. Also in offline data analysis BBC provides innermost information for the Muon Arm track reconstruction. A complete BBC (South or North) covers $3.1 < |\eta| < 3.9$ in pseudorapidity with full azimuth and positioned in 144.35 cm distance from the collision vertex.

The equations for the z-vertex (Vtx_z) determination and the start timing (t_0) are as follows:

$$\begin{aligned} Vtx_z &= \frac{t_S - t_N}{2} \times c \\ t_0 &= \frac{t_S + t_N}{2} - \frac{L}{c} \end{aligned} \quad (2.6)$$

where t_S (t_N) indicates average hit time in BBC South (North), c indicates speed of the light, and L indicates BBC's distance from the collision vertex, respectively.

The basic unit of the BBC is a quartz-Cherenkov radiator with a meshed-dynode photomultiplier tube (PMT). On the other hand, a complete BBC is composed of 64 basic units in the structure of 3 rings which surround the beam pipe (Fig. 2.9). The maximum achievable time resolution of the start timing (t_0) by the BBC is ~ 20 ps.

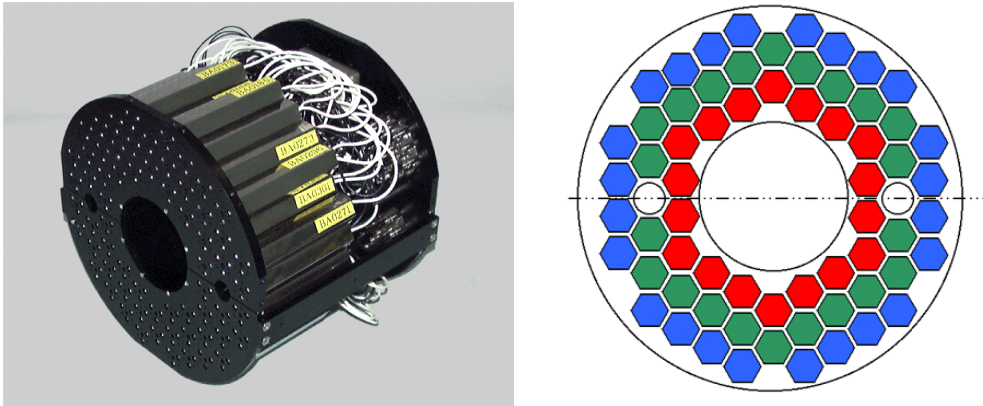


Figure 2.9: A BBC supermodule's picture (left) and its layout in beam view (right). A couple of blank circles in layout's middle layer indicate the positions of laser sources for calibration.

FVTX (Forward Vertex Silicon Trackers) [24] The FVTX is one of two trackers in forward rapidity and provides tracking informations close to the collision vertex. The FVTX covers $1.2 < |\eta| < 2.2$ in pseudorapidity with full azimuth.

The basic unit of the FVTX is a *wedge*, which carries a mini-strip Si sensor, read-out chips, and a high-density interconnect, respectively. On the other hand, a complete FVTX is composed of two identical supermodules shaped in annular endcap, which consists of 4×2 layers of *half-disks* in z-direction and in azimuthal direction. Lastly each *half-disk* is composed of multiple unit of *wedges*.

Some main design parameters including segmentation are summarized in following Table 2.5.

Item	Value
Strip pitch (radial)	75 (μm)
Strip length (azimuthal, inner radius)	3.4 (mm)
Strip length (azimuthal, outer radius)	11.5 (mm)
Silicon sensor thickness	320 (μm)
Inner radius of silicon	44.0 (mm)
Silicon $\langle z \rangle$ offsets from the station (layer) center	$\pm 5.845, \pm 9.845$ (mm)
Nominal operating sensor bias	+ 70 (V)
Strips per column for small (large) <i>wedges</i>	640 (1664)
Strip columns per half-disk (2 per <i>wedge</i>)	48
$\langle z \rangle$ position of each station (layer)	$\pm 201.1, \pm 261.4, \pm 321.7, \pm 382.0$ (mm)

Table 2.5: Summary of FVTX design parameters

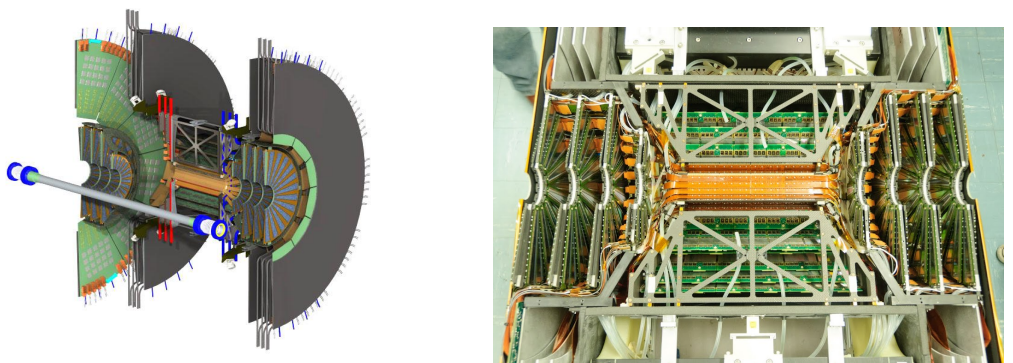
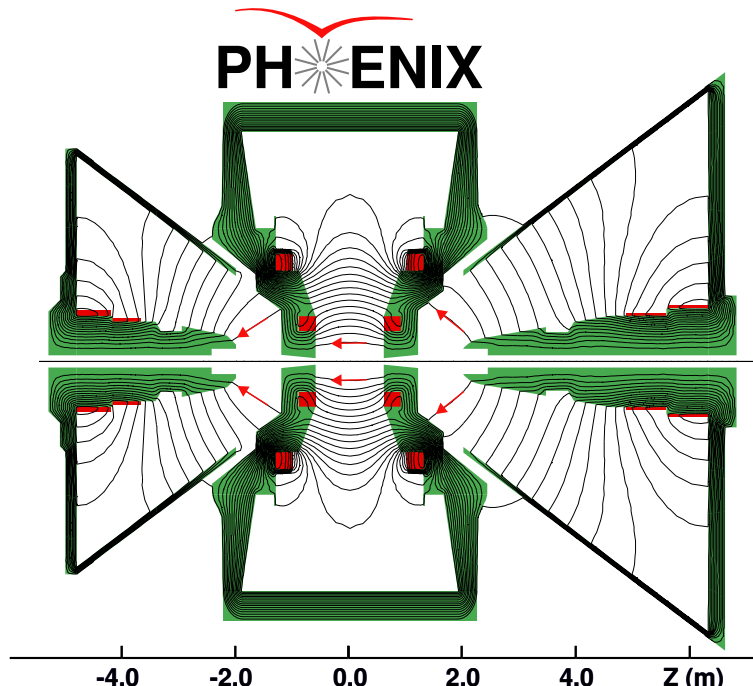


Figure 2.10: 3D layout (left) and a picture (right) of the completed half-detector of combined FVTX/VTX.

Muon Magnets [25] There exist two magnet systems in PHENIX: the Central Magnets in midrapidity and the Muon Magnets in forward rapidity, respectively. Some important parameters of the Muon Magnets are summarized in Table 2.6.

Item	Muon Magnet South	Muon Magnet North
Type	Two sloenoidal coils	
Field direction		Radial (\hat{r})
Field strength ($\int \vec{B} \cdot d\ell$)		0.72 T·m at $\theta = 15^\circ$
Acceptance (η)	$1.1 < \eta < 2.2$ ($12^\circ - 37^\circ$)	$1.1 < \eta < 2.4$ ($10^\circ - 37^\circ$)

Table 2.6: Summary of major parameters of Muon Magnets



Magnetic field lines for the two Central Magnet coils in combined (++) mode

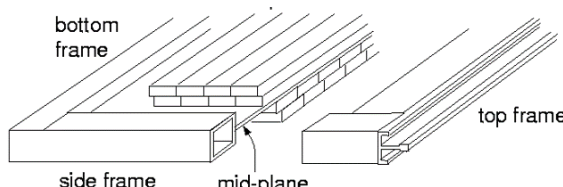
Figure 2.11: Sideview of PHENIX magnets. The dumbbell shaped structure in center is the Central Magnet and two truncated cone shaped structures in left and right are the Muon Magnets. The tapered pillar like structure inside Muon Magnet indicates Muon Piston.

MuID (Muon Identifiers) The MuID provides identification information of the muons. It plays role of a trigger detector in online data taking and a seed information provider in offline tracking. MuID covers whole η and ϕ acceptance of the MuTr.

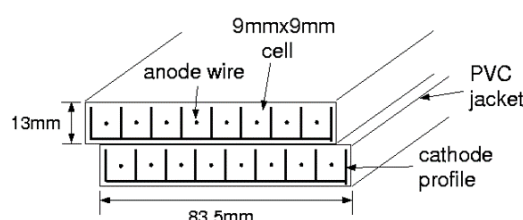
The basic unit of the MuID is a pair of Iarocci tube arrays named *two-pack*. An array of Iarocci tubes in a *two-pack* is shifted by a half-cell distance from another, where a Iarocci tube cell's dimension is 9×9 mm in a few m length. The structure of a *two-pack* can be found in Fig. 2.12.

On the other hand, the structure of a complete MuID can be explained separately in azimuthal direction or in z-direction. In azimuthal direction, the MuID is composed of 6 units of modules named *panel* (4 large + 2 small). A *panel* consists of a pair of *two-packs* arranged in horizontal and vertical direction. The structure of a *panel* can be seen in 2.12. In z-direction, the MuID is composed of 5 layer of modules named *gap* sandwiched by the steel walls (Table 2.4). A *gap* is composed of 2 *planes*, and a *plane* is composed of 6 *panels*. A complete structure of the MuID can be seen in Fig. 2.13. The total area covered by a *gap* is $12.5 \text{ m} \times 9.8 \text{ m}$.

Typically the MuID is operated by following conditions: mixed gas in the mixture of $\text{CO}_2 : \text{C}_4\text{H}_{10} = 0.92 : 0.08$ with $4300 \sim 4500$ V of high voltage. The expected multiplication gain is $\sim 2 \times 10^4$.



Cross section of the MuID panel



Cross section of the plastic tube(2-pack)

Figure 2.12: Structure of a MuID *panel* composed of a pair of *two-packs* (top) and Cross section of a *two-pack* (bottom).

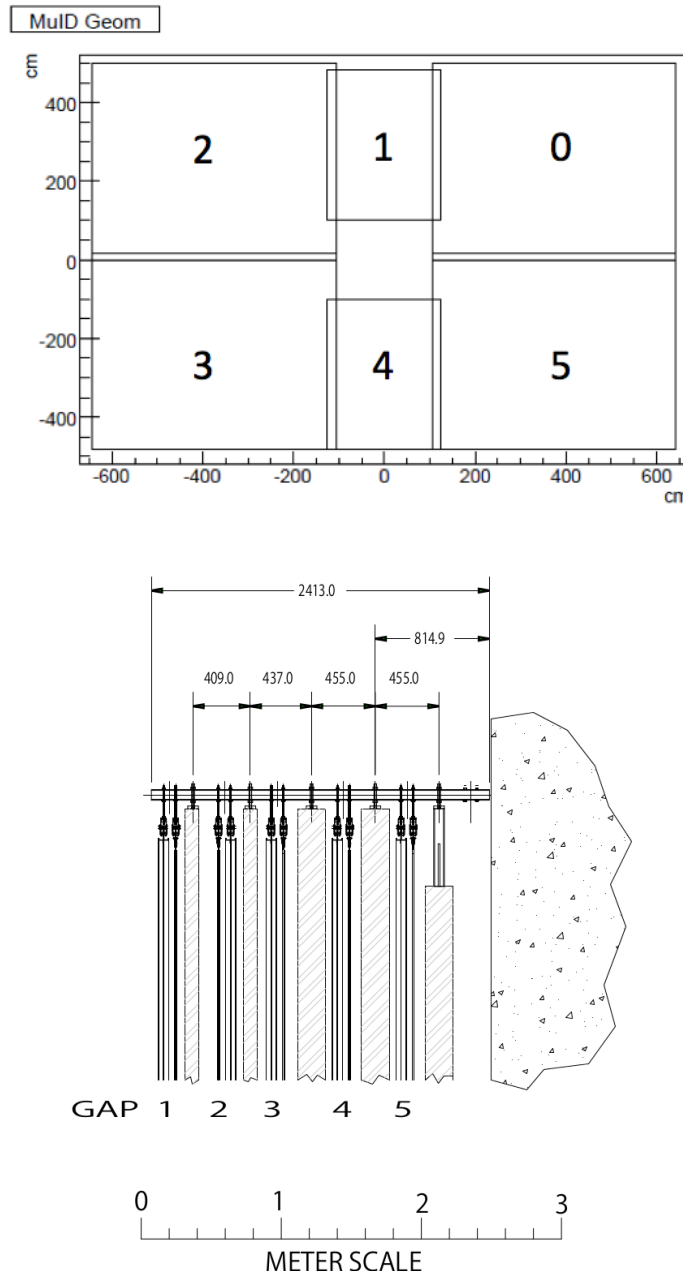


Figure 2.13: Structure of the MuID in beam view with *panel* numbering scheme (top)[8] and Structure of the MuID in sideview with *gap* numbering scheme (bottom)[7]. The numbering of the *gaps* start from 1 and increases with distance from the collision vertex. The hatched materials in sideview indicate steel wall absorbers. The bottom figure is quoted from [7].

MuTr (Muon Trackers) [22] The MuTr is one of two trackers in forward rapidity and provides main tracking information in Muon Arms. Combined with MuTRG and RPCs it also provides information for the online triggering. Each MuTr covers acceptance of roughly $1.2 < |\eta| < 2.2$ ($12.5^\circ - 35^\circ$) for South and $1.2 < |\eta| < 2.4$ ($10^\circ - 35^\circ$) for north with full azimuth.

A complete MuTr (South or North) is built inside of the Muon Magnet and composed of 3 stations. Numbering of each stations starts from 1 and increases as its distance from the collision vertex farther. Each station is composed of multiple units of CSC (Cathode Strip Chamber) in both azimuthal direction and z-direction. For instance, the St. 1 is consists of 4 identical segments named *quadrant* in azimuthal direction and 3 successive layers named *gap* in z-direction. The segmentations of each MuTr station can be found in Table 2.7.

Station	Segments in \hat{z}	Segments in $\hat{\phi}$	$\langle z \rangle$ (cm)
1	3 (gaps)	4 (quadrants) - 8 (octants)	189.0
2	3 (gaps)	8 (octants) - 16 (half octants)	313.5 (363.5)
3	2 (gaps)	8 (octants) - 16 (half octants)	448.5 (595.4)

Table 2.7: Segmentation of MuTr. The z distances without brackets indicate common or MuTr South while values with brackets indicate MuTr North.

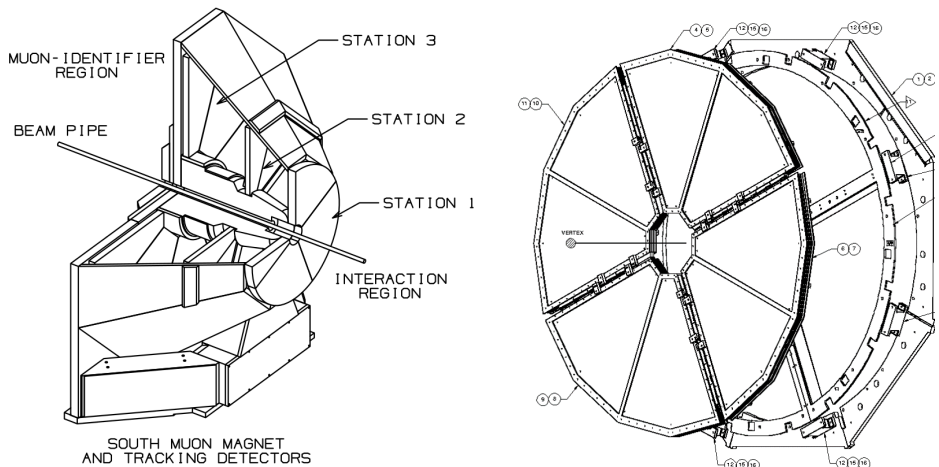


Figure 2.14: Schematic diagrams MuTr. Left figure shows whole MuTr South and Right figure shows *quadrants (half octants)* structure of MuTr St.1

Note that a *quadrant* of the St.1 is composed of 2 identical units called *octant* (for St.2 and St.3, ϕ segments are divided into 8 *octants* and 16 *half-octants*) and a *gap* in a station is a composition of 1 anode wire plane sandwiched between 2 cathode strip planes.

The anode planes are alternating structures of 20 μm gold-plated tungsten sense wires and 75 μm gold-plated copper-beryllium field wires running along $\hat{\phi}$ direction. The spacing between each sense wire is 10 mm and The spacing between a sense wire and a field wire is 5 mm. On the other hand, the cathode planes are a combination of \hat{r} direction cathode strips and alternate strips with various tilted angle. The pitch of each strip is 5 mm. In detail, half of the cathode planes have strips perpendicular to the anode wires and the other half have strips at tilted (*stereo*) angles between 0° and $\pm 11.25^\circ$ with respect to perpendicular strips. Typically the former is called as *non-stereo* plane and the latter is called as *stereo* plane. The distance between the *non-stereo* plane and *stereo* plane (i.e. *gap* thickness) is 6.35 mm. The alternating structure of the anode plane and The *non-stereo/stereo* structure of the cathode planes can be seen in Fig. 2.15. Also the *stereo* angle of the each gap can be found in Table 2.8.

In conclusion, the achievable position resolution is $\leq 100 \mu\text{m}$ for *non-stereo* planes; the resolution is worse for the *stereo* planes.

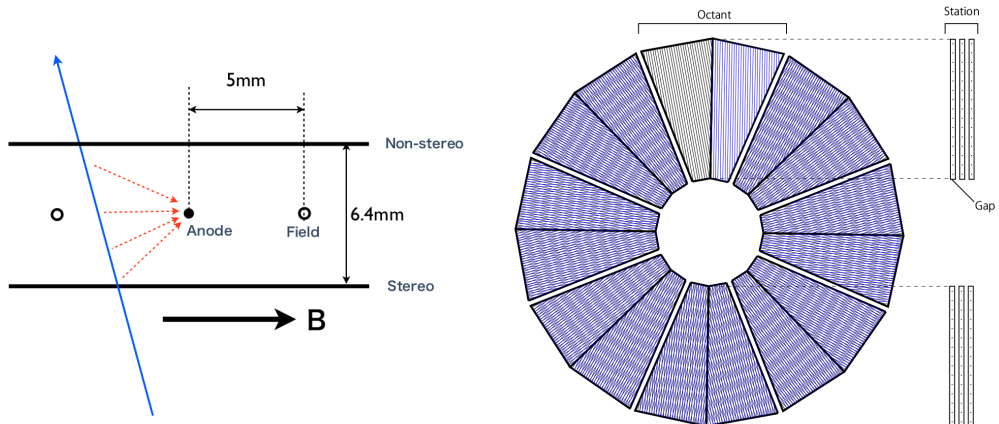


Figure 2.15: Alternating structure of the anode plane (left) and *non-stereo/stereo* structure of the cathode planes (right). The black lines indicate *non-stereo* plane and the blue lines indicate *stereo* plane. These figures are quoted from [7].

Station	ϕ angle offset of <i>stereo</i> cathode plane (deg)					
	Gap	Angle	Gap	Angle	Gap	Angle
1		- 11.25		+ 6.00		+ 11.25
2	1	+ 7.5 / - 7.5	2	+ 3.75 / - 3.75	3	+ 11.25 / - 11.25
3		- 11.25 / + 11.25		- 11.25 / + 11.25		×

Table 2.8: The ϕ angle offset of *stereo* cathode planes with respect to their corresponding *non-stereo* planes.

Lastly typical operation conditions of the MuTr are as follows: mixed gas in the mixture of $\text{Ar} : \text{CO}_2 : \text{CF}_4 = 0.5 : 0.3 : 0.2$ with ~ 1850 V of high voltage on anode wires. In this case typical multiplication gain is $\sim 2 \times 10^4$.

RPC (Resistive Plate Counters) The RPC provides fast timing information and used for the online triggering. Especially as a dedicated trigger detector for the $W \rightarrow \mu$ measurement, RPC's time resolution enables distinguishing the bunch crossing of each muon candidate. There exist two RPC stations in PHENIX Muon Arms: a smaller station named RPC1 which located between BBC and MuTr St.1 and a larger station named RPC3 which located in the downstream of the MuID, respectively. Note that though both of the RPC stations are commissioned in Run12 but only RPC3 is integrated to the online triggers. Each RPC stations roughly cover following η acceptance with full azimuth: $1.2 < |\eta| < 2.0$ for RPC1 and $1.4 < |\eta| < 2.6$ for RPC3, respectively.

The basic unit of both RPC1 and RPC3 is a double-gap resistive plate chamber based on endcap RPC technology for the CMS experiment at CERN. To distinguish the RPC stations at PHENIX Muon Arms from the basic unit, let the basic unit called as *module*. A *module* is made of a copper readout strip sandwiched by two gaps of oil-coated bakelite resistive plates (Fig. 2.16). The outer surface of each resistive plate is coated with graphite and works as electrode. In operational condition the readout strip reads image charge induced by two gaps. The structure of a *module* can be found in Fig. 2.16 and The design parameters of a *module* is summarized in Table 2.9.

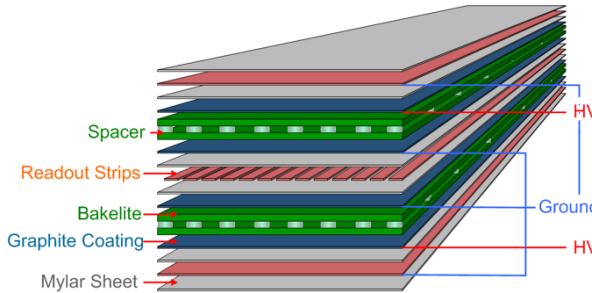


Figure 2.16: Cross-sectional layout of a RPC module.

Item	Value	Item	Value
Gap thickness	2 ± 0.1 (mm)	Resistivity	$1 - 6 \times 10^{10}$ ($\Omega \cdot \text{cm}$)
Time resolution	≤ 3 (ns) for MIP	Efficiency	> 95 % for MIP
Rate capability	0.5 (kHz/cm ²)	Noise rate	< 10 (Hz/cm ²)
Average cluster size	≤ 2 (strips)	Number of streamers	< 10 (%)

Table 2.9: Design criteria of the PHENIX RPC [16][17]

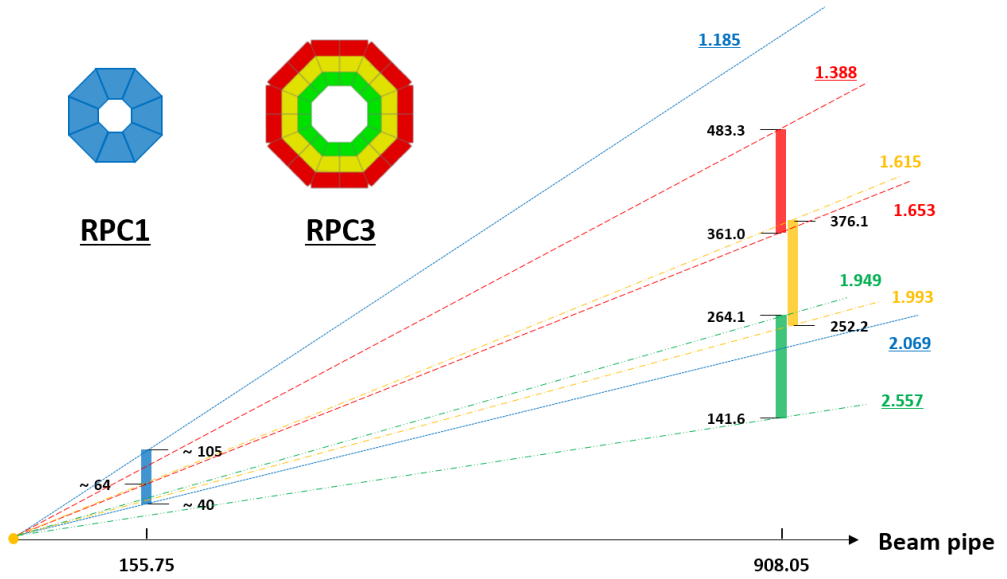


Figure 2.17: Layout of RPC1 and RPC3 in sideview. RPC3's ring-like structure with different colors indicates 3 different types of module of RPC3 (ex. innermost green ring indicates *RPC3A*).

Each station of RPC has following structure. The RPC1 is composed of 8 *modules* which called as *octant*. The RPC3 is composed of 16 supermodules called *half-octant* which is composed of 3 *modules*. Especially each module in RPC3 is called as *RPC3A*, *RPC3B*, and *RPC3C*, respectively. The structure of a RPC1's *octant* and a RPC3's *half-octant* can be seen in Fig. 2.17.

The position resolution of the RPCs are determined by the width of each *module*'s readout strip. The segmentation of a readout strip is differ from the module, but typically separated into 2-3 segments in radial direction and multiple segments in azimuthal direction with $\Delta\phi < 1^\circ$.

Typical operation conditions of the RPC are as follows: mixed gas in the mixture of $\text{C}_2\text{H}_2\text{F}_4 : \text{C}_4\text{H}_{10} : \text{SF}_6 = 0.95 : 0.045 : 0.05$ with 20 - 40 % of relative humidity. The applied high voltage is ~ 9500 V. Typical strip multiplicity under these conditions is 1.5 - 3.

ZDC (Zero Degree Calorimeters) The ZDC is one of two global detectors with the BBC. Main roles of the ZDC are as follows: minimum bias trigger by the energy measurement of the spectator neutrons and luminosity monitoring, respectively. It covers acceptance of ≤ 2 mrad and located at the 18 m distance from the collision vertex. The horizontal acceptance is ± 5 cm.

The ZDC is composed of 3 identical sampling hadronic calorimeter modules arranged in z-direction with a SMD (Shower Maximum Detector) sandwiched between the first module and the second module. Each hadronic calorimeter module is composed of 27 tungsten plate ($2 \lambda_n$, $50 X_0$) with optical fibers. To maximize the Cherenkov light from hadronic showers tungsten plates are tilted 45° with respect to the incident beam fragments. The energy resolution measured by emitted single neutrons is $\sim 10\%$ of $\sigma_E/E \leq 20\%$ at $E_n = 100$ GeV. On the other hand, the SMD is composed of two 5 mm thick scintillator arrays arranged in horizontal and vertical direction. The segmentation is 14 mm for horizontal direction and 19 mm in vertical direction. The position resolution of the SMD by the neutrons is ~ 1 cm.

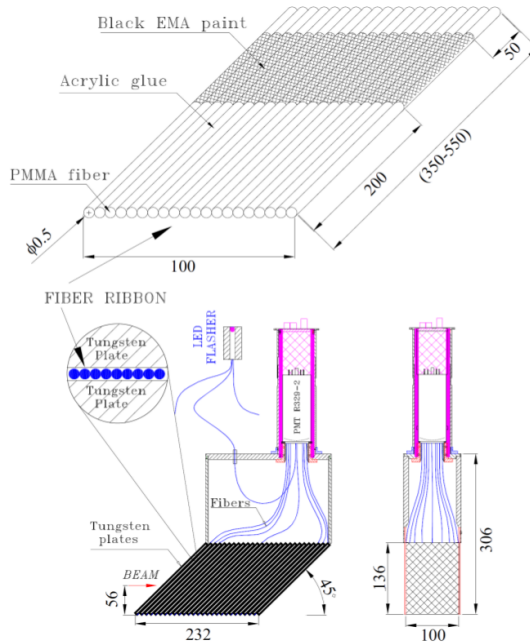


Figure 2.18: Mechanical design of the ZDC: a layer of optical fibers (top), sideview of a hadronic calorimeter module (bottom left), and beam view of a hadronic calorimeter module (bottom right), respectively. All units are mm. This plot is quoted from [9].

2.3 Data Acquisition

This section explains data acquisition process of the PHENIX DAQ and Triggering/Tracking at the Muon Arms.

2.3.1 DAQ System

The process of online data taking with PHENIX DAQ will be explained. First of all, the terms used in the PHENIX DAQ is summarized in following list with brief explanation.

1. Clock timing

- Clock: 9.4 MHz RHIC clock of the *Blue* beam
- MTM (Master Timing Module): receives Clock and fans it out to the GL1 and the GTM
- GTM (Granule Timing Module): receives Clock from the MTM and forwards it to the FEMs with Mode bits
- * Granule: minimal unit of hardware can be read out in PHENIX DAQ. A Granule is composed of 1 GTM with one or more FEM/DCM.
- * Mode bits: a series of predetermined routines (reset ADC baseline, schedule reset of the analogue memory unit, etc.) being sent to the FEM.

2. Data from individual detectors

- FEM (Front End Module): controls each detectors' FEE (Front End Electronics) and judge LL1 signal to be issued or not. If GL1 is issued send the data in corresponding timing to the DCMs.
- LL1 (Local Level 1 Trigger): level 1 trigger signals issued by individual detectors
- DCM (Data Collection Module): receives and packages data from the FEM. Then send it to the Partition and to the SEB. 4 DCM and 1 DSP compose a DCB (DCM Board).

3. Building physics event

- GL1 (Global Level 1 Trigger): receives Clock signal from the MTM and receives LL1 signals from the FEMs. Then issues the global trigger decision if LL1 condition is satisfied and any GTM is not busy.
- Partition: one or more Granules which receive the same triggers and busies. Up to 32 level 1 trigger can be operated simultaneously with maximum 128 independent triggers. Each partition operate in parallel and independent to each other.
- SEB (Sub Event Buffer): receives data from the DCM and forwards it to the ATP
- ATP (Assembly & Trigger Processor): receives and assembles the data from each SEBs, then send it to the buffer boxes for storage

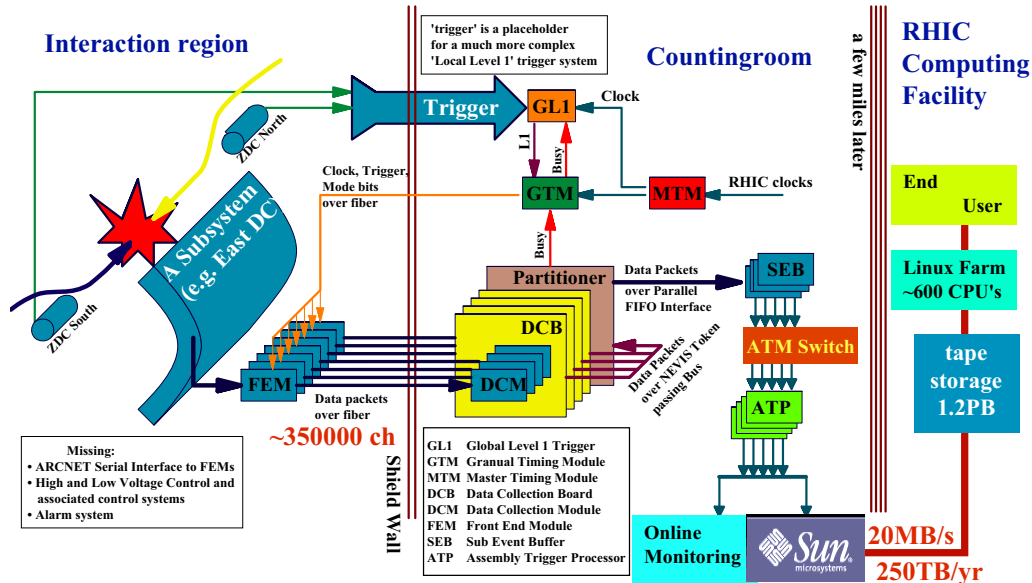


Figure 2.19: Data acquisition process

The Clock signal of the PHENIX DAQ is given by the RHIC. The MTM receives the Clock signal and forwards it to the GL1 and the GTM.

The GTM forwards the Clock signal again to the assigned FEM with Mode bits. The FEM process its input signals from the detector using the Clock signal and issues LL1 signal if required condition is satisfied. At the same time the FEM stores the results in buffer. The maximum delay of the buffer is 40 beam clock for all detectors.

The GL1 receives Clock signal from MTM and LL1 signals from the FEMs then judges if they match to any specific global level 1 pattern. If the pattern matches to certain global level 1 pattern and any of the GTM is not busy, then the GL1 issues a global trigger signal to the GTMs via MTM. The GTMs forward trigger signal again to the FEMs with delay, then the FEMs send the data in corresponding timing to the DCMs. These series of data taking can be performed without deadtime thanks to the event buffering system.

Once the data is transferred, the DCM process it further and send it to the the SEB. During this process multiple unit of DCMs are combined as a DCB unit, and again multiple unit of DCBs are combined as a Partition unit. The data collected in SEB is processed once again by ATPs, and finally sent to buffer boxes for storage.

2.3.2 Triggers

GL1 triggers, GL1p scaler, and Raw/Live/Scaled As explained in previous section PHENIX DAQ can operate maximum 32 GL1 (global level 1) triggers simultaneously without deadtime. However due to the limited DAQ bandwith not all of issued GL1 triggers can be accepted. Therefore in actual data taking operation certain prescale factor is applied to each GL1 triggers to scale down the number of accepted events. For instance, if a prescale factor of 10 is applied to a specific GL1 trigger, only 10 % of events triggered by the GL1 trigger will be recorded to the datafile. The prescale factor varies by physics interest and data taking operation condition.

The number of GL1 triggered events are counted by a scaler named GL1p. There exist 3 states for a GL1 triggered event: *raw*, *live*, and *scaled*, respectively. First, if an event is triggered by a GL1 trigger it automatically satisfies *raw* state. Second, in addition to the *raw* state, if any of the GTMs is not busy, in other words if the DAQ is able to process the event it satisfies *live* state. Third and Finally, in addition to the *live* state if the event is actually recorded it satisfies *scaled* state. As already explained not all of GL1 triggered event are recorded due to the prescale. The events with *scaled* state are mean the events actually recorded in the datafile. In short, each state can be summarized as follows.

- *raw*: GL1 trigger is fired
- *live*: GL1 trigger is fired + DAQ is available to process the event
- *scaled*: GL1 trigger is fired + DAQ is available to process the event + prescale is applied

Each GL1 trigger is composed of at least more than 1 LL1 (local level 1) triggers. For instance, the minimum bias trigger without vertex requires only 1 LL1 trigger (BCCLL1(>tubes)novertex) but one of the $W \rightarrow \mu$ triggers in Run 12 requires 3 LL1 triggers at the same time. The GL1 triggers employed in Run 12 are summarized in following Table 2.10.

Name	Bit mask	Abbr. ¹	Type	Order ¹
BBCLL1(>0 tubes)	0x1	BBC30cm	MB	0
BBCLL1(>0 tubes) novertex	0x2	BBCnoVtx		1
ZDCLL1wide	0x4		0T	2
BBCLL1(noVtx)&(ZDCN ZDCS)	0x8			3
BBCLL1(>0 tubes) narrowvtx	0x10	BBC15cm	MB	4
ZDCNS	0x20		0T	5
ERT_4x4b	0x40		ERT	6
ERT_4x4a&BBCLL1	0x80			7
ERT_4x4c&BBCLL1(narrow)	0x100			8
ERTLL1_E	0x200			9
ERTLL1_E BBCLL1(narrow)	0x400			10
CLOCK	0x800		0T	11
MPC_B	0x1000		MPC	12
MPC_A	0x2000			13
MPC_C&ERT_2x2	0x4000			14
(MPCS_C&MPCS_C) ((MPCN_C & MPCN_C)	0x8000			15
((MUIDLL1_N2D S2D) ((N1D&S1D))&BBCLL1(noVtx)	0x10000	MUID2D	Muon	16
(MUIDLL1_N1D S1D)&BBCLL1(noVtx)	0x20000	MUID1D		17
(MUON_S_SG1&MUIDLL1_S1D)	0x40000	R12W1		18
(MUON_N_SG1&MUIDLL1_N1D)&BBCLL1(noVtx)				
MUON_S_SG3&MUIDLL1_S1D&BBCLL1(noVtx)	0x80000			19
MUON_N_SG3&MUIDLL1_N1D&BBCLL1(noVtx)	0x100000			20
(MUON_N_SG3&MUIDLL1_N1H)	0x200000			21
(MUON_S_SG3&MUIDLL1_S1H)&BBCLL1(noVtx)				
MUON_S_SG3&BBCLL1(noVtx)	0x400000			22
MUON_N_SG3&BBCLL1(noVtx)	0x800000			23
MUON_S_SG1&BBCLL1(noVtx)	0x1000000			24
MUON_N_SG1&BBCLL1(noVtx)	0x2000000			25
MUON_S_SG1_RPC3_1_A B C&BBCLL1(noVtx)	0x4000000	R12W2_S		26
MUON_N_SG1_RPC3_1_A B C&BBCLL1(noVtx)	0x8000000	R12W2_N		27
PPG(Pedestal)	0x10000000		Service	28
PPG(Test Pulse)	0x20000000			29
PPG(Laser)	0x40000000			30
Noise	0x80000000			31

¹ Unofficial convention (only used in this thesis)

Table 2.10: Table of triggers for Run12 p + p at 510 GeV

BBCLL1 (MinBias) The BBCLL1 (Local level 1) triggers are the minimum bias triggers in data acquisition at PHENIX. There are 3 types of BBCLL1 triggers in Run 12:

- BBCLL1(>0 tubes) novertex
- BBCLL1(>0 tubes) (BBC 30 cm)
- BBCLL1(>0 tubes) narrowvtx (BBC 15 cm)

The minimum condition of the BBCLL1 trigger is having at least 1 hit in each side of BBC module (South and North). Then the event categorized into 3 types by the z-vertex difference from the zero point: no z-vertex condition is required (novertex), z-vertex is located within 30 cm from the zero point, and z-vertex is located within 15 cm from the zero point, respectively. The z-vertex distance is obtained by using the Eq. 2.6.

ERT and MPC The ERT triggers are used for the measurement at Central Arms. It is triggered by measuring the deposited energy in certain group of EMCAL towers (Fig. 2.20). Similar to the ERT triggers MPC triggers are used for the measurement at the MPC, and it also triggered by measuring the energy deposited in the MPC towers.

These two group of triggers are completely irrelevant to the data acquisition at Muon Arms, however, they are indirectly utilized in this analysis for the measurement of Muon Arm triggers' efficiency.

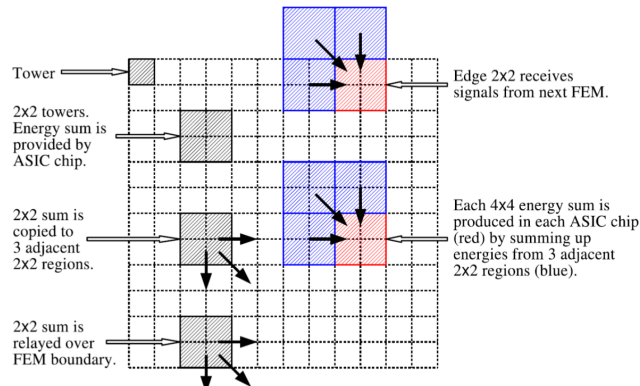


Figure 2.20: Schematic diagram of ERT triggers

MuIDLL1 The MuIDLL1 uses hit pattern among MuID gaps to issue the LL1 trigger condition. When a particle is originated from the collision vertex and passes through the MuID the MuID’s tubes will be fired along the trajectory the particle draw. Though these fired tubes are located in different MuID gaps, this group of tubes along the trajectory can be treated as a logical detector. This logical detector called as *symset*, and the judgment of the MuID trigger is based on the hit pattern of multiple *symsets*. Note that by the structure of the MuID the *symset* can be defined independently along vertical tubes or horizontal tubes.

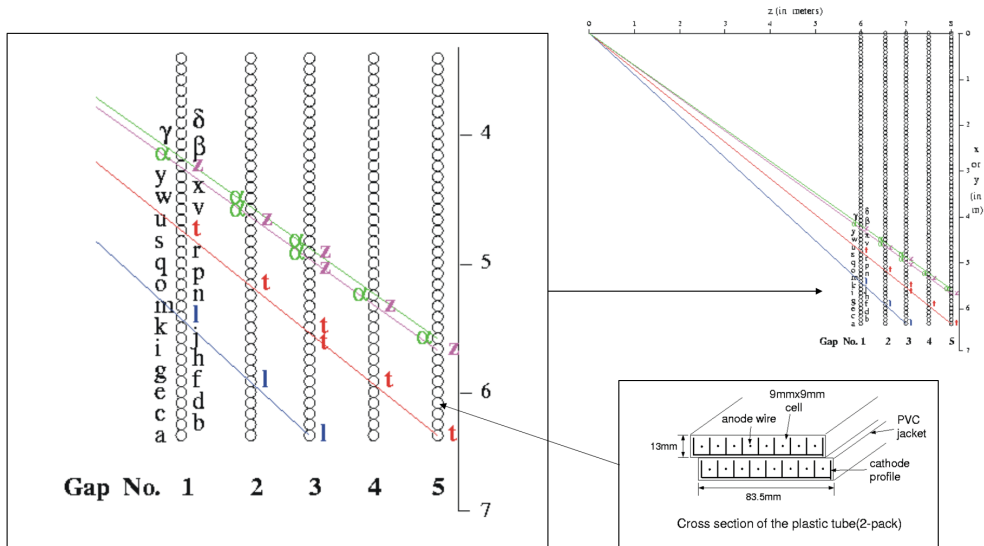


Figure 2.21: Example of MuID *symsets*. The tubes (*two-packs*) along same *symset* share same index (ex. *α*, *z*, *t*, *l*).

There are two main *symset* logics in Run 12: the 1D (one-deep) and the 1H (one-hadron), respectively. Both of the logics used for the identification of single tracks, however, the former targets muons while the latter targets hadrons. The logic diagram of 1D and 1H can be found in Fig. 2.22.

The trigger decision of the MuID can be done with multiple tracks, either: for instance 2D (two-deep) or 1D1H (one-deep, one-hadron). Note that the 2D is not a simple AND condition of two 1D but the opening angle between two tracks is considered as well.

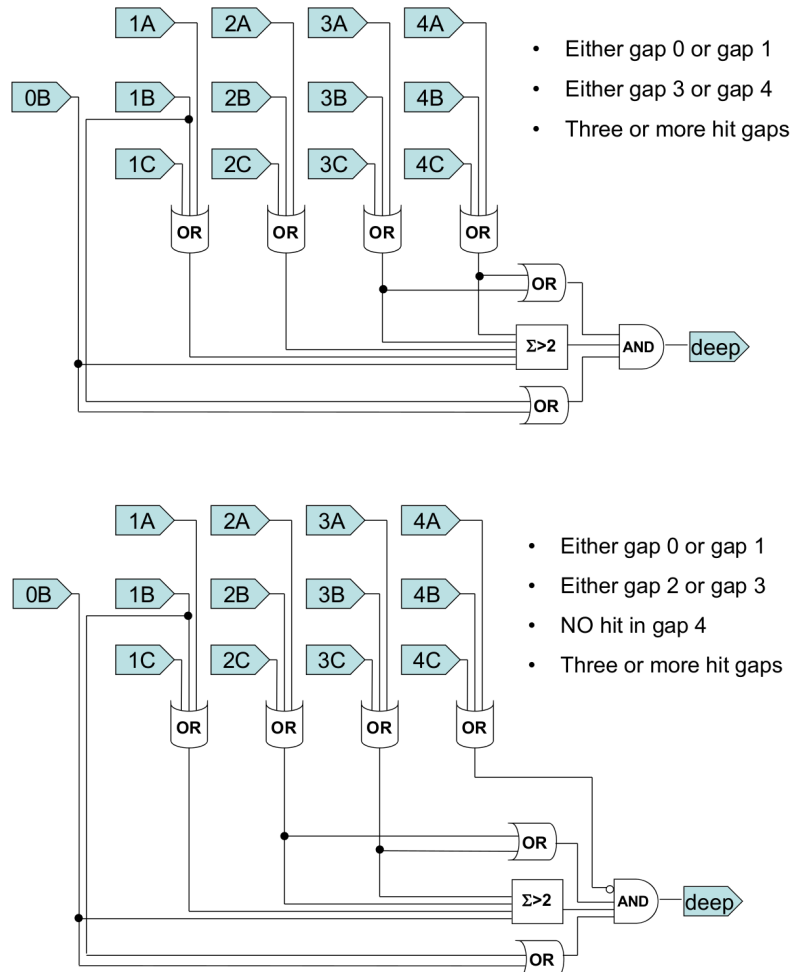


Figure 2.22: Logic diagram of MuID1D (top) and MuID1H (bottom). Note that the number of each diagram indicates MuID gaps (ex. 0 for gap 1).

In Run 12 $p + p$ data taking period following two MuIDLL1 triggers are employed.

- $((\text{MUIDLL1_N2D} \parallel \text{S2D}) \parallel (\text{N1D} \& \text{S1D})) \& \text{BBCLL1}(\text{noVtx})$
- $(\text{MUIDLL1_N1D} \parallel \text{S1D}) \& \text{BBCLL1}(\text{noVtx})$

MuTRG (SG) [26] The MuTRG-LL1 or simply the SG (Sagitta) triggers are newly introduced high momentum muon triggers which use the hit patterns of the MuTr. All of physics triggers for $W \rightarrow \mu$ include MuTRG trigger, especially the SG1. To describe the MuTRG one need to explain the recent fast readout electronics upgrade (MuTRG-FEE) on MuTr FEE. Due to the low intrinsic timing resolution ($\sim 2\text{-}3$ beam clock), MuTr itself cannot be used alone for the triggering. Therefore MuTRG-FEE are additionally attached on the MuTr's non-stereo cathode planes.

The MuTRG-FEE system is composed of 3 main parts: MuTRG-ADTX (signal amplifier and discriminator), MuTRG-MRG (merger), and MuTRG-DCMIF (interface board with the DCM), respectively. The signal process via MuTRG-FEE can be explained as follows: $\sim 6\%$ of signal charge from the MuTr's non-stereo cathode planes split into MuTR-ADTX, then MuTr-ADTX digitize and send it to the MuTRG-MRG. The MuTRG-MRG buffers the data (i.e. the hit information of the strips) from multiple MuTRG-ADTXs and send it to the LL1 board for the trigger decision. Once the trigger issued, the MuTRG-MRG multiplex the patterns of 7 beam clock ($-3 \leq \text{Trigger issued beam clock} \leq +3$) and send it to the DCM via MuTRG-DCMIF. Note that among these processes the MuTRG-MRG extends the timing width of the hit to multiple beam clocks: by using this extended timing width low intrinsic timing resolution of the MuTr can be overcome.

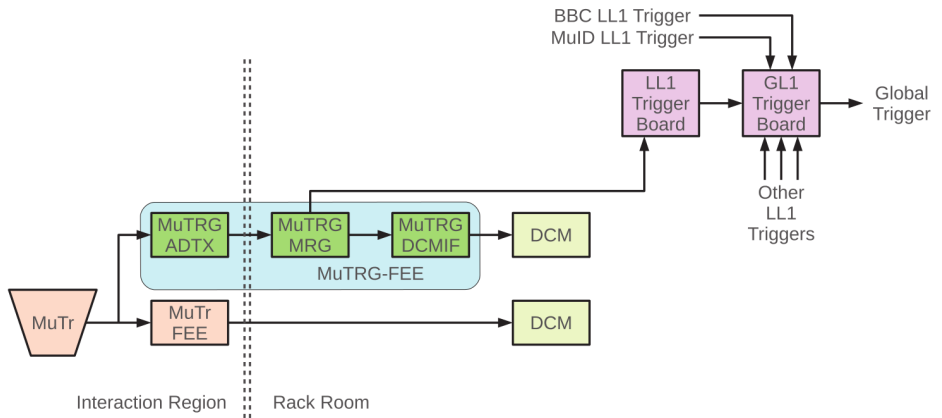


Figure 2.23: Signal process of MuTRG-FEE.

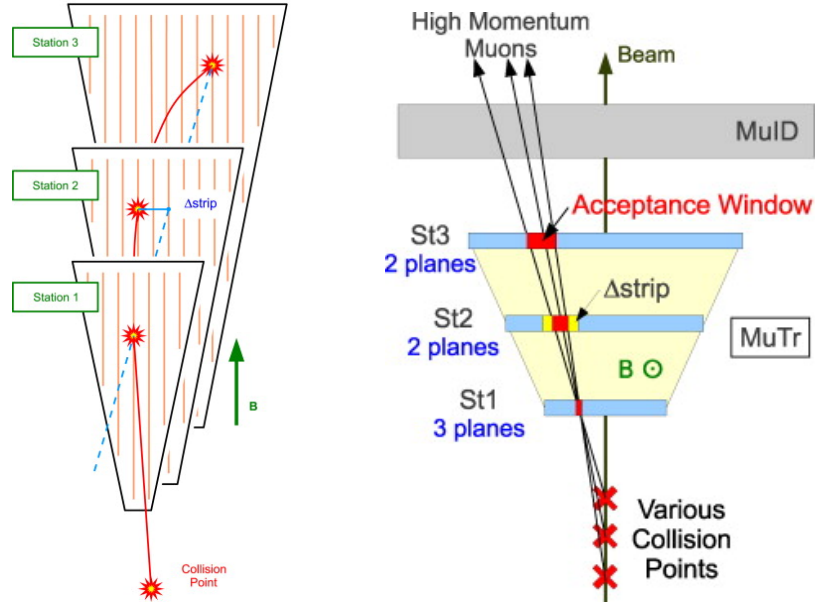


Figure 2.24: Schematic diagrams of MuTRG trigger

The trigger decision of the MuTRG-FEE is based on the sagitta drawn by the track. If a very high-momentum track is passes through the MuTr, its size of bending inside MuTr should be relatively small (i.e. close to the straight line) compared to the low-momentum tracks. The parameter of the decision is Δstrip (sagitta) measured in MuTr St.2. As explained already MuTRG-MRG sends the hit information of the strips from multiple MuTRG-ADTXs to the LL1 board. By using these hit informations on St. 1 and St. 3 a straight line can be drawn, then by measuring the number of strips away from the straight line (Δstrip) at St. 2 the size of the sagitta can be obtained for the trigger decision (Fig. 2.24).

Note that the MuTRG triggers are not used alone but always combined with other timing based triggers such as MuIDLL1 or RPCLL1. The MuTRG trigger used in $W \rightarrow \mu$ is the SG1 ($\Delta\text{strip} < 1$), however, SG3 triggers also employed in Run 12 p + p data taking period.

In Run 12 p + p data taking period total ten SG combined triggers are employed, however, following two types of triggers are used as main physics triggers in $W \rightarrow \mu$. The other employed SG triggers can be found in Table 2.10.

- $(\text{MUON_S_SG1\&MUIDLL1_S1D}) || (\text{MUON_N_SG1\&MUIDLL1_N1D}) \& \text{BBCLL1}(\text{noVtx})$
- $\text{MUON_S_SG1_RPC3_1_A} || \text{B} || \text{C} \& \text{BBCLL1}(\text{noVtx})$
- $\text{MUON_N_SG1_RPC3_1_A} || \text{B} || \text{C} \& \text{BBCLL1}(\text{noVtx})$

2.3.3 Track Reconstruction

A detailed explanation of track reconstruction in Muon Arms can be found in Ch. 4 of the [7]. Only a brief scheme of the single track reconstruction will be given in this section.

The track reconstruction in the Muon Arms starts with finding seed in the MuID. MuID is located outside of Muon Magnets and has multiple layer (*gap*) of XY readout structure. The particle incident from the collision vertex passes through the MuID straightly and leaves hit in horizontal tubes and vertical tubes individually. One can imagine the 1D trajectory in the MuID tubes by the pass-through particle: it is called as the *road*. The *road* is searched for X and Y individually and combined later as a 2D *road*. Typically the *gap* 2 or *gap* 3 is used as start hit position to find the *road*. The *road* finding algorithm search the *road* by following orders:

$$\begin{array}{ccccccc} \text{gap 2} & \rightarrow & \text{gap 3} & & & & \\ & \rightarrow & & \text{gap 1} & \rightarrow & \text{gap 4} & \rightarrow \\ \text{gap 3} & \rightarrow & \text{gap 2} & & & & \text{gap 5} \end{array}$$

As a next step, one optimal 2D *road* from MuID is projected into nearest MuTr station. Note that the hits in MuTr stations are considered in the order of outer station to inner stations. Similar to the MuID, MuTr has its own 2D readout structure composed of multiple cathode planes. The track reconstruction in the MuTr can be summarized in 3 steps: find hit position in each cathode strips (*coordinates*) by using Mathieson function, search possible passage of charged particle in each cathode planes (*stubs*) by searching algorithm, and compose a track from 3 *stubs* in each MuTr station by bend-plane fitting, respectively. Once the track is reconstructed successfully the track is fitted with Kalman fitting.

The reconstructed track after Kalman fitting is extrapolated to MuID to refine the MuID *road*. In addition the track extrapolated further in downstream direction to find the matching hit in RPC3, or extrapolated in upstream direction to find the matching hit in RPC1 or FVTX.

Chapter 3

Dataset

3.1 Overview

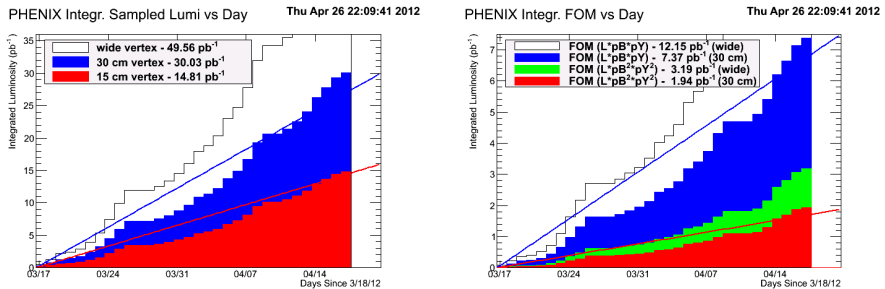


Figure 3.1: Integrated luminosity (left) and its Figures of Merit (right) in Run 12 [10]

The dataset used in this analysis is obtained in longitudinal $p + p$ collision at $\sqrt{s} = 510$ GeV in 2012. During the operation the RHIC can maintain beams about 8 hours: this a stable, long maintained beam is called as a *Fill*. Also typical DAQ operation in PHENIX keep in 1 hour length: this 1 hour length data unit is called as a *run*. Note that this 1 hour unit will be denoted in small letter to distinguish it from the data taking period in 2012 (Run 12). The data is obtained from March 12 to April 19 and collected via PHENIX Muon Arms with all of muon triggers. The collected data is cross checked by following items: Data taking conditions (DAQ status, beam polarization, magnetic field, etc.), Muon Arms' reconstruction response, RPCs operation conditions, and Single muon yields [27]. In conclusion, total 49 *Fills* (16593 - 16735) and 311 *runs* (364822 - 368798) are selected for the data analysis.

3.2 Integrated Luminosity

For the integrated luminosity ($\int L dt$) estimation the minimum bias trigger without vertex cut (BBCLL1(>0 tubes) novertex) is used. The trigger is fired when both BBC have a hit within valid time domain (coincidence), and each detected hit in BBC is originated from the inelastic proton-proton collisions. Therefore the BBC efficiency comes in during the calculation of integrated luminosity. Related to the total inelastic proton-proton collision cross section, the luminosity measured by the minimum bias trigger can be defined as follows:

$$\begin{aligned} L &= \frac{R_{\text{BBC}}}{\sigma_{\text{BBC}}} \\ &= \frac{R_{\text{BBC}}}{\epsilon_{\text{BBC}} \cdot \sigma_{pp}^{\text{total}}} \end{aligned} \quad (3.1)$$

where R_{BBC} indicates minimum bias trigger rate, σ_{BBC} indicates BBC cross section, ϵ_{BBC} indicates BBC efficiency, and $\sigma_{pp}^{\text{total}}$ indicates total inelastic proton-proton collision cross section, respectively.

Therefore to estimate the integrated luminosity σ_{BBC} and R_{BBC} are required. Especially since there exist pileup effect due to multiple collisions per crossing, there exist clear discrepancy between the observed BBC trigger rate $R_{\text{BBC}}^{\text{observed}}$ and the true BBC trigger rate $R_{\text{BBC}}^{\text{true}}$ thus it should be corrected. The σ_{BBC} can be obtained by specific analysis named Vernier scan (Van der Meer scan) and The pileup effect can be corrected by special analysis technique defined in PHENIX.

According to the Vernier scan analysis by using Run 9 p + p at $\sqrt{s} = 510$ GeV ([28]) the σ_{BBC} and its corresponding ϵ_{BBC} are estimated as follows.

$$\begin{aligned} \sigma_{\text{BBC}} &= 32.51 \pm 1.19 \text{ (stat)} \pm 3.01 \text{ (syst)} \text{ (mb)} \\ \epsilon_{\text{BBC}} &= 0.53 \end{aligned} \quad (3.2)$$

On the other hand, the pileup effect on the $R_{\text{BBC}}^{\text{observed}}$ can be corrected by following equations. The induction of the equation can be found in Section 5.1.2 of [7].

$$\begin{aligned} R_{\text{BBC}}^{\text{observed}}(\mu) &= 1 - e^{-R_{\text{BBC}}^{\text{true}}(1+k_S)} - e^{-R_{\text{BBC}}^{\text{true}}(1+k_N)} + e^{-R_{\text{BBC}}^{\text{true}}(1+k_S+k_N)} \\ R_{\text{BBC}}^{\text{true}} &= \mu \epsilon_{\text{BBC}}, \quad k_S = \frac{\epsilon_S}{\epsilon_{\text{BBC}}}, \quad k_N = \frac{\epsilon_N}{\epsilon_{\text{BBC}}} \end{aligned} \quad (3.3)$$

where μ indicates average number of collisions per bunch crossing assumming Poisson distribution, ϵ_{BBC} indicates probability of both BBC have a hit, in other words BBC efficiency, $3\epsilon_{S(N)}$ indicates probability of exclusive hit on BBC south (north), respectively. Note that the μ is usually called as *Multiple collision parameter*.

In conclusion, final integrated luminosity and related parameters are as follows. Note that these values are based on the pileup correction study by analyzer Sanghwa Park [29].

- $k_S = 0.223$
- $k_N = 0.224$
- $L^{observed}$ (before correction): 44.9 pb^{-1}
- L^{true} (after correction): 53.1 pb^{-1}

3.3 Hit Efficiency

3.3.1 MuID

There are a couple of methods for the MuID hit efficiency measurement: data driven method by using offline reconstructed *roads* and HV method by using current draw in MuID HV chain. In this analysis the efficiency is measured by the HV method due to limited data statistics.

As explained in section 2.2.2 the MuID is composed of 5 *gaps* in beam direction and 6 *planes* in azimuthal direction. Note that a *gap* has two *planes* (one horizontal *plane* and one vertical *plane*). Lastly, a *plane* has multiple unit of HV groups. Fig. 3.2 shows HV groups in vertical *plane* and horizontal *plane*.

By using the current draw in a HV group the existence of a hit can be judged. Note that the efficiency of the tubes in same HV group are assumed to be same. The efficiency of MuID *planes* can be estimated as follows:

$$\epsilon_{plane} = \frac{\text{Hit in the } plane}{\text{roads associated with MuTr tracks}} \quad (3.4)$$

Note that a MuTr track requires MuID *road* finder and trigger emulator. Also following quality cuts are applied in the selection of event samples. By using this method, all of MuID *planes* efficiency is measured. The Fig. 3.3 shows an example of the measured efficiency of a *plane*.

- Distance between the MuID *road* and MuTr track < 20.0 (cm)
- $|p_z| > 1.3$ (GeV/c)
- Both *planes* in a *gap* has hit

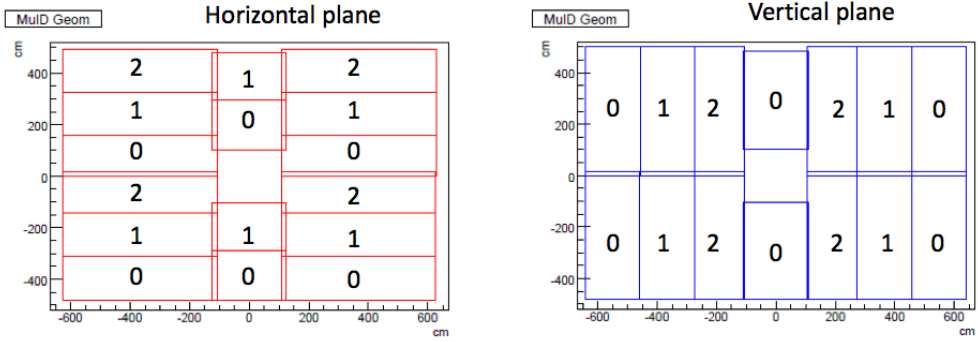


Figure 3.2: HV groups of horizontal *plane* (left) and vertical *plane* (right) of MuID. A large *plane* has 3 HV groups and A small *plane* has 2 groups. This plot is quoted from [8].

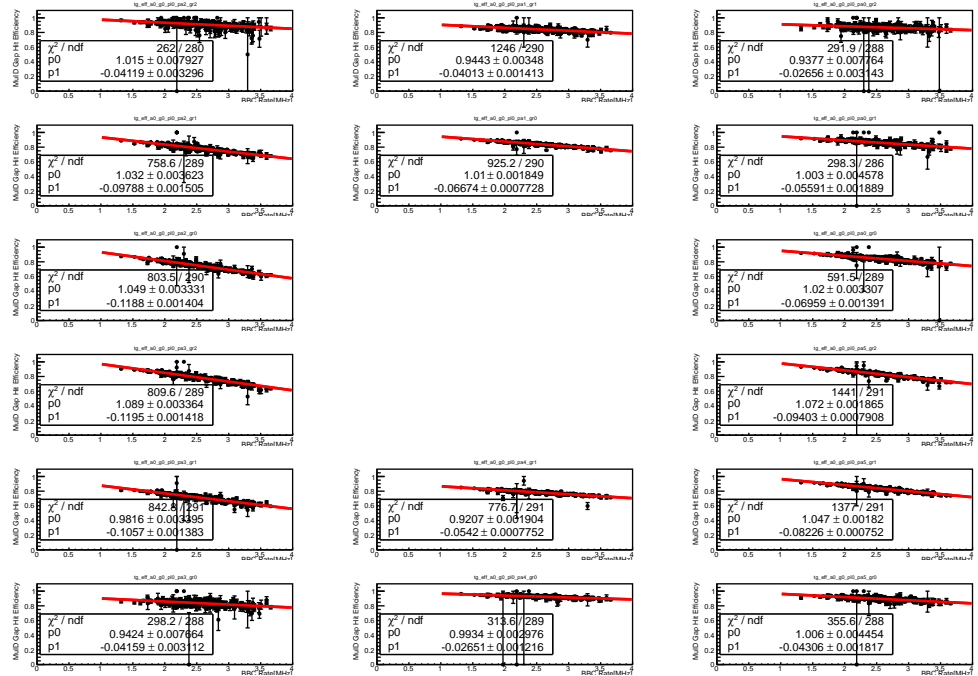


Figure 3.3: Hit efficiency of MuID south gap 0 horizontal *plane* vs. BBC rate (MHz). Each histogram corresponds to the HV group in the position. This plot is quoted from [8].

3.3.2 MuTr

MuTr in a Muon Arm is composed of 8 *gaps* which consists of 2 *planes*. Therefore maximum 8×2 number of hits can be exist for a reconstructed track. If a particle pass through a *gap* and hits recorded in both *planes*, there will be clear correlation as they originated from same energy deposition. Therefore following two probability parameters are considered in efficiency estimation.

- p_1 : probability of two *planes* of a *gap* have at least one hit (OR hit)
- p_2 : probability of two *planes* of a *gap* have only one hit (p_1 AND only 1 hit)

Then under the assumption of two *planes*' performance in a *gap* are uniform hit efficiency of each *gap* and *plane* is defined as follows.

$$P_k = {}_n C_k p_1^k (1 - p_1)^{n - k}, \quad (0 \leq k \leq n)$$

$$P_i = \sum_{\frac{i}{2} \leq k \leq i} {}_n C_k p_1^k (1 - p_1)^{n - k} {}_k C_{2k - i} (1 - p_2)^{i - k} p_2^{2k - i}, \quad (k \leq i \leq 2k) \quad (3.5)$$

where n indicates total number of *gaps* in a Muon Arm (8), k indicates number of *gaps* have a hit, and i indicates the number of *planes* have a hit, respectively. By fitting the number of hit distribution of the data with Eq. 3.5, p_1 and p_2 can be obtained. Once p_1 and p_2 are obtained then finally *gap* efficiency and *plane* efficiency can be estimated as follows. Note that the *gap* efficiency indicates efficiency for both *planes* have hits.

$$\epsilon_{gap}^{AND} = p_1 (1 - p_2)$$

$$\epsilon_{plane} = p_1 (1 - \frac{p_2}{2}) \quad (3.6)$$

The *run by run* *gap* efficiency and *plane* efficiency can be seen in Fig. 3.4. As the results shows there exist apparent negative correlation between the efficiency and the luminosity. Therefore the final base efficiency and asymmetry width are depend on the multiple collision condition μ as follows [8].

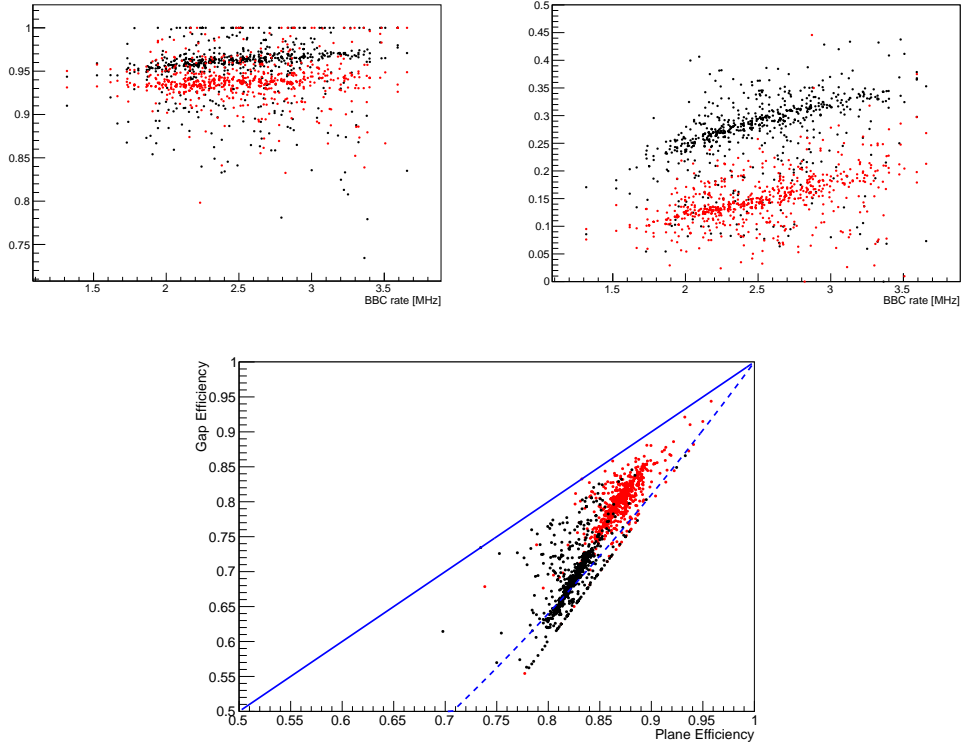


Figure 3.4: *run by run* p_1 (top left) and p_2 (top right) of MuTr vs. BBC rate (MHz) and Correlation between *gap* efficiency and *plane* efficiency (bottom). The Blue solid line indicates full correlation between two efficiencies while The Blue dashed line indicates no correlation. Red dots indicates MuTr south and Black dots indicate MuTr north. These plots are quoted from [8].

- Base efficiency
 - o MuTr south: $0.9725 - 0.0526\mu + 0.0275\mu^2$
 - o MuTr north: $0.9534 - 0.0084\mu - 0.1307\mu^2$
- Asymmetry width
 - o MuTr south: $0.3472 + 1.070\mu - 1.282\mu^2 + 3.213\mu^3$
 - o MuTr north: $0.4322 + 0.036\mu + 3.763\mu^2 - 1.425\mu^3$

3.3.3 RPC

The hit efficiency of the RPC is measured with Tag & Probe method by using dimuon samples. The conditions used for the measurement are as follows. Each kinematic variables' definition can be found in later section 4.2.1.

- Dimuon events selection
 - Events with two reconstructed tracks in MuTr
 - Triggered W trigger independent of RPC (R12W1 in Table 2.10)
 - $2.5 < m_{inv} < 100$ (GeV/c 2)
 - $|\phi_1 - \phi_2| > 1.2$ (rad) (jet rejection)
- Tag side cuts
 - $\chi^2 < 7.0$
 - $DCA_r < 12.0$ (cm)
 - $DG0 < 4.0$ (cm)
 - $DDG0 < 2.2$ (deg)
 - $lastGap = 4$
- Probe side cuts (denominator)
 - $\chi^2 < 20.0$
 - $DG0 < 20.0$ (cm)
 - $DDG0 < 2.2$ (deg)
 - $lastGap = 4$
- Probe pass cut (numerator): $0 < RPC3DCA < 100$ in addition to Probe side cuts

To estimate the efficiency precisely the purity of dimuon events need to be estimated. Therefore the unlike-sign events' efficiency and like-sign events' efficiency are measured separately in order to subtract the combinatorial backgrounds from the dimuon sample. The efficiencies for each case can be found in Fig. 3.5. When combinatorial backgrounds' ratio among the dimuon sample is p , the true hit efficiency by the dimuons can be expressed as follows.

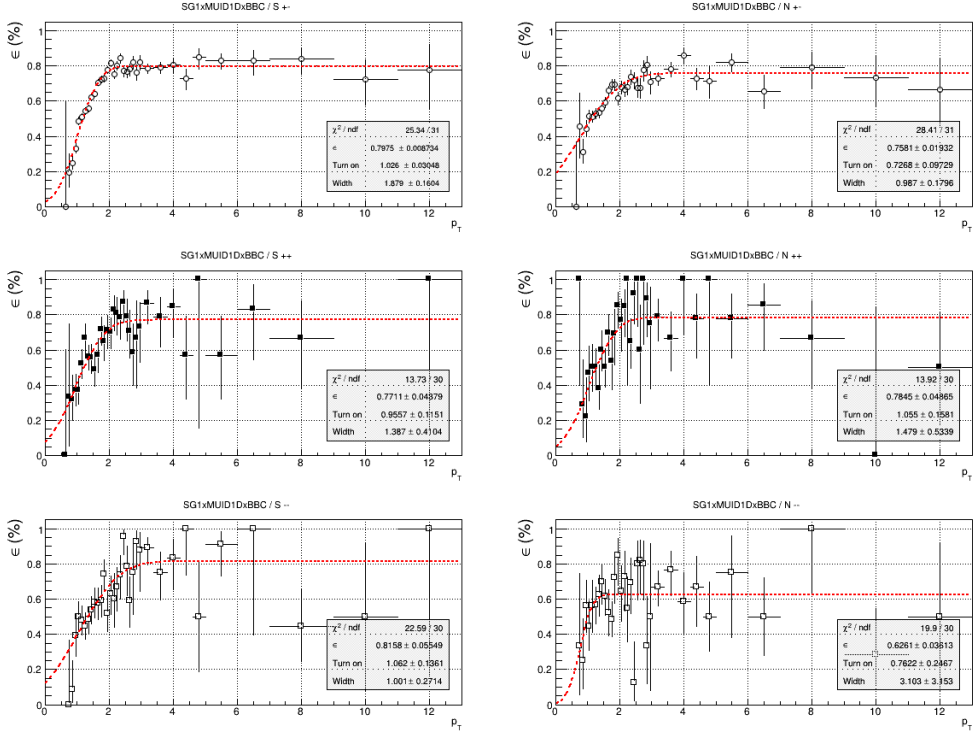


Figure 3.5: RPC efficiencies for unlike-sign events (top) and like-sign events (middle and bottom). Each column shows results of RPC3 south (left) and north (right).

$$\epsilon_{(+-, \text{observed})} = p \epsilon_{(+-, \text{true})} + (1 - p) \epsilon_{\text{comb}}$$

$$p = \frac{N_{(+-)} - N_{\text{comb}}}{N_{(+-)}} \quad (3.7)$$

$$N_{\text{comb}} = 2 \sqrt{N_{(++)} \times N_{(--)} }$$

where $\epsilon_{(+-, \text{observed})}$ indicates observed unlike-sign efficiency, $\epsilon_{(+-, \text{true})}$ indicates true unlike-sign efficiency, ϵ_{comb} indicates like-sign efficiency, and N indicates number of muons in each sign condition. Note that the $\epsilon_{(+-, \text{true})}$ is obtained by combining $(++)$ and $(--)$. The final backgrounds subtracted $\epsilon_{(+-, \text{true})}$ are as follows:

- RPC3 south: 0.802 ± 0.0341
- RPC3 north: 0.732 ± 0.0254

3.4 Trigger Efficiency

During the reconstruction of single muon dataset all of muon triggers in Table 2.10 are used to acquire as many as muon candidates. Therefore to estimate the representing trigger efficiency all related trigger conditions are need to be considered. Especially following two items are essentially required: fraction of events triggered by specific trigger and the trigger's efficiency, respectively.

However direct estimation of trigger efficiency by using the dataset is not appropriate by following reasons. First, the dataset includes huge backgrounds. By filtering the backgrounds the fraction of events by specific trigger changes dramatically. Second, more than one trigger can be fired for an event. Third and Finally, there exist strong correlation between the data purity and trigger efficiency.

Therefore the trigger efficiency will be estimated after the backgrounds reduction is finished: the estimation of the representing trigger efficiency will be explained later in Section 4.2.4.

Chapter 4

Analysis

4.1 Overview

As discussed in Chapter 1 the final goal of this analysis is the measurement of longitudinal spin contribution of \bar{u} and \bar{d} to the whole proton spin $\frac{1}{2}$. The physical observable for the measurement is longitudinal single spin asymmetry (A_L), which originated from W bosons by parity-violating weak interaction between left-handed quarks and right-handed antiquarks inside proton. The actual measurement performed by collecting muons which directly decayed from W bosons. Due to the high mass of its mother the signal muons have high transverse momentum (p_T) of at least a few GeV. The relationship between the A_L and the muons can be expressed as follows:

$$A_L = \frac{1}{\langle P \rangle} \frac{\sigma_+ - \sigma_-}{\sigma_+ + \sigma_-} \quad (4.1)$$

where $\langle P \rangle$ means average beam polarization and σ_{\pm} means longitudinal cross section in positive or negative helicity of the proton beam.

Therefore to achieve the final goal a number of procedures need to be performed. First, one need to extract a well defined set of muon candidates. Second, the set's signal-to-background (S/BG) ratio and uncertainty should be measured. Third and Finally, the A_L and its uncertainties will be measured by using the First and the Second.

This analysis utilizes the PHENIX Muon Arms at forward rapidity ($1.2 < \eta < 2.2$ (S) / 2.4 (N)) to collect the muons from W^{\pm} bosons. Unlike the $W^{\pm} \rightarrow e^{\pm}$ analysis in central rapidity, the Jacobian peak in forward rapidity is strongly suppressed (W^+) or completely smeared out (W^-) (Fig. 4.1). In addition some systematic

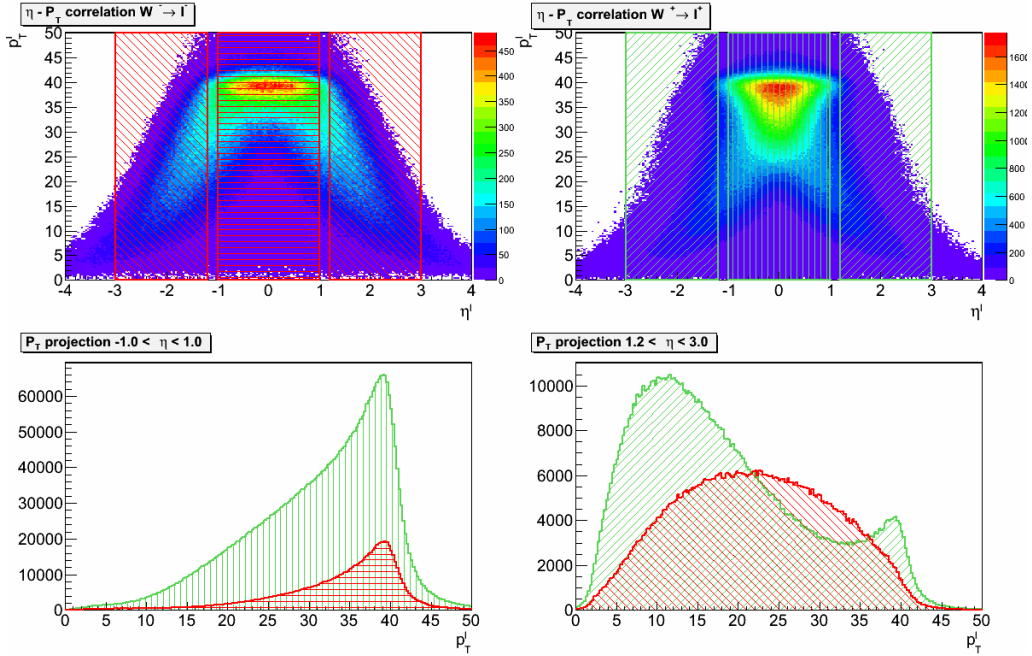


Figure 4.1: p_T vs. η distribution of leptons from W^- (left) and W^+ (right). The bottom left plot shows the projections vs. p_T in $|\eta| < 1.0$ and The bottom right plot shows the projections vs. p_T in $1.2 < \eta < 3.0$. Color of dashed lines indicate charge of the leptons (green for positive, red for negative). This plot is quoted from [11].

conditions of Muon Arms such as limited η acceptance, large amount of signal mimic backgrounds, and low momentum resolution of MuTr makes signal extraction even more difficult. Therefore the separation of the signal muons becomes the major challenge of this analysis.

As explained in section 2.1.2, the combination of the spin direction of each beam (spin pattern) is supposed to be different bunch crossing (i.e. for every collision) by bunch crossing. Therefore to measure the A_L properly each signal candidate must be sorted out by the spin pattern and measured position with respect to a beam's going direction (forward or backward). In addition, to make sure the asymmetry is originated from signal muons a series of crosschecks (zero intrinsic asymmetry, residual transverse polarization via local pol analysis, etc) are also required.

This chapter is composed of two main sections. The first section explains the collection of muon candidates, backgrounds filtering processes, and S/BG estimation of final candidates. The second section explains categorization of final sample, relevant crosschecks, and measurement of final A_L with its errors, respectively.

Note that in the following sections certain type of muon candidate will be expressed in corresponding color, especially for the case of it need to be presented with other types.

- Data (black)
- Signal (red)
- Muonic backgrounds (green)
- Hadronic backgrounds (blue)

4.2 Signal Extraction

4.2.1 Analysis Variables

All analysis variables used in this analysis are summarized in this section. All of the following variables are assigned to each reconstructed single muon candidate. Note that most of the informations are based on following references: [7][8][11]

Physics

- p (GeV/c): momentum at vertex. Physical momentum will be denoted as p^{true} and Reconstructed momentum denoted as p^{reco} for the case of strict distinction is required. Same notation holds in transverse momentum (p_T) as well.
- p_T (GeV/c): transverse momentum component relative to the beam axis.
- η (dimensionless): pseudorapidity at vertex.
- ϕ (rad): azimuthal angle at vertex.

Vertex - MuTr match

- DCA_r (cm): distance of closest approach (DCA) in radial direction between the projected MuTr track and the beam axis. Note that the track is linearly projected from MuTr station 1 with its direction vectors towards collision vertex.
- DCA_z (cm): distance of closest approach in the beam axis direction between the projected MuTr track and the collision vertex. To know the z position of the collision vertex BBC information is required. Its value can be either negative or positive.

FVTX - MuTr match

- $FVTX_{cone}$ (dimensionless): number of FVTX clusters inside a cone around the track under the condition of $0.04 \text{ (rad)} < dR < 0.52 \text{ (rad)}$, where $dR = (d\eta^2 + d\phi^2)^{\frac{1}{2}}$
- $FVTX_{dr}$ (cm): residual difference in radial direction between MuTr track and FVTX track. The matching z position is ~ 160 cm from collision vertex.
- $FVTX_{d\Theta}$ (rad): residual difference in two-dimensional angle between MuTr track and FVTX track. The matching z position is same to $FVTX_{dr}$.
- $FVTX_{d\phi}$ (rad): residual difference in azimuth between MuTr track and FVTX track. The matching z position is same to $FVTX_{dr}$.

MuTr

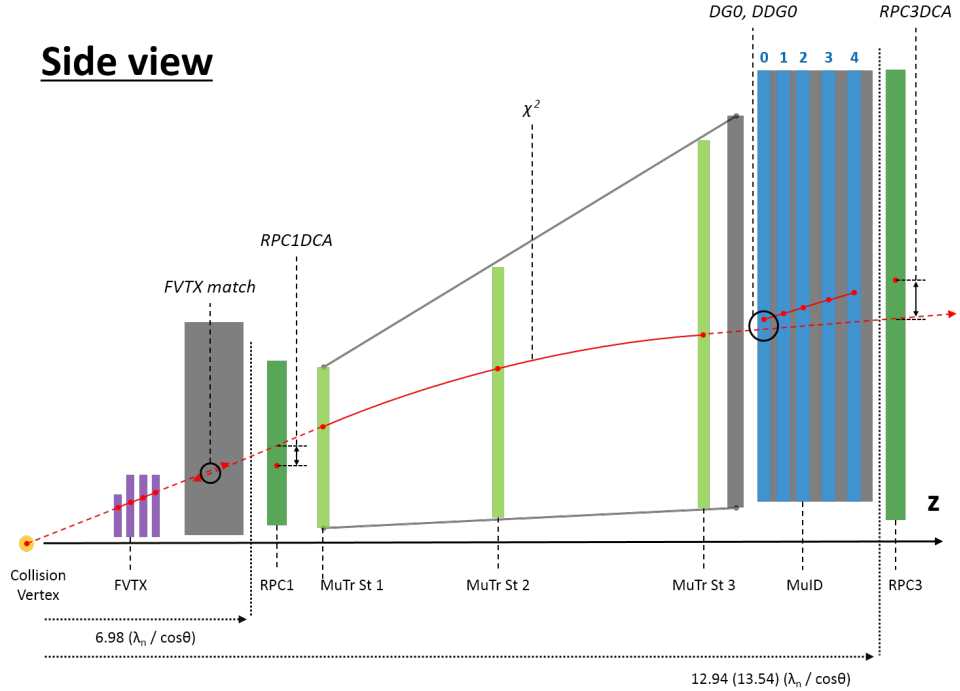
- $d\phi_{ij}$ (rad): azimuthal angle difference between i th station and j th station of MuTr.
- $dw_{ij} (p_T \times \sin\theta \times d\phi_{ij})$ (GeV/c · rad): azimuthal bending between i th station and j th station of MuTr, weighted by p_T and transverse distance from beam axis ($\sin\theta$). Applying p_T compensates strong p_T dependence of the bending while $\sin\theta$ compensates degradation of magnetic field strength in radial direction.
- χ^2 (dimensionless): reduced χ^2 of the reconstructed track which describes quality of the fit to the MuTr coordinates. It is calculated in the Kalman filter by using residuals between the position of MuTr cathode plane and position of the track. The degrees of freedom is 7 (position, momentum, and charge). Note that this χ^2 cannot be directly compared to a statistical χ^2 due to its non-gaussian residual distributions by noise contaminated clusters and misalignment.

MuTr - MuID match

- $DG0$ (cm): distance between the projected MuTr track and the MuID road, at the z position of MuID gap 0.
- $DG4$ (cm): same to $DG0$ except z position is gap 4 of MuID.
- $DDG0$ (degree): slope deviation between the projected MuTr track and the MuID road, at the z position of MuID gap 0.
- $lastGap$ (dimensionless): ID of deepest MuID road among associated roads. By convention it can be 2 to 4 (either 4th and final gap or 5th and final plane of MuID).

MuTr - RPC match

- $RPC1DCA$ (cm): distance of closest approach between the projected MuTr track and the position of the nearest associated cluster in the RPC station 1. Note that the the track is linearly projected from MuTr station 1.
- $RPC3DCA$ (cm): distance of closest approach between the projected track from MuTr station 3 and the nearest associated cluster in the RPC station 3.



Beam view

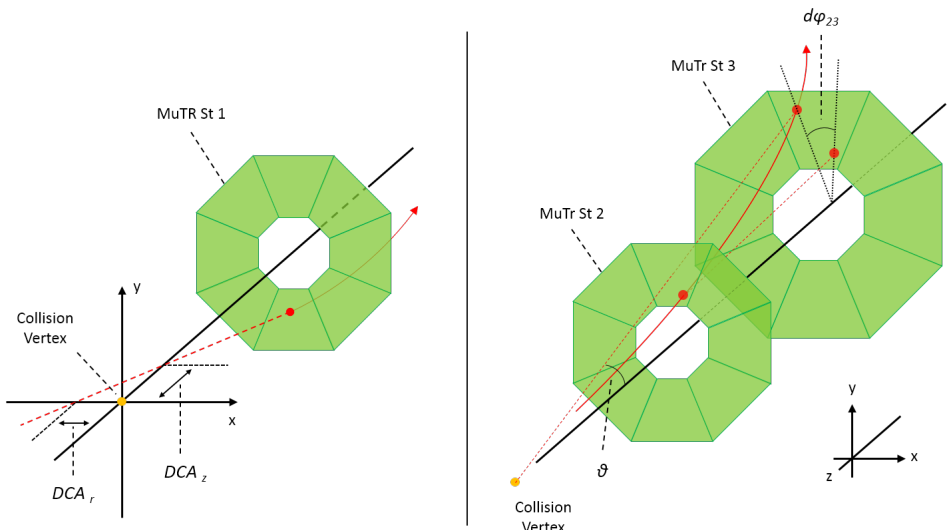


Figure 4.2: Schematic diagrams of analysis variables. The numbers at the bottom of the Top figure indicate accumulated nuclear interaction length of south (north) Muon Arm. Polar angle (θ) in bottom right indicates particular condition for dw_{23} . Note that not all analysis variables are displayed.

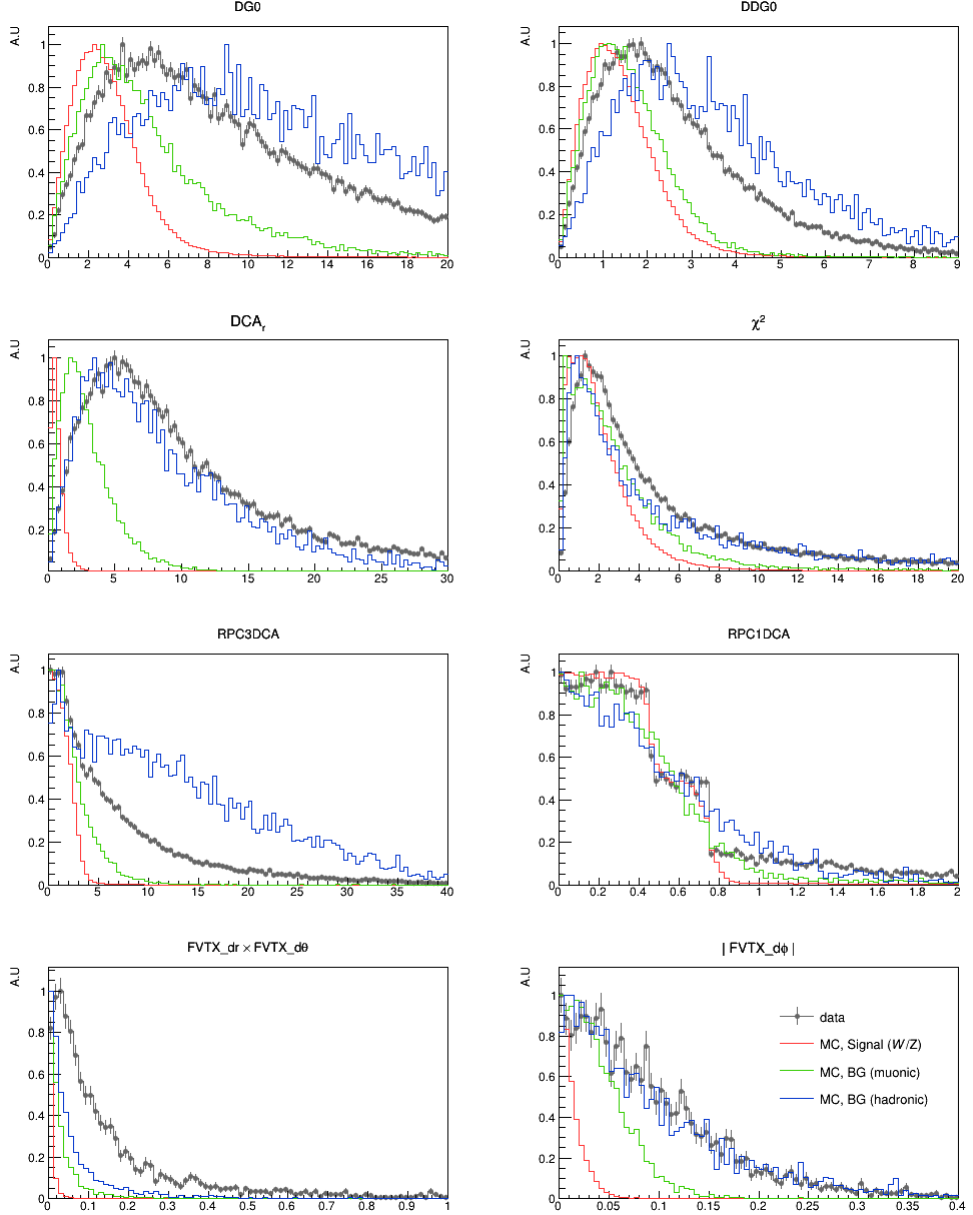


Figure 4.3: Several frequently used kinematic variables' distributions by each type of muon candidate. All MC distributions are a sum of multiple processes. Especially signal and muonic BG distribution is obtained under *high* multiple collision condition. Note that each sample is arbitrary scaled for the comparison. These distributions are obtained from south, negative charged muons.

4.2.2 Type of Muon Candidates

This section explains three types of collected muon candidates as well as the informations of the Monte Carlo (MC) simulations to study their pattern.

Signals: $W/Z \rightarrow \mu$ The signal of this analysis is muons decayed from W^\pm bosons. In general point of view the most direct and clean measurement will be the extraction of distinct W peak. For instance, in the $W^\pm \rightarrow e^\pm$ measurement at Central Arms extraction of Jacobian peak ($p_T \sim \frac{M_W}{2}$) is available thanks to characteristic of W decay kinematics and relative track isolation technique based on EMCal.

However, such direct measurement is not available in Muon Arms by following reasons. First of all, as briefly explained earlier the Jacobian peak is strongly suppressed in forward rapidity by W s' kinematics. Second, due to the limited acceptance of Muon Arms some conventional analysis techniques (ex. track isolation) cannot be employed. Third, large amount of backgrounds are enter MuTr and reconstructed as muons. Fourth, due to the low momentum resolution of MuTr sizable momentum and charge smearing induced in reconstruction process.

Especially the amount of momentum smearing tend to increase as the momentum increase. As a result p_T^{reco} distribution of $W^\pm \rightarrow \mu^\pm$, which is $10 < p_T^{true} < 40$ (GeV/c) in Muon Arms' rapidity range can be smeared up to ~ 100 (GeV/c). However, in this analysis the following p_T^{reco} range is regarded as the p_T^{reco} of valid muon candidate. It is based on the FoM (Figures of Merit) test performed in Run 11 analysis [7][30].

$$16 < p_T^{reco} < 60 \text{ (GeV/c)} \quad (4.2)$$

Despite all of these challenges, several characteristics of muons from W can be utilized to extract them from the raw candidates: First, W bosons decay into single muons. Therefore only one track can be exist for a W event (number of reconstructed track for an event, $FVTX_{cone}$). Second, W bosons decay into muons immediately. Therefore the difference between the reconstructed track at the vertex and the collision vertex will be very close (DCA_r , DCA_z). Third, the angle of multiple scattering θ after the forward absorbers (Central magnet, MuID walls) inversely proportional to p_T . Due to the characteristic of signal muons (high p_T of at least a few GeV) the scattering angle of the signals will be very small compared to the low p_T fakes ($DG0$, $DDG0$, $FVTX_{dr/d\Theta/d\phi}$, $RPC1(3)DCA$). Fourth, the amount of bending (sagitta) of the signals under magnetic field will be small compared to the fakes in the same manner of scattering angle ($d\phi_{ij}$, dw_{ij}). Fifth and Finally, the signal muons are more likely penetrate through all of Muon Arms and reach deepest detector in downstream

(RPC3), while punch-through hadronic backgrounds are more likely to be blocked by hadron absorbers (*lastGap*, *RPC3DCA*).

The relevant information of signal MC will be explained with muonic backgrounds at the end of next paragraph.

Backgrounds: muonic In addition to $W/Z \rightarrow \mu^\pm$ decays, various subprocesses produce muons as well. As Fig. 4.4 shows such muonic backgrounds decrease quickly as p_T increase, and after $p_T > 20$ (GeV/c) muons are dominated by W process with small fraction from Z . But due to the momentum smearing in reconstruction sizable amount of low p_T muons are reconstructed as high p_T muons and remain as irreducible backgrounds.

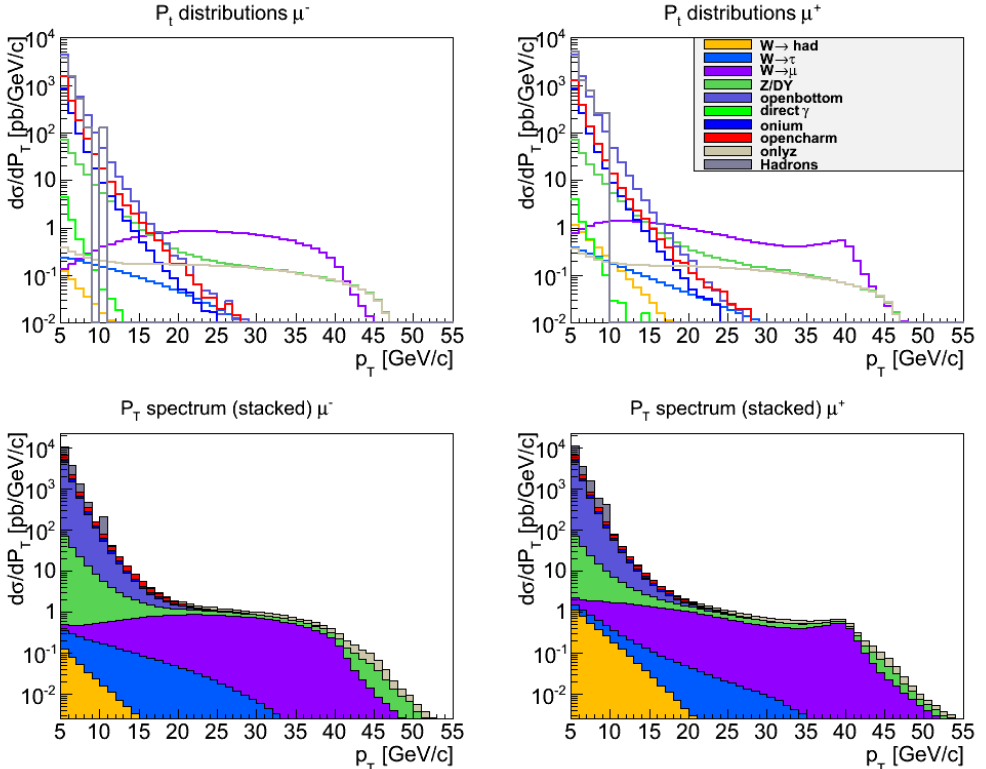


Figure 4.4: Real muon cross sections from Pythia Tune A with k factor of 1.5. All subprocess displayed individually (top) or stacked (bottom), for negative charge (left) or positive charge (right). This plot is quoted from [11].

To quantify these irreducible muonic backgrounds a reliable cross section for each subprocess is required. But since those cross sections are only partially available in the rapidity coverage of the PHENIX Muon Arms, full event simulations are produced from Pythia 6.4[31] by using PHPythia and PISA with Run 12 conditions. The production of each subprocess performed independently to each other. Note that the simulations are produced using Pythia Tune A[32], which is optimized to match the cross sections measured at the Tevatron.

The list of subprocesses are as follows: direct $W \rightarrow \mu$ and $Z \rightarrow \mu$ decays are treated as signal, Direct γ , open bottom, open charm, Quarkonia, $W \rightarrow \text{hadrons}$, $W + \text{jet}$, $W \rightarrow \tau$, Z and Drell Yan, and $Z + \text{jet}$ for muonic backgrounds, respectively. Although $W + \text{jet}$ and $Z + \text{jet}$ are independently produced as well, according to the reference ([31]) those processes are basically included in the W and Z process. Therefore they are not used in this analysis except for cross checking purposes. Also to concentrate on high p_T muons only, events with at least a muon with $p_T > 4$ (GeV/c) and $1.1 < |\eta| < 2.5$ conditions are selectively fed into the PISA simulations.

The production of MC simulations was repeated three times with different reference runs. Since some detectors' (ex. MuTr and MuID) response has clear dependency against collision rate, to reflect it three reference runs chosen by its collision rate. From now on each of these conditions will be denoted as follows:

$$\text{Multiple collision conditions: } \mathbf{high}, \mathbf{mid}, \text{ and } \mathbf{low} \quad (4.3)$$

Table 4.1 shows conditions of each reference runs. Also relevant informations of the produced muonic MC are summarized in Table 4.2.

Although these muonic MC describe the data fairly well, still additional scaling is required to reflect precise yields among final muon candidates. The handling of these final muonic backgrounds and its scaling will be discussed later in section 4.2.5.

Condition	μ	Reference Run	L (nb $^{-1}$)	MuTr factors		
				Arm	Hit efficiency	Charge asym.
<i>high</i>	0.876	367593	42.85	South	0.9475	1.7696
				North	0.8458	2.3917
<i>mid</i>	0.576	367466	56.91	South	0.9513	0.8547
				North	0.9051	1.4297
<i>low</i>	0.409	368630	60.44	South	0.9556	0.6402
				North	0.9281	0.9795

Table 4.1: Reference conditions for MC production. Quoted from [8]. μ is a parameter for the multiple collision condition.

Muonic process	k factor	σ/mb	Generated # (M)	L/pb^{-1}
Direct γ	1.5	5.32×10^{-2}	<i>high</i>	6400.0
			<i>mid</i>	10980.0
			<i>low</i>	11600.0
Open b	1.5	7.30×10^{-3}	<i>high</i>	4003.0
			<i>mid</i>	4590.0
			<i>low</i>	1552.0
Open c	1.5	5.71×10^{-1}	<i>high</i>	134220.0
			<i>mid</i>	286040.0
			<i>low</i>	145940.0
Quarkonia	1.5	1.35×10^{-1}	<i>high</i>	55470.0
			<i>mid</i>	86879.0
			<i>low</i>	32910.0
$W \rightarrow \mu$	1.5	1.66×10^{-6}	<i>high</i>	173.4
			<i>mid</i>	236.7
			<i>low</i>	212.4
$W \rightarrow \text{hadrons}$	1.5	1.66×10^{-6}	<i>high</i>	81.0
			<i>mid</i>	297.0
			<i>low</i>	120.0
$W \rightarrow \tau$	1.5	1.66×10^{-6}	<i>high</i>	82.0
			<i>mid</i>	299.0
			<i>low</i>	118.0
Z/DY (inclusive)	1.5	1.59×10^{-5}	<i>high</i>	245.2
			<i>mid</i>	244.0
			<i>low</i>	101.5
$Z \rightarrow \mu$	1.5	3.37×10^{-7}	<i>high</i>	106.5
			<i>mid</i>	109.0
			<i>low</i>	128.5

Table 4.2: Table of summary for signal MC and muonic backgrounds MC.

Backgrounds: hadronic Although the upstream absorber between the MuTr station 1 and the collision point effectively shield most of incoming hadrons, tiny fraction of relatively low momentum charged hadrons (π^\pm and K^\pm , $p_T < 20$ (GeV/c)) penetrate through the absorber and then enter the MuTr. Even though the fraction is extremely small, by its enormous total cross section compared to muonic processes the overall amount of the introduced hadronic backgrounds becomes very large, eventually.

These hadronic backgrounds are the dominant source of muon candidates in all filtering level.

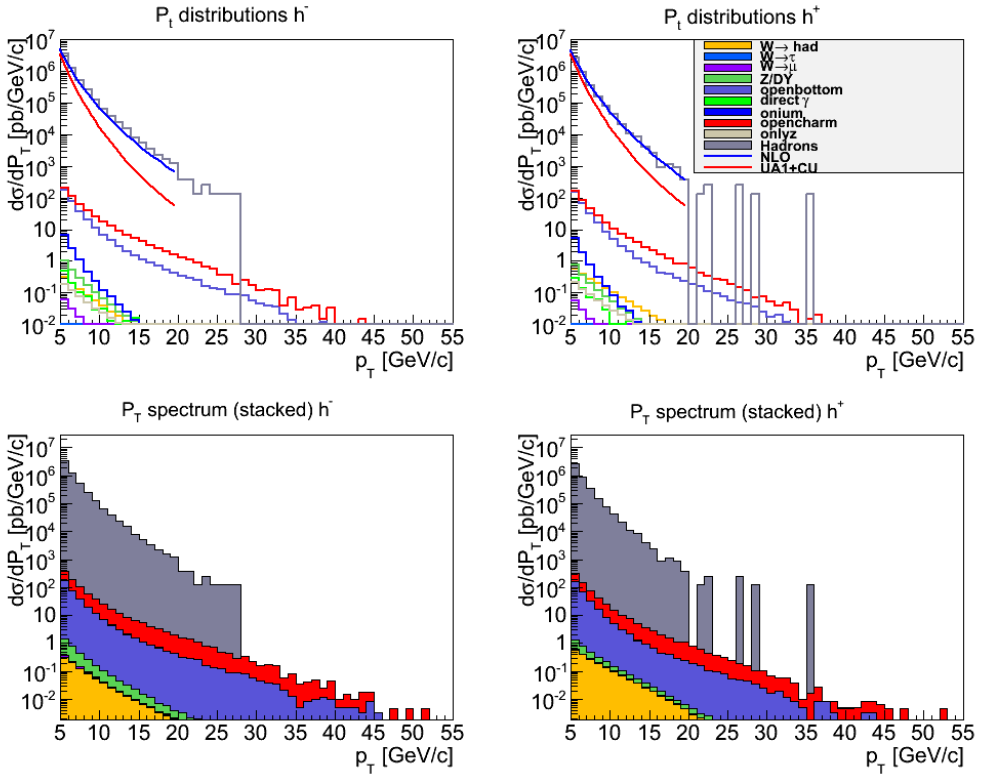


Figure 4.5: Hadron cross sections of π^\pm and K^\pm based on UA1 experiment (red continuous lines) and NLO perturbative QCD calculations (blue continuous lines), displayed individually (top) or stacked (bottom) for negative charge (left) or positive charge (right). Hadrons from muonic subprocesses in Table 4.2 are displayed as well. This plot is quoted from [11].

The overall hadronic backgrounds in $16 < p_T^{reco} < 60$ can be categorized into mainly three types:

- Punch-through: penetrate through both upstream absorber and MuID walls.
- Early muonic decay: decay into muons before reaching to the MuTr.
- Late muonic decay: decay into muons inside MuTr stations.

Note that the first two types of hadronic backgrounds are likely to be reconstructed at their true momenta while the third is not.

Certain distinctive characteristic can be expected for each of these hadronic backgrounds. First, as a punch-through hadron has to penetrate through both upstream absorbers and MuID walls to be reconstructed as a muon, the frequency of the event is rare. Second, if a hadron decayed into muon near collision vertex before it reach upstream absorber it will be reconstructed as valid muon. But as its vertex is not the collision vertex one can expect vertex matching variables (DCA_r, DCA_z) can provide certain degree of distinguishing power. Third and finally, if a hadron penetrated through upstream absorber and then decayed inside MuTr, the reconstruction algorithm trying to fit the trajectory with kink, therefore χ^2 of the reconstructed track is generally larger and the momentum will not be correctly reconstructed [7].

The hadronic backgrounds MC is produced by a random generator creating single hadrons and PISA. Some important characteristics can be summarized as follows.

- Subprocess (most abundant): π^\pm, K^\pm
- p_T bin by p_T bin production in the range of $1 < p_T < 9$ (GeV/c)
- Generated and Applied Gaussian vertex z distribution of 40 cm resemble the data
- Rapidity range of $1.2 < |\eta| < 2.2$ (2.4) for South (North). Later extended to 2.3 (2.5)
- Flat entries vs. η distribution before fed into PISA
- Scaled by production cross sections based on NLO perturbative QCD calculation
- Run 13 condition based production

Note that this hadronic MC produced with respect to Run 13 but both geometrical condition and detector configuration is almost same. The informations of produced hadronic MC is summarized in Table 4.3.

Hadronic process	p_T (GeV/c)	σ /mb	Generated # (M)		L/pb^{-1}
π^-	1 - 2	11.34×10^9	South	59370.0	5.24
			North	59299.0	5.23
	2 - 3	455.99×10^6	South	62902.0	137.95
			North	62601.0	137.29
	3 - 4	50.55×10^6	South	23309.3	461.11
			North	23278.8	460.51
	4 - 5	9.86×10^6	South	4981.2	505.21
			North	5013.0	508.43
	5 - 6	2.66×10^6	South	1401.4	527.40
			North	1390.4	523.26
π^+	6 - 7	891.01×10^3	South	599.2	672.50
			North	592.9	665.43
	7 - 8	346.01×10^3	South	410.1	1185.23
			North	397.8	1149.68
	8 - 9	149.24×10^3	South	341.1	2285.53
			North	329.1	2205.13
	1 - 2	11.40×10^9	South	60206.0	5.28
			North	60227.0	5.28
	2 - 3	462.40×10^6	South	63405.0	137.12
K^-			North	63126.0	136.52
	3 - 4	51.97×10^6	South	23411.8	450.50
			North	23375.2	449.80
	4 - 5	10.33×10^6	South	5228.2	506.35
			North	5281.4	511.49
	5 - 6	2.84×10^6	South	1499.1	527.46
			North	1488.4	523.69
	6 - 7	975.48×10^3	South	602.1	617.23
			North	601.9	617.03
K^+	7 - 8	388.49×10^3	South	402.7	1036.57
			North	408.3	1050.98
	8 - 9	171.98×10^3	South	346.4	2014.19
			North	327.3	1903.13
	1 - 2	1.33×10^9	South	59141.0	44.32
			North	58589.0	43.90
	2 - 3	112.20×10^6	South	56308.0	501.86
			North	56292.0	501.72
	3 - 4	14.14×10^6	South	7642.9	540.69
			North	7664.9	542.24
K^+	4 - 5	2.89×10^6	South	1694.5	585.67
			North	1690.9	584.43
	5 - 6	794.52×10^3	South	673.9	848.19
			North	672.4	846.30
	6 - 7	267.77×10^3	South	422.5	1577.87
			North	417.2	1558.08
	7 - 8	103.61×10^3	South	350.0	3377.96
			North	335.9	3241.87
	8 - 9	44.33×10^3	South	346.7	7820.91
			North	334.3	7541.19
	1 - 2	1.43×10^9	South	59644.0	41.72
			North	58882.0	41.18
	2 - 3	119.28×10^6	South	60042.0	503.36
			North	59986.0	502.89
	3 - 4	15.61×10^6	South	7902.2	506.09
			North	7898.6	505.86
	4 - 5	3.35×10^6	South	1697.2	507.25
			North	1685.8	503.85
	5 - 6	968.16×10^3	South	672.9	695.03
			North	668.2	690.17
	6 - 7	344.40×10^3	South	427.0	1239.85
			North	420.1	1219.82
	7 - 8	141.04×10^3	South	346.1	2453.85
			North	341.6	2421.94
	8 - 9	63.87×10^3	South	344.3	5390.90
			North	323.7	5068.36

Reference run: 393888 (2013 data taking period)

Table 4.3: Table of summary for hadron MC

According to the results of Run 11 hadronic MC analysis[7], the yields of high p_T^{reco} hadronic backgrounds are dominated by $p_T^{true} < 3$ (GeV/c) events. As for the subprocess among those events K^+ dominates with a relative fraction of 60 % to 70 % while K^- takes fraction of 20 % to 30 %. The contribution from π^\pm is ~ 10 %. It is a reflection of the longer lifetime of π^\pm than K^\pm and the steep fall-off of the hadronic cross section in addition to its probability of absorber penetration.

Like muonic MC case, despite plenty of hints these hadronic MC give it cannot be directly utilized to extract signals from final muon candidates. The handling of hadronic backgrounds among final sample will be explained later, in section 4.2.5.

Reliability of the MC To use the MC for the backgrounds reduction in the p_T range of interest ($16 < p_T < 60$ (GeV/c)), their match to the data need to be tested for each of analysis variables. Among the MC, the reliability of muonic MC has been intensively tested [12][30] by using match to the cosmic muons. As a result it confirmed that the muonc MC describes cosmic muon data well. In succession to the study, overall MC including hadrons need to be tested if it can reproduce distribution of the data.

Following Fig. 4.6 and Fig. 4.7 show match between the stack of all MC and the data. Note that those distributions include lower p_T range than the p_T region of interest (Eq. 4.2). Although not all of distributions displayed in the figure, all of distributions in other condition shows reasonable match. Therefore these MC judged as reliable thus will be actively used in following analysis procedures.

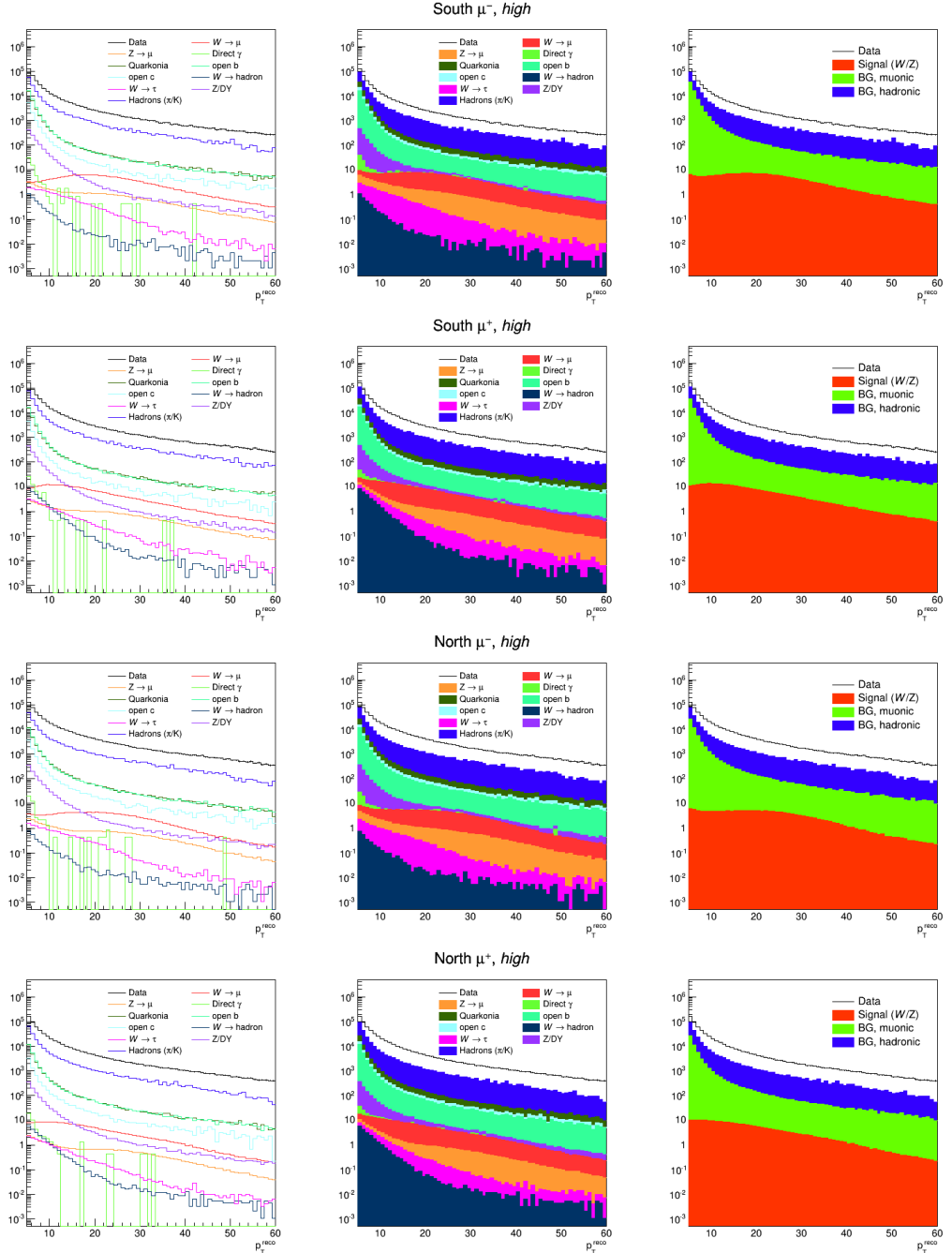


Figure 4.6: Stacked cross sections including both muonic and hadronic processes, after 1st backgrounds filtering by *Basic cut* in section 4.2.3. Each subprocess scaled to the luminosity of the data. Note that $Z \rightarrow \mu$ process subtracted from Z/DY to prevent double counting.

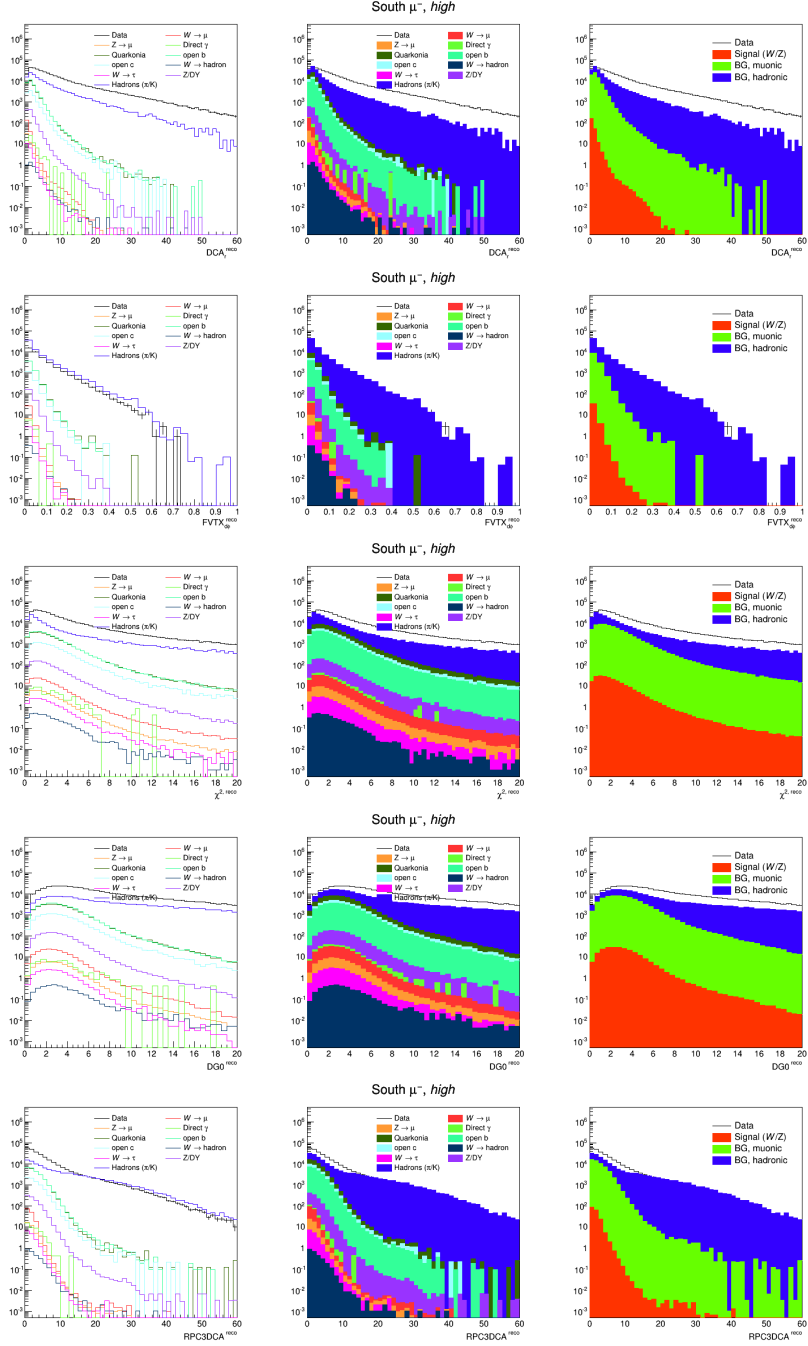


Figure 4.7: Stacked cross sections with same condition to previous Fig. 4.6 including p_T range. Some kinematic variables from south, negative muons are selectively displayed but the other conditions (side, charge or variable) also show reasonable match as well.

4.2.3 Backgrounds Filtering

This section explains four stages of backgrounds reduction process. The muon candidates after 4th and final filtering will be called *Tight candidates* and will be used in the estimation of A_L .

1st filtering: *Basic cut* First stage of backgrounds filtering is done by applying a set of kinematic variables filter called as *Basic cut*. Following list shows involved kinematic variables with cut values.

- Events with single reconstructed track in MuTr
- $\chi^2 < 20$
- $DG0 < 20$ (cm)
- $DDG0 < 9$ (degree)
- $lastGap = 4$
- $p < 250$ (GeV/c)
- $16 < p_T < 60$ (GeV/c)

This is a minimum selection criteria for the identification of all muon-like tracks at $p_T^{reco} = 10$ (GeV/c). In detail, to search optimal cut of each kinematic variable several percentile contours (99.5, 97, 95, and 90 (%)) were defined and tested by evaluating single muon yields within it [30][7]. As the cut values in the *Basic cut* are looser than the one of 99.5 % contour, in principle, almost all of muon-like tracks will be accepted even after filtered by these cuts unless the distribution seriously depends on its p_T .

The kinematic distributions are generally wider at lower p_T and tend to narrow down with increasing p_T , except small exception at highest p_T where smearing is biggest concern. However, even if the dependency is considered in, the dependence to the p_T does not significantly affect overall distributions. As major portion of backgrounds originated from low p_T particles $p_T^{reco} = 10$ is set as the standard.

2nd filtering: define $Wness$ Although reasonable match between the inclusive MC and the data is verified in section 4.2.2, still it is not sufficient to extract signals directly from the muon candidates due to backgrounds dominance. On the other hand, as Fig. 4.3 suggests there exist certain degree of discrepancy between signal distributions and background distributions. Therefore abundant backgrounds itself can be utilized by definining a likelihood to specific type of muon candidates. Hereafter the likelihood especially to W signals will be denoted as $Wness$.

To define $Wness$ both kinematic variables and samples (for signals or backgrounds) need to be specified. The definition and assignment of $Wness$ is based on probability density functions. From now on greek letter λ or acronym PDF indicates a probability density function composed of a kinematic variable's histogram. The library RooFit[33] is used in the composition of PDFs. Note that all of following procedures are based on muon candidates filtered by *Basic cut*.

First, following 9 kinematic variables are used to define λ_{sig} or λ_{BG} :

- $DG0$, $DDG0$, DCA_r , χ^2 , $RPC3DCA$, $RPC1DCA$, $FVTX_{dr} \times FVTX_{d\Theta}$, and $|FVTX_{d\phi}|$

Then λ_{sig} or λ_{BG} can be defined as follows:

$$\lambda_{\text{sig(BG)}} = (\lambda_{DG0} \cdot \lambda_{DDG0}) \cdot (\lambda_{DCA_r} \cdot \lambda_{\chi^2}) \cdot \lambda_{\dots} \quad (4.4)$$

In all cases at least one associated hit in either RPC1 or RPC3 is required in addition to first four variables. But latter variables including $RPC1(3)DCA$ are used when available due to external reason such as efficiency. Especially fraction of events with meaningful FVTX match variables are $\sim 7\%$ after *Basic cut*. Therefore to assign proper $Wness$ with respect to its condition multiple set of PDFs are prepared at the same time and then selectively used for the corresponding condition of an event. Following list shows conditions of PDFs used in the determinaton of the $Wness$. In short, total $2 \times 2 \times 3 \times 2$ number of different conditions exist in the determination of the Wness.

- Arm (south or north)
- Charge sign (negative or positive)
- $RPCDCA$ condition: both stations or only 1 station (RPC1 or RPC3) has associated hit
- $FVTX$ *Match* variables have valid value or not

Second, following samples are used to obtain a λ_{sig} or a λ_{BG} : note that the PDFs for signals and backgrounds are divided into three groups by its multiple collision condition.

1. *high*:

- Signals: Pythia + PISA MC for *high* condition $W \rightarrow \mu$
- Backgrounds: *high* condition data

2. *mid*: ...

3. *low*: ...

To reflect corresponding multiple collision condition above 3 sets of PDFs are prepared at the same time and selectively used similar to the kinematic variables.

Like distributions for signal, distributions for backgrounds can be obtained from muonic and hadronic MC as well. However, though hadronic MC takes dominant fraction even among the backgrounds, as precise fraction of each backgrounds is unknown direct use of backgrounds MC would be inappropriate. On the other hand, as more than 99 % fraction of data is dominated by backgrounds, data itself can be a good sample of total backgrounds without worrying their fraction. But one important caveat exist in using data as backgrounds sample. Although the fraction is very small there exist signals in the data. Therefore the signal contamination in the backgrounds will induce certain degree of smearing in the determination of W_{ness} .

Eventually, once all preparation is finished W_{ness} is defined as follows.

$$W_{\text{ness}} = \frac{\lambda_{\text{sig}}}{\lambda_{\text{sig}} + \lambda_{\text{BG}}} \quad (4.5)$$

Note that additional cuts are applied during the composition of the PDFs: in any case $DCA_r < 30$ (cm) and either one or both of $RPCDCA$ ($RPC1DCA < 20$ (cm), $RPC3DCA < 40$ (cm)) have to be satisfied. In succession to this, not all of muon candidates after *Basic cut* are assigned with valid W_{ness} ($0 \leq W_{\text{ness}} \leq 1$). Thus assigning W_{ness} itself works as a cut: as a result ~ 30 % of *Basic cut* passed muons are excluded. Especially the events which proper W_{ness} cannot be assigned ($\lambda_{\text{sig}} + \lambda_{\text{BG}} = 0$) suggest they judged as neither a signal nor a known form of background.

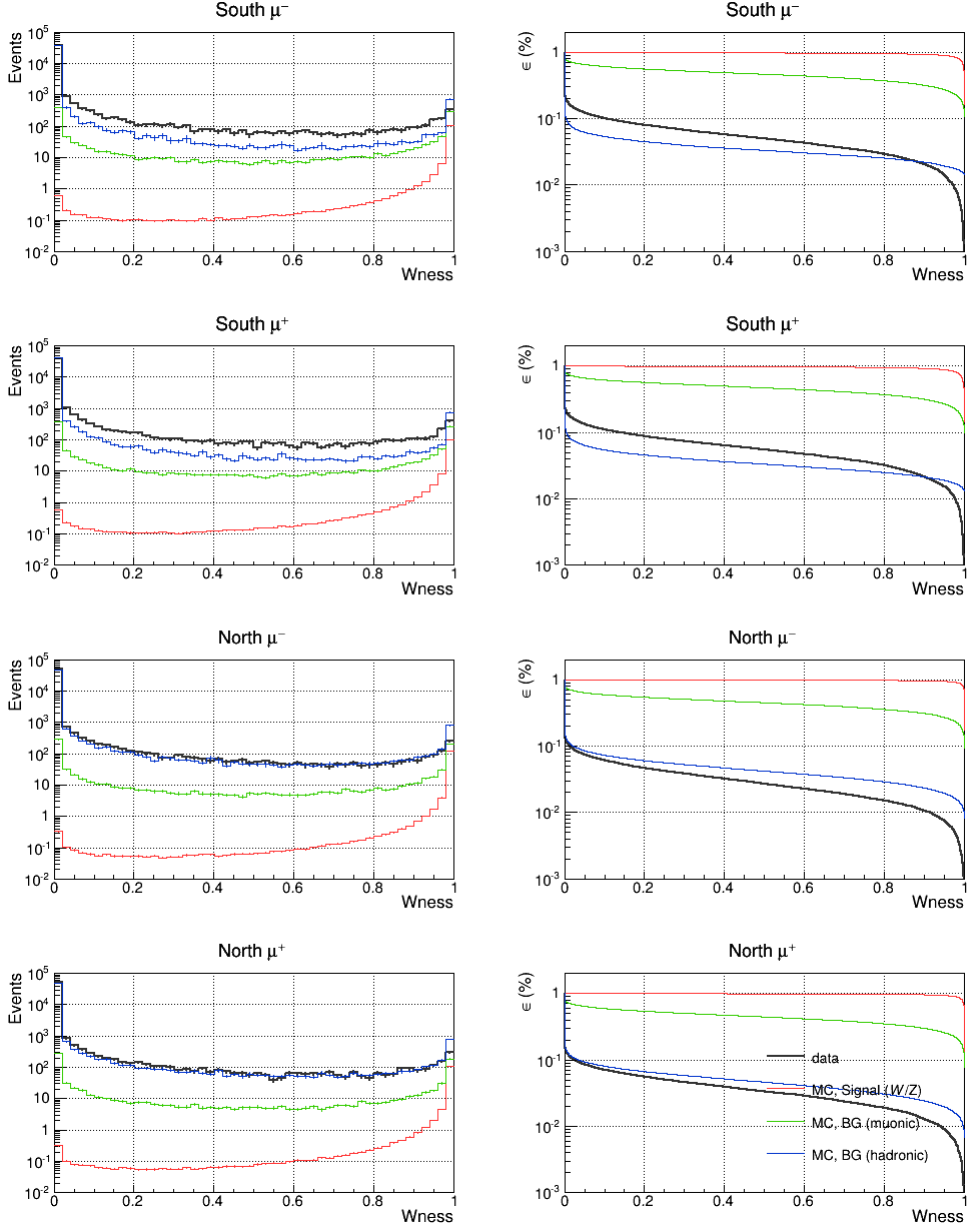


Figure 4.8: Distributions (left) and Efficiencies (right) of W_{ness} for all three types of muon candidates. Note that MC distributions for certain type of muon candidates are a stack of multiple subprocess after luminosity scaling. Especially for muonic backgrounds additional scaling factors in later section 4.2.5 are applied as well. All multiple collision conditions are considered by using the fractions in Table 4.4.

3rd filtering: optimal W_{ness} cut W_{ness} is a measure of how much an event is closer to the W signal. By its definition the purity of the candidates is higher as tighter W_{ness} cut (closer to 1) is applied. However by applying W_{ness} cut not only backgrounds but also certain portion of signals will be excluded as well. Thus a figure of merit (FoM) need to be tested to search optimal W_{ness} cut which keep most of signals but exclude as many as backgrounds.

As a first step, fraction of events with each multiple collision condition is estimated. As the Table 4.4 shows the fraction of each condition is stable with W_{ness} change. If all signal distributions (W MC) have same dependence to W_{ness} there's no need to worry about these fractions. But as Fig. 4.10 shows a little discrepancy exists among each distribution.

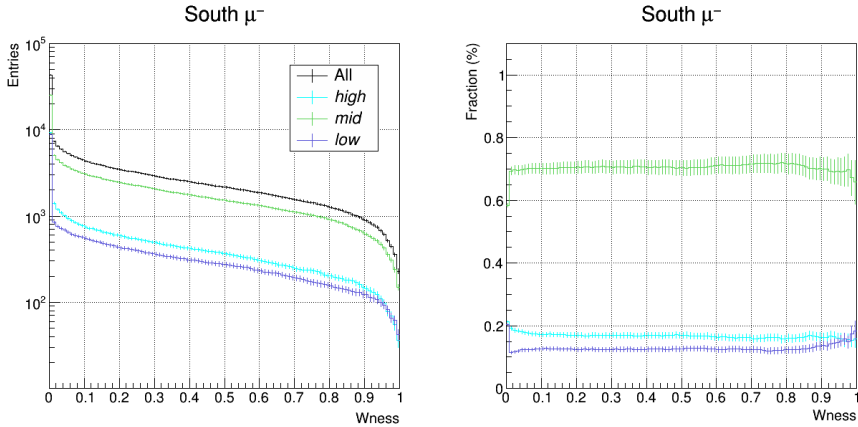


Figure 4.9: Fraction of each multiple collision condition in the data after *2nd filtering*. Left plot shows number of events and Right plot shows their fraction to the whole.

Arm and Charge	Wness	high	mid	low
South μ^-	0 - 1	0.167 ± 0.010	0.705 ± 0.026	0.128 ± 0.009
	0.9 - 1	0.159 ± 0.018	0.688 ± 0.046	0.152 ± 0.018
South μ^+	0 - 1	0.171 ± 0.010	0.691 ± 0.024	0.138 ± 0.009
	0.9 - 1	0.165 ± 0.018	0.685 ± 0.043	0.150 ± 0.017
North μ^-	0 - 1	0.272 ± 0.016	0.517 ± 0.025	0.211 ± 0.014
	0.9 - 1	0.246 ± 0.028	0.562 ± 0.048	0.192 ± 0.024
North μ^+	0 - 1	0.240 ± 0.013	0.532 ± 0.022	0.564 ± 0.043
	0.9 - 1	0.172 ± 0.021	0.564 ± 0.043	0.264 ± 0.027

Table 4.4: Fraction of events with each multiple collision condition after *2nd filtering*. The first bin around $W_{ness} \sim 0.01$ is omitted in the fraction calculation.

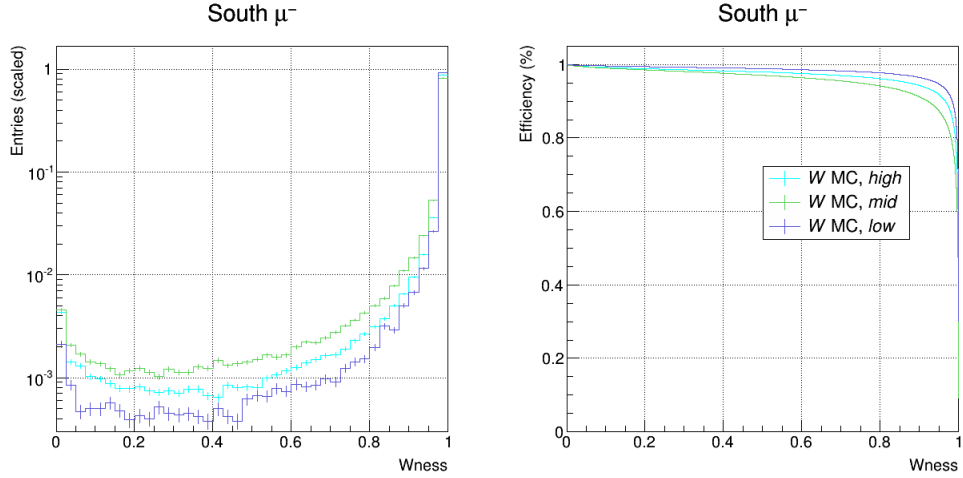


Figure 4.10: Normalized yields of W MC with different multiple collision condition (left) and Its efficiency versus $Wness$ (right).

Next, the FoM of the $Wness$ can be judged by *Significance* test with signal MC and background MC.

$$Significance = \frac{Signal}{\sqrt{Signal + Background}} \quad (4.6)$$

To test *Significance*, all relevant subprocesses for certain type of candidates (ex. muonic BG) are stacked, scaled, and then normalized by its own integral. Especially for muonic backgrounds additional scaling factors in later section 4.2.5 are applied as well.

Since two types of backgrounds exist and their fraction among data is unknown, *Significance* tested independently to each type of backgrounds in addition to multiple collision condition. Fig. 4.11 shows an example of south negative charged muons.

Once all ingredient is prepared optimal $Wness$ cut can be calculated as follows. The results are summarized in Table 4.5.

$$Wness_{opt} = \sum_{i=1}^3 fraction_i \times Wness_i \text{ (at max. Significance)} \quad (4.7)$$

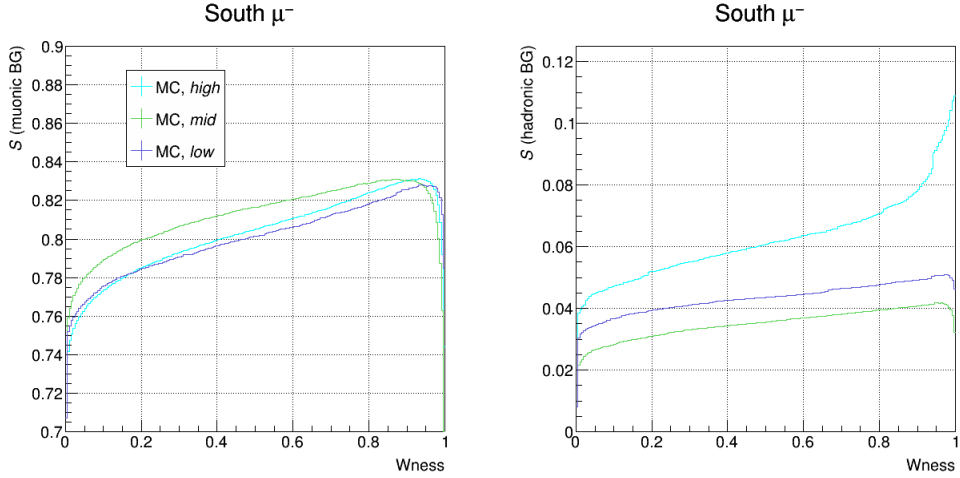


Figure 4.11: Example of *Significance* test by using signal MC and backgrounds MC for each multiple collision condition. Left plot shows results versus muonic backgrounds and Right plot shows results versus hadronic backgrounds.

Background type	Arm and Charge	Wness at max. Significance			Wness _{opt}
		high	mid	low	
Muonic	South μ^-	0.9334	0.8684	0.9384	0.8882
	South μ^+	0.9334	0.8584	0.9585	0.8850
	North μ^-	0.9585	0.9484	0.9484	0.9511
	North μ^+	0.9484	0.8984	0.9434	0.9207
Hadronic	South μ^-	0.9985	0.9484	0.9735	0.9600
	South μ^+	0.9935	0.9535	0.9635	0.9617
	North μ^-	0.9985	0.9935	0.9835	0.9928
	North μ^+	0.9985	0.9985	0.9785	0.9939

Table 4.5: Summary of *Significance* test with various conditions. The average values in the last column are calculated by weighting the fraction of each multiple collision condition in Table 4.4, especially with the fraction at $0 \leq Wness \leq 1$.

Judging from the $Wness_{opt}$ (fraction weighted average) in Table 4.5, hadronic backgrounds require tighter $Wness$ cut than muonic backgrounds as well as north side require tighter cut than south. However, as continually mentioned fraction of each type of backgrounds among data is unknown. Also it can be possible the fraction even varies versus $Wness$. At least one conclusion can be draw: as hadronic backgrounds' fraction higher optimal $Wness$ cut becomes tighter. And it is a verified knowledge that hadronic backgrounds is at least factor of two abundant than muonic backgrounds in all $Wness$ region.

In conclusion, it is hard to set one optimal $Wness$ cut satisfying all conditions. Therefore to minimize final uncertainty of the A_L another FoM should be tested with various $Wness$. However, a minimum limit of meaningful $Wness$ cut can be set by the results of *Significance* test:

$$Wness > \mathbf{0.92} \quad (4.8)$$

4th and Final filtering: define H_{ness} Though W_{ness} shows fine performance in overall discrimination between signals and backgrounds, still backgrounds are dominant even after $W_{ness} > 0.92$. Main reason is of course the abundance of signal mimic backgrounds itself, however, it also caused by intrinsic uncertainty of W_{ness} .

There are a couple of reasons for this intrinsic uncertainty. First, the W_{ness} is defined by the PDFs composed of several kinematic variables' distribution. However as Fig. 4.3 shows there exist certain amount of overlap between signals and backgrounds in all variables. These overlap eventually induces ambiguity in the determination of W_{ness} . Second, data itself is used as the sample of backgrounds in defining W_{ness} . As discussed previously data includes small fraction of signal thus it can cause another smearing.

Therefore further backgrounds rejection is required in addition to the W_{ness} : especially as hadronic backgrounds are dominant in all region of interest it need to be suppressed as much as possible. For this purpose another likelihood is defined as follows:

$$H_{ness} = \frac{\lambda_{\text{BG, hadronic}}}{\lambda_{\text{sig}} + \lambda_{\text{BG, hadronic}}} \quad (4.9)$$

As the definition indicates this likelihood judges how much a candidate close to the hadronic backgrounds. Note that H_{ness} has no distinguishing power against muonic backgrounds. The kinematic variables and assigning conditions for the H_{ness} is exactly same to W_{ness} , however, hadronic MC and signal MC is used as the sample for ‘signal’ and ‘background’ in this case.

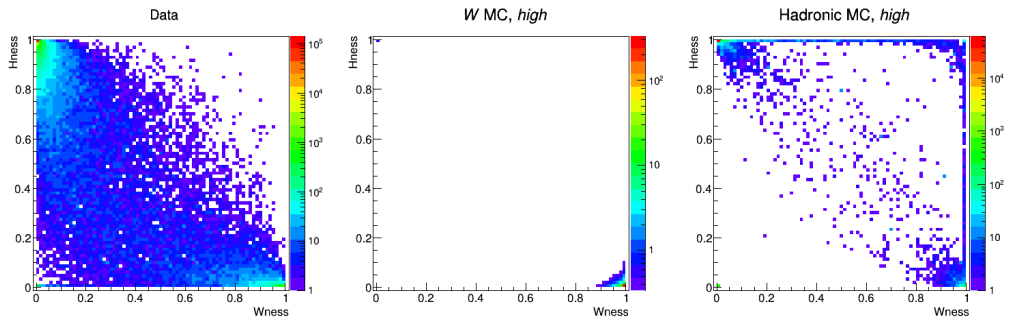


Figure 4.12: H_{ness} vs. W_{ness} for data (left), signal MC (middle), and hadronic MC (right). Each MC is scaled by luminosity. Hadronic MC is a sum of all subprocesses and p_T bins.

By definition H_{ness} should be inversely proportional to W_{ness} : an event with high W_{ness} should have low H_{ness} and vice versa. However this negative correlation is diluted in the data due to the smearing in W_{ness} and the presence of muonic backgrounds. The correlation between two likelihoods can be seen in Fig. 4.12.

H_{ness} targets relatively hadron-like events in $W_{ness} > 0.92$ condition. Once optimal H_{ness} cut value is defined it can be used either to select signal-like events ($H_{ness_{event}} < H_{ness_{opt}}$) or to exclude hadron-like events ($H_{ness_{event}} > H_{ness_{opt}}$). For this purpose a FoM test is performed by using signal MC's efficiency versus increasing H_{ness} .

Fig. 4.13 shows an example of the FoM test: as it shows signal efficiency rapidly falls off with H_{ness} . To exclude as many as hadron-like events but to keep most of the signals, the H_{ness} at 5 % signal efficiency is determined as the optimal cut value. In other words with this H_{ness} cut 95 % of signals being conserved but 5 % of the them can be lost. Note that the 5 % standard is set arbitrary: therefore to check its validity the H_{ness} obtained by this standard is tested with one of the fit variables (dw_{23}) in 4.2.5. As the cut describes a characteristic of hadronic backgrounds (sidebands) fairly well it is regarded the standard set properly.

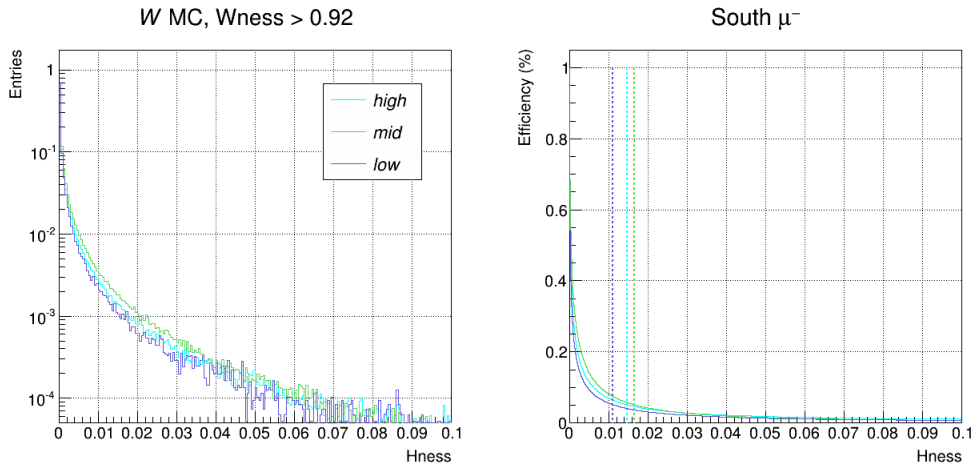


Figure 4.13: Finding optimal H_{ness} cut by using signal MC. Left column shows signal MC distributions vs. H_{ness} with $W_{ness} > 0.92$ condition and Right column shows its efficiency vs. H_{ness} . Dashed lines in right column indicate H_{ness} for 5 % signal efficiency.

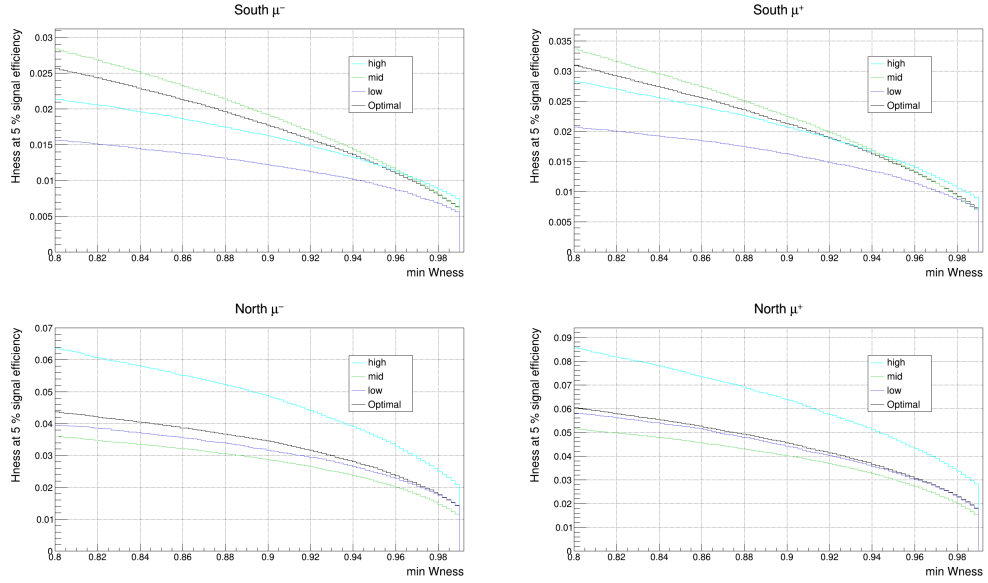


Figure 4.14: Optimal H_{ness} vs. W_{ness} for each Arm and Charge. Each colored lines indicate optimal H_{ness} for each multiple collision condition and A black line indicates multiple collision fraction weighted final optimal H_{ness} .

The FoM test is repeated multiple times by W_{ness} and three multiple collision conditions. With increasing W_{ness} hadron-like candidates likely decrease, thus optimal cut value of the H_{ness} will be affected as well. Also as discussed before each multiple collision should be dealt with separately: therefore 1st optimal H_{ness} cut values are obtained separately, then 2nd and final H_{ness} is defined by weighting fraction of multiple collision condition (Table 4.4) onto 1st optimal H_{ness} . Fig. 4.14 shows the results of repeated FoM test and Table 4.6 shows optimal H_{ness} for several W_{ness} points.

$H_{ness_{opt}}$ (multiple collision fraction weighted)				
W_{ness}	South μ^-	South μ^+	North μ^-	North μ^+
0.90	0.017564	0.021158	0.034300	0.045165
0.92	0.015530	0.018732	0.031267	0.040963
0.99	0.005433	0.006374	0.012126	0.015529

Table 4.6: Optimal H_{ness} for several W_{ness} conditions.

Hereafter the muon candidates satisfying $W_{ness} > 0.92$ and optimal H_{ness} at corresponding W_{ness} will be denoted as *Tight candidates*. The remaining yields of the muon candidates after each filtering condition is summarized in Table 4.7.

Filtering condition		South μ^-	South μ^+	North μ^-	North μ^+	Total
1st	<i>Basic cut</i>	57,562	61,852	88,957	93,411	301,782
2nd	$+ 0 \leq W_{ness} \leq 1$	43,320	46,385	57,286	60,099	207,090
3rd	$+ W_{ness} > 0.92$	786	871	547	680	2,884
4th	$+ H_{ness_{event}} < H_{ness_{opt}}$	673	776	377	519	2,345

Table 4.7: Yields of single muon candidates after each filtering condition. Note that the applied $H_{ness_{opt}}$ at 4th filter is the optimal value for $W_{ness} = 0.92$.

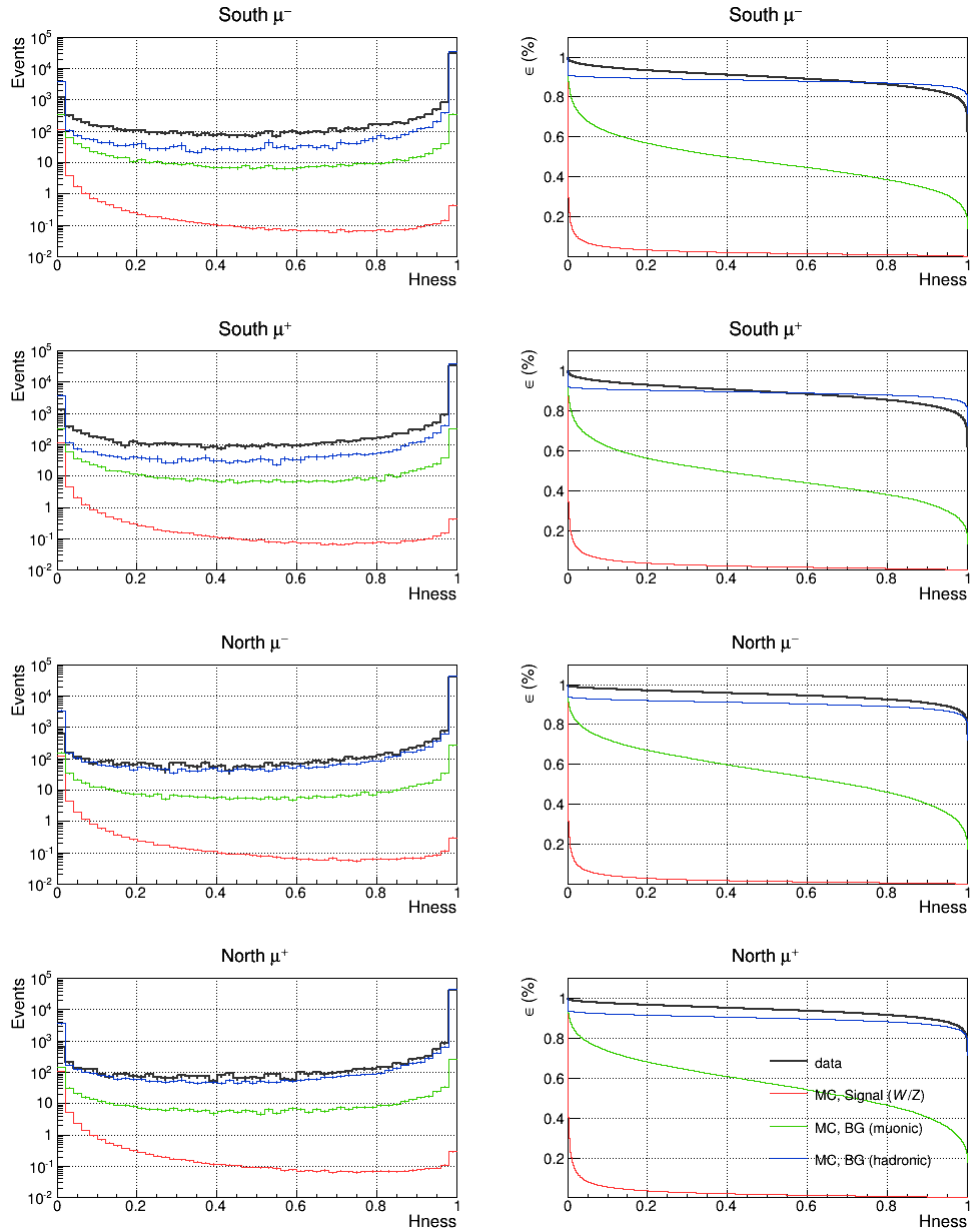


Figure 4.15: Distributions (left) and Efficiencies (right) of H_{ness} for all three types of muon candidates. The other conditions are same to Fig. 4.8.

4.2.4 Overall trigger efficiency

In principle by applying tighter filtering conditions overall purity of the muon candidates will be higher. As the muon triggers designed for the real muons, once can expect a correlation between the filtering conditions and the trigger efficiency. It is a confirmed knowledge that there is a clear linear correlation between W_{ness} and muon triggers' efficiency. Since the *Tight candidates* are a small fraction of the data with very high W_{ness} , its trigger efficiency need to be estimated with the same filtering condition. The list of triggers related to this study is summarized in table 4.8.

Name ¹	Bit mask	Abbr. ²	Type	Order ²
ERT_4x4b	0x40	ERT	ERT	6
ERT_4x4a&BBC	0x80			7
ERT_4x4c&BBC	0x100			8
ERTLL1_E	0x200			9
ERTLL1_E&BBC	0x400			10
MPC_B	0x1000	MPC	MPC	12
MPC_A	0x2000			13
MPC_C&ERT_2x2	0x4000			14
(MPCS_C&MPCS_C) (MPCN_C & MPCN_C)	0x8000			15
MUID2D&BBCnoVtx	0x10000	MUID2D	Muon	16
MUID1D&BBCnoVtx	0x20000	MUID1D		17
SG1&MUID1D&BBCnoVtx	0x40000	R12W1		18
SG3&MUID1D&BBCnoVtx_S	0x80000	19		
SG3&MUID1D&BBCnoVtx_N	0x100000	20		
SG3&MU1D1H&BBCnoVtx	0x200000	21		
SG3&BBCnoVtx_S	0x400000	22		
SG3&BBCnoVtx_N	0x800000	23		
SG1&BBCnoVtx_S	0x1000000	24		
SG1&BBCnoVtx_N	0x2000000	25		
SG1&RPC3_&BBCnoVtx_S	0x4000000	R12W2_S		26
SG1&RPC3_&BBCnoVtx_N	0x8000000	R12W2_N		27

¹ Arbitrary simplified

² Unofficial convention (only used in this thesis)

Table 4.8: Simplified list of triggers for Run12 p + p at 510 GeV (Full list in Table 2.10). Triggers tagged as Muon are the triggers for the muon candidates. Especially triggers with abbreviation R12W are main W triggers for the Run12.

As Table 4.8 shows total 12 muon triggers exist. Although two specific $W \rightarrow \mu$ triggers (R12W1 and R12W2) are expected to take the biggest portion of the W candidates, the other triggers also need to be considered as well to obtain a single efficiency value which represent all relevant conditions. Let this one representing efficiency as ‘Overall trigger efficiency’ ($\epsilon_{trig\ OA}$) hereafter.

To get the $\epsilon_{trig\ OA}$ following issues need to be resolved first. Note that the remaining parts of the paragraph will be continued as the order of the list.

1. Fraction of each muon trigger among *Tight candidates*

- Number of simultaneously fired triggers for an event
- ID of a trigger (or combination of triggers for more than one trigger fired)
- Acceptance of each trigger (or trigger combination)

2. Average efficiency of each muon trigger (or trigger combination) at $W_{ness} > 0.92$

- Muon candidates independent from muon triggers
- Statistics of independent muon candidates

First of all, there could be the case which more than one trigger fired simultaneously for a muon candidate. Fig. 4.16 shows the number of simultaneously fired triggers for a muon candidate in the *Tight candidates* condition. As it shows at least 40 % of the muons experienced more than two triggers fired simultaneously. Note that even if the number of fired triggers are same its combination can be different (ex. MUID1D and R12W1 vs. MUID1D and R12W2).

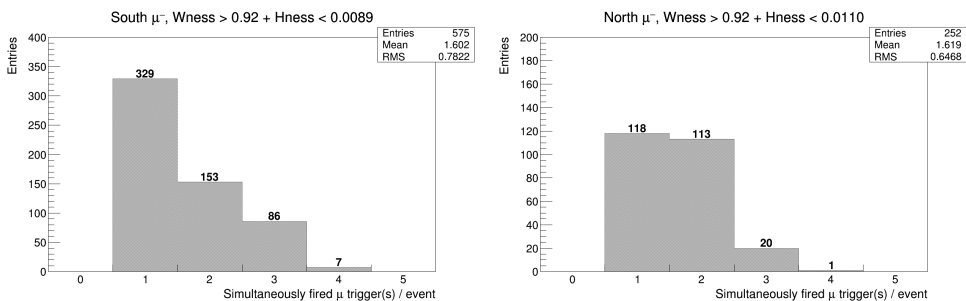


Figure 4.16: Number of triggers simultaneously fired for an event, for south (left) and north (right). The pattern is similar to the positive charged muon candidates as well.

1 trigger fired		2 triggers fired		3 triggers fired		4 triggers fired	
Comb	Trigger	Comb	Triggers	Comb	Triggers	Comb	Triggers
0	<i>16</i>	9	<i>16, 18</i>	26	<i>16, 17, 27</i>	42	<i>16, 17, 18, 20</i>
1	<i>17</i>	10	<i>16, 20</i>	27	<i>16, 18, 19</i>	43	<i>16, 17, 18, 26</i>
2	<i>18</i>	11	<i>16, 26</i>	28	<i>16, 18, 20</i>	44	<i>16, 17, 18, 27</i>
3	<i>19</i>	12	<i>16, 27</i>	29	<i>16, 18, 26</i>	45	<i>16, 18, 19, 26</i>
4	<i>20</i>	13	<i>17, 18</i>	30	<i>16, 18, 27</i>	46	<i>16, 18, 20, 27</i>
5	<i>21</i>	14	<i>17, 20</i>	31	<i>16, 19, 20</i>	47	<i>17, 18, 19, 26</i>
6	<i>22</i>	15	<i>17, 26</i>	32	<i>16, 20, 27</i>	48	<i>17, 18, 20, 27</i>
7	<i>26</i>	16	<i>17, 27</i>	33	<i>17, 18, 19</i>	49	<i>18, 19, 21, 26</i>
8	<i>27</i>	17	<i>18, 19</i>	34	<i>17, 18, 20</i>		
			<i>18, 20</i>	35	<i>17, 18, 26</i>		
			<i>18, 26</i>	36	<i>17, 18, 27</i>		
			<i>18, 27</i>	37	<i>18, 19, 26</i>		
			<i>19, 26</i>	38	<i>18, 20, 27</i>		
			<i>20, 27</i>	39	<i>18, 21, 26</i>		
			<i>21, 26</i>	40	<i>18, 26, 27</i>		
			<i>21, 27</i>	41	<i>19, 21, 26</i>		
			<i>25, 27</i>				

Table 4.9: Table of 50 trigger combinations. Roman numbers indicate the order of the combination and Italicized numbers indicate the member triggers for corresponding trigger combination. The relationship between the actual member trigger and the italicized number can be seen in Table 4.8. A trigger combination with more than two triggers means all member triggers fired simultaneously for an event. For instance, trigger combination 19 indicates both trigger *18* (R12W1) and trigger *26* (R12W2_S) is fired at the same time.

To manage this issue a set of 50 specific trigger combination is defined. Table 4.9 shows the trigger combinations with its member triggers. These 50 trigger combinations are determined by each member trigger's sensitivity to the $W \rightarrow \mu$ events. The validity of the set is tested by existence of missing events: it is confirmed that there is no missing events among *Tight candidates*, however, the number of missing events increase as lower *Wness* cut is applied. Consequently, the measured fraction of each 50 trigger combination in the *Tight candidates* can be seen in Fig. 4.19.

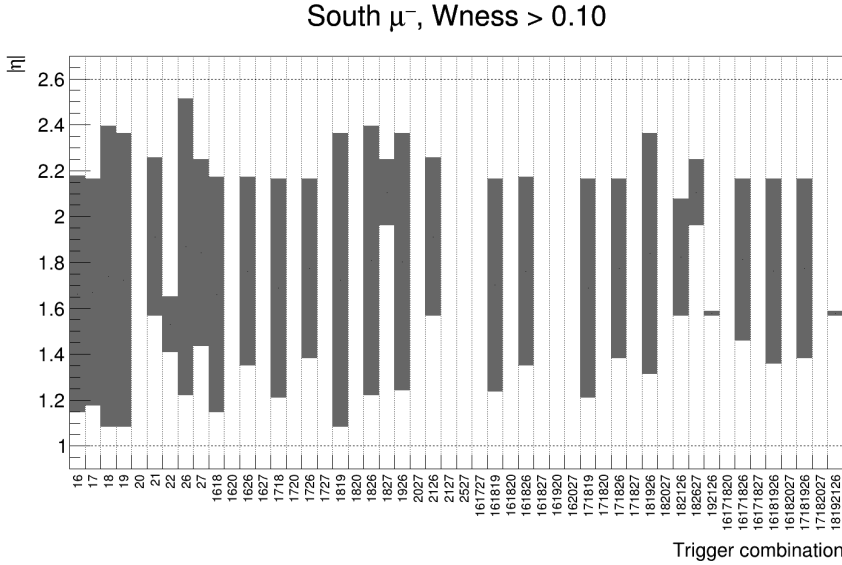


Figure 4.17: $|\eta|$ acceptance of 50 trigger combination. The black filled boxes indicate each trigger combination's effective acceptance and The dashed lines at 1.0 or 2.6 indicate physical limit of reconstructed tracks. Blank columns mean there's no event fired by corresponding trigger combination in the $Wness > 0.1$ condition.

As a next step, each trigger combination's effective η acceptance should be estimated to avoid underestimation. In detail, to avoid bias from the very triggers to be tested, the data cannot be used in the estimation of each trigger combination's efficiency. Therefore another set of muon candidates is defined by independent triggers such as ERT or MPC. But as these independent triggers' geometrical acceptances are completely irrelevant to the Muon Arms (muon triggers), underestimation is inevitable unless each trigger combination's acceptance is properly reflected. In conclusion each trigger combination's acceptance is measured by using the data. To reduce statistical uncertainty only $Wness > 0.1$ is applied. Fig. 4.17 shows an example of 50 trigger combination's acceptance.

Now each trigger combination's efficiency at *Tight candidates* condition is needed for the $\epsilon_{trig\,OA}$ calculation. As explained already the muon candidates from independent triggers are used for the estimation of each trigger combination's efficiency. With same reason to the effective acceptances, the statistics of these independent muon candidates cannot be rich. If the *Tight candidates* condition is applied remaining statistics are even more scarce. Therefore a loose cut in following list is defined and applied to these candidates: note that this cut is looser than *Basic cut*.

- $\chi^2 < 20$
- $DG0 < 20$ (cm)
- $DDG0 < 9$ (degree)
- $lastGap = 4$
- $1 < p_T < 60$ (GeV/c)
- $1.0 < |\eta| < 2.6$
- $Wness > 0.1$

Now the efficiency for a trigger combination can be estimated as follows:

$$\epsilon_{trigger\ comb} = \frac{\text{At least 1 independent trigger (raw) \& trigger combination (live)}}{\text{At least 1 independent trigger (raw)}} \quad (4.10)$$

But, again, this equation cannot be applied directly. By the low p_T events from loose cut there exist apparent turn-on behavior in trigger efficiency versus p_T . Also there exist clear linear correlation between the trigger efficiency and $Wness$. As required trigger efficiency is the one in the *Tight candidates* condition ($p_T > 16$, $Wness > 0.92$), there will be certain underestimation with additional uncertainty unless these issues are properly dealt with. Therefore following procedures are defined and performed for each trigger combination's efficiency estimation:

1. Divide whole $Wness$ range into several segments
2. Estimate plateau efficiency in p_T for each segments
(each trigger combination's acceptance is considered).
3. Define plateau efficiency vs. $Wness$ from the segment and perform linear fit
4. Extrapolate linear fit to $Wness = 0.96$ with 1σ confidence level

Fig. 4.18 shows an example of this procedure. All of each *Trigger combination*'s efficiency is estimated by using this procedure. Each estimated efficiency can be seen in Fig. 4.19. Note that *Trigger combination* with zero fraction are ignored during the efficiency estimation.

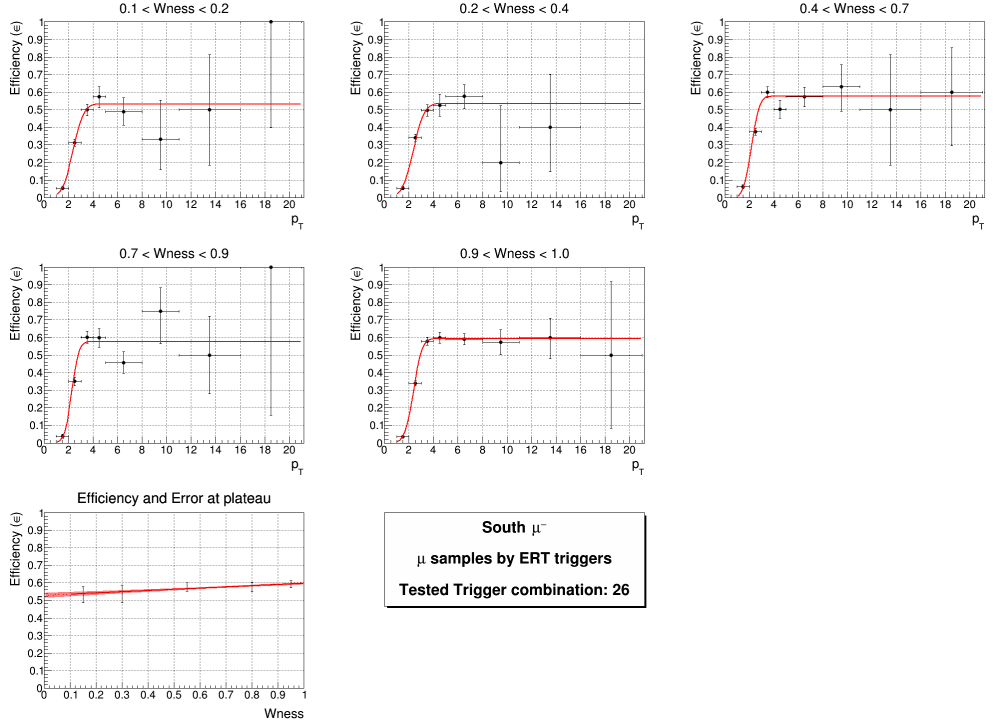


Figure 4.18: Example of the estimation procedures for a trigger combination's efficiency at *Tight candidates*. First five turn-on plots show extraction of plateau efficiency vs. p_T for each $Wness$ window. Bottom linear plot shows linear fit on plateau efficiencies and its 1σ CL extrapolation. Both p_T and $Wness$ windows set arbitrary to acquire enough statistics.

One important concern exist in the η dependence of the trigger combination's efficiency. The effective η acceptance only consider minimum and maximum acceptance of a trigger combination: for example, the trigger combination 19's (1826, R12W1 and R12W2_S) effective η acceptance is about $1.2 \sim 2.4$. However there could be a serious η dependence for the trigger combination's efficiency. Therefore the dependence tested with several trigger combinations with large fraction: the test is performed by dividing whole effective η acceptance into 2 to 3 segments. As a result, maximum $\pm 10\%$ of efficiency fluctuation is observed, however, it is not clear whether this fluctuation is originated from η dependence or limited statistics of independent muon candidates. Under the assumption of the efficiency is similar in all η acceptance further correction won't be applied.

Finally, once all trigger combinations' fraction and efficiency in *Tight candidates* is prepared the $\epsilon_{trig\,OA}$ and its error can be calculated as follows.

$$\epsilon_{trig\,OA} = \sum_{i=1}^{50} f_i \cdot \epsilon_i$$

$$\delta_{trig\,OA} = \sqrt{\sum_{i=1}^{50} (f_i \cdot \delta_i)^2} \quad (4.11)$$

The $\epsilon_{trig\,OA}$ estimation is performed by a couple of independent muon samples (ERT and MPC) to crosscheck its reliability. The results are summarized in Table 4.10. As the ERT sample is statistically rich, the results by ERT will be used as final $\epsilon_{trig\,OA}$ with additional systematic error by central value difference between two samples.

Arm and Charge	$\epsilon_{trig\,OA}$ (ERT)	$\epsilon_{trig\,OA}$ (MPC)	$\epsilon_{trig\,OA}$ (Final)
South μ^-	0.479 ± 0.005	0.505 ± 0.031	0.479 ± 0.031
South μ^+	0.466 ± 0.008	0.471 ± 0.025	0.466 ± 0.013
North μ^-	0.599 ± 0.021	0.589 ± 0.042	0.599 ± 0.031
North μ^+	0.591 ± 0.032	0.570 ± 0.046	0.591 ± 0.053

Table 4.10: Overall trigger efficiency at $W_{ness} > 0.92$. Note that MPC sample's statistics is $\sim 50\%$ to ERT after loose cut for independent muon candidates.

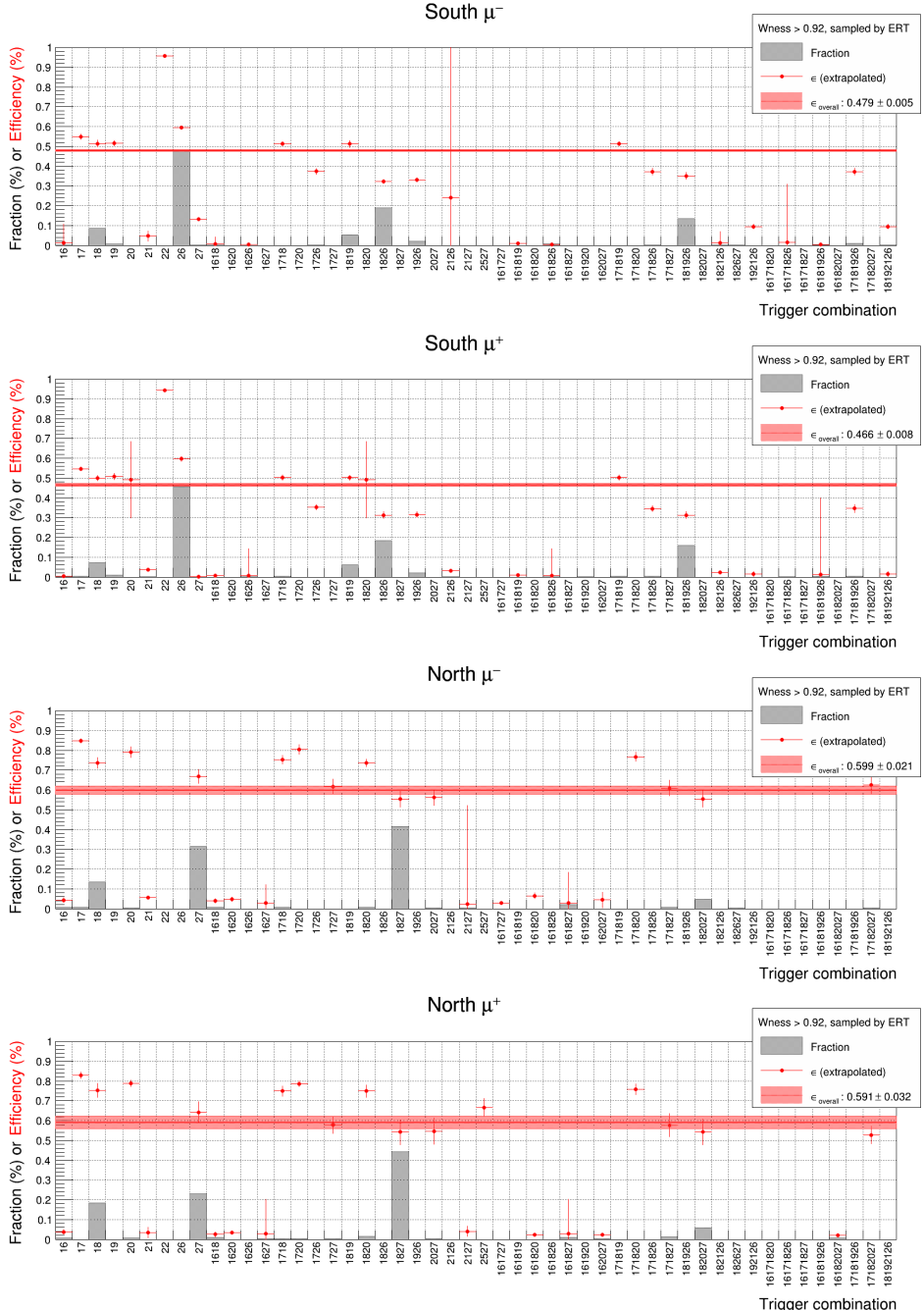


Figure 4.19: Results of $\epsilon_{trig OA}$ estimation by using ERT sample. trigger combination with no efficiency point means its fraction in *Final candidate* is 0.

4.2.5 Signal to Backgrounds Estimation

The *Tight candidates* are defined and its overall trigger efficiency has been measured. Now the amount of signal within the candidates, namely signal-to-background (S/BG) ratio need to be estimated to extract the A_L originated from W/Z . Due to the background's abundance even among the *Tight candidates* the S/BG will be extracted by extended unbinned maximum likelihood (EUML) fit. The information of EUML fit itself will be given later in this section.

Fit variables Following two kinematic variables are chosen as the fit variables.

- η (pseudorapidity)
- dw_{23} (reduced azimuthal bending between MuTr Station 2 and MuTr Station 3)

The definition of each variable can be found in section 4.2.1. Especially schematic diagram of the dw_{23} can be checked in Fig. 4.2. As these fit variables are independent of backgrounds filtering processes so far further backgrounds separation can be expected. These fit variables' independence to each other can be seen in Fig. 4.20.

Related to the Muon Arms' geometry η provides the information in the polar direction while dw_{23} provides information in the azimuthal direction. Especially the dw_{23} has fine resolution in the consistency check between p_T^{true} and p_T^{reco} . In detail, in the region of interest ($16 < p_T^{reco} < 60$) the signal track is likely to draw almost straight line if the multiple scattering is small. In other words, if the candidate is a signal the magnitude of the bending in the azimuthal direction would corresponds to its charge with very small deviation. The dilution by the momentum and the radial field strength is corrected by weighting $p_T^{reco} \sin\theta$. On the other hand, as explained in section 4.2.1 both type of backgrounds' $p_T^{true} < 20$ in most of cases. Thus the deviation of dw_{23} of the backgrounds likely to be larger than the signal. The 3rd column of Fig. 4.20 shows dw_{23} distribution for each type of muon candidates.

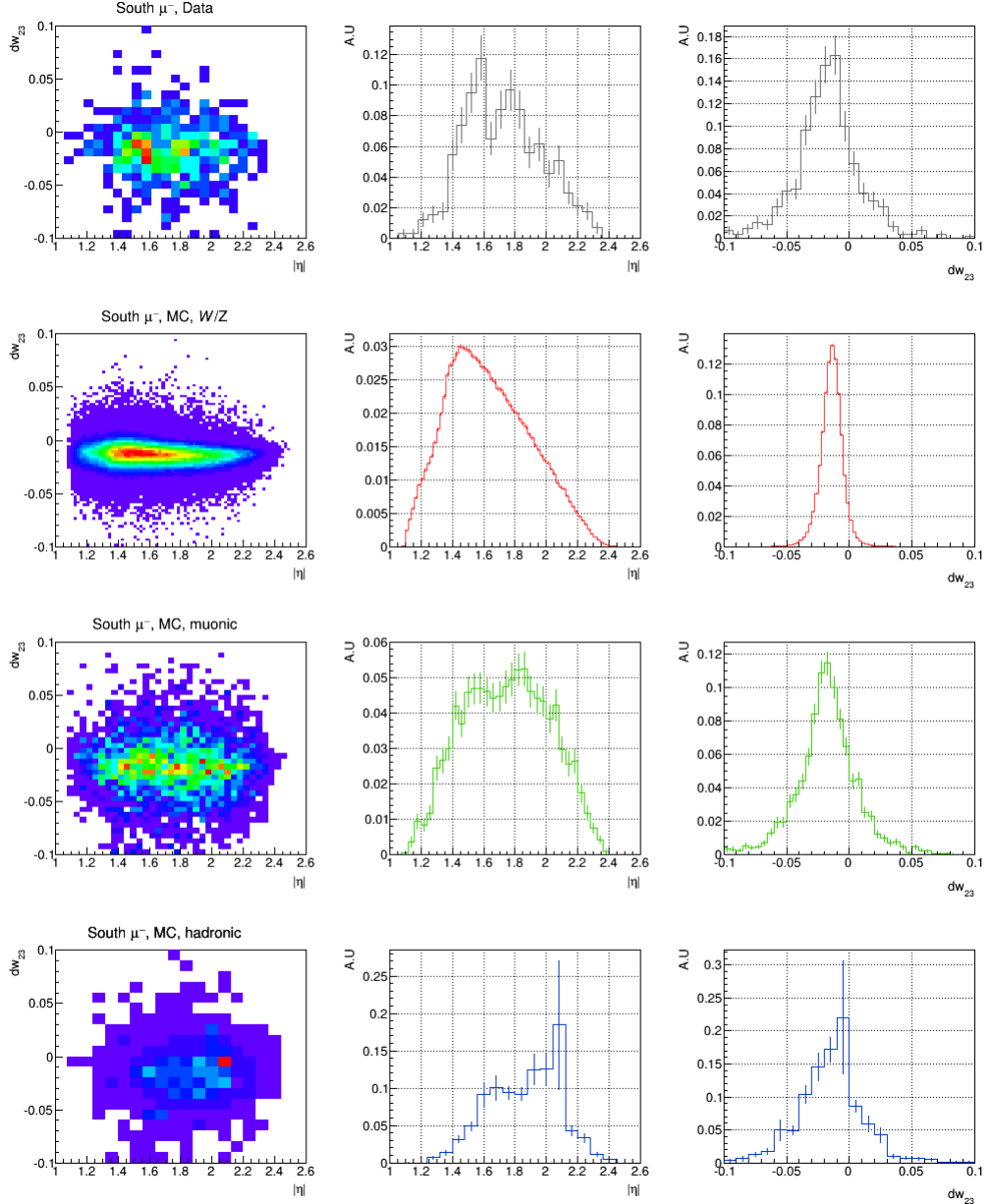


Figure 4.20: Distributions of fit variables in *Tight candidates* condition. Each row shows different type of muon candidates: data, signal MC, muonic backgrounds MC and hadronic backgrounds MC, respectively. The 2nd and 3rd column is a projection of 1st column's distribution onto each variable. Note that all MC is a stack of related subprocesses after scaling.

Composition of the PDFs To perform EUML fit one need to define a fit model composed of component PDFs representing signals or backgrounds. Therefore total 2×3 PDFs are defined for fit variables (η, dw_{23}) and each type of muon candidates (signal, muonic BG, hadronic BG). Relevant informations and characteristics are summarized in the following list.

- Common

- o Variables: η, dw_{23}
- o All three multiple collision conditions (Eq. 4.3) and their fractions (Table 4.4) are reflected in the composition of a PDF.

- Signals

- o Process: $W/Z \rightarrow \mu$
- o **Based on MC** scaled by production cross section with respect to the data luminosity
- o Variable W_{ness} and H_{ness} cut ($W_{ness_{event}} > W_{ness_{cut}}, H_{ness_{event}} < H_{ness_{cut}}$)

- Backgrounds: muonic

- o Process: Direct γ , Open b , Open c , Quarkonia, $W \rightarrow$ hadrons, $W \rightarrow \tau, Z/DY$ (inclusive), and $Z \rightarrow \mu$ (* $Z \rightarrow \mu$ is subtracted from Z/DY (inclusive) to avoid double counting)
- o **Based on MC** scaled by production cross section with respect to the data luminosity
- o Additionally scaled by k factor of 1.5
- o Additionally scaled by di-muon scaling factors (* explained in next paragraph)
- o Additionally scaled by overall trigger efficiency (Table 4.10)
- o Variable W_{ness} and H_{ness} cut ($W_{ness_{event}} > W_{ness_{cut}}, H_{ness_{event}} < H_{ness_{cut}}$)
- o **Fixed in the EUML fit**

- Backgrounds: hadronic

- o Process: mainly π and K
- o **Based on the data**
- o **Fixed W_{ness} and H_{ness} cut** ($W_{ness_{event}} > 0.90, H_{ness_{event}} > H_{ness_{cut, fixed}}$)
- o Additional cut: $FVTX_{cone} > 0$

Di-muon scale factors for muonic backgrounds Further muonic backgrounds rejection among *Tight candidates* is practically impossible as they are real muons originated from the collision vertex. However, as dominant generation processes are well verified the amount of muonic backgrounds in the *Tight candidates* can be estimated with reasonable precision: with the help of the measured di-muon yields the relative contributions of the real muon backgrounds can be obtained in a data-driven extraction. In this purpose a particular study was done by analyzers Hideyuki Oide and Sanghwa Park. Note that following informations are based on the results of the study and quoted from [11].

To study these scaling factors a set of di-muon candidates is defined by following cuts:

- $\chi^2 < 20$
 - $DG0 < 20$
 - $DDG0 < 9$
 - $lastGap = 4$
 - $1.2 < |\eta| < 2.0$
 - $1.2 < |\phi_0 - \phi_1| < 5.8$
 - Triggered by MUID1D for $M_{\mu^+\mu^-} < 7$ (GeV/c²) (* check Table 4.8 for the triggers)
 - Triggered by R12W1 for $M_{\mu^+\mu^-} > 7$ (GeV/c²)
 - Combinatorial backgrounds subtraction by like-sign candidates:
- $$N'_{(+-)} = N_{(+-)} - 2\sqrt{N_{(++)} \times N_{(--)}} \quad (1)$$

Note that these cuts do not include p_T . Also azimuthal angle difference cut is applied to reject the jets. For the combinatorial backgrounds subtraction it is assumed that the backgrounds are independent of muon charge combination. Once the data is defined MC in the same condition is produced by PYTHIA + PISA.

The general procedure of this study is summarized in following list. And the relevant informations including final scaling factors are summarized in Table 4.11. Fig. 4.21 shows the final fit for each Arm and mass range. Lastly there exist correlations among each di-muon processes and its covariance will be counted in the determination of systematic error. The correlation matrix can be seen in Table 4.12.

Process	σ/pb	Final scaling factors
Open b	7.56×10^{-3}	3.186 ± 1.064
Open c	5.78×10^{-1}	3.539 ± 0.823
J/ψ	9.01×10^{-4}	0.506 ± 0.016
ψ_2	3.52×10^{-4}	
Υ (1s)	7.96×10^{-7}	0.634 ± 0.079
Υ (2s)	5.26×10^{-7}	
Υ (3s)	4.16×10^{-7}	
Z/DY	1.72×10^{-4}	1.445 ± 0.353
ϵ_{trig} (MUID1D) :		0.93 ± 0.07 (S), 0.94 ± 0.06 (N)
ϵ_{trig} (R12W1) :		0.82 ± 0.06 (S), 0.84 ± 0.05 (N)

Table 4.11: Relevant informations of di-muon scaling factors. Note that the trigger efficiencies are obtained in Run 11.

General procedures of the di-muon scale factor study:

1. Scale each MC sample by luminosity with respect to the data
2. Scale each MC sample by trigger acceptance and efficiency
3. Stack scaled samples and test match to the data by a least-squares fit.
The fitting is performed for both Arms and both mass ranges at the same time.
4. Introduce additional scaling factors to each process if necessary,
then repeat 3 until best match found

	Global	Open b	Open c	J/ψ	Υ	Z/DY
Open b	0.95	+ 1.00	- 0.79	- 0.26	+ 0.04	- 0.78
Open c	0.90	- 0.79	+ 1.00	- 0.17	+ 0.05	+ 0.48
J/ψ	0.68	- 0.26	- 0.17	+ 1.00	- 0.04	+ 0.29
Υ	0.62	+ 0.04	+ 0.05	- 0.04	+ 1.00	- 0.41
Z/DY	0.88	- 0.78	+ 0.48	+ 0.29	- 0.41	+ 1.00

Table 4.12: Correlation among di-muon processes in the least-squares fit on the di-muon spectrum.

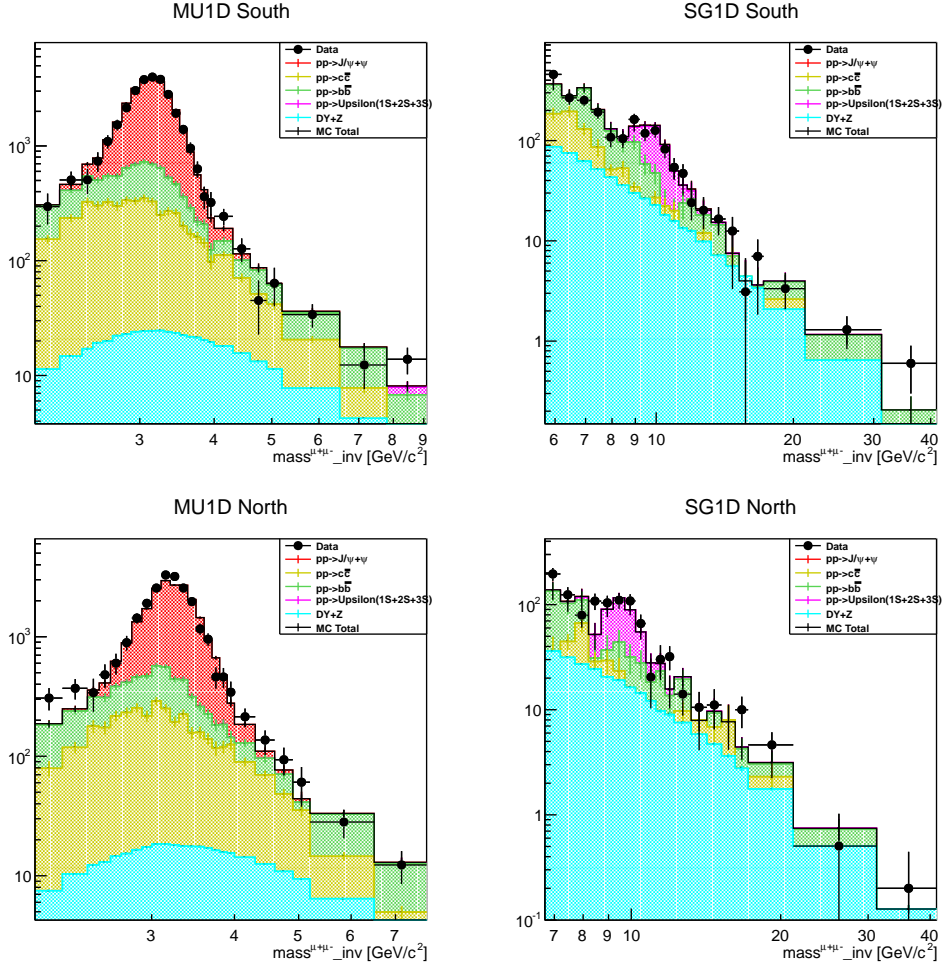


Figure 4.21: Final di-muon fit results by Sanghwa Park. Left column shows low mass region triggered by MUID1D (MU1D) and Right column shows high mass region by R12W1 (SG1D). This plot is quoted from [11].

Extended unbinned maximum likelihood fit The dataset with relatively high purity is defined. Also each type of muon candidates are known with its probability density distribution. Now the extended unbinned maximum likelihood fit will be used to extract the contribution of each type of candidates in the dataset. The ‘extended’ unbinned maximum likelihood fit is the maximum likelihood fit which takes into account the Poisson statistics of the number of events.

Let’s set a few notations first:

- X : dataset to be fit composed of N candidates
- x_i : i th candidate of X ($i = 1, 2, 3, \dots, N$).
- A x_i is composed of two fit variables ($x_i = (\eta, dw_{23})_i$).
- $\lambda_t(x_i)$: a normalized 2D PDF for a type of candidate ($\lambda_{sig}(x_i), \lambda_{mbg}(x_i), \lambda_{hbg}(x_i)$).
- n_t : the number of events for a type of muon candidates ($n_{sig}, n_{mbg}, n_{hbg}$)

Note that each PDF satisfies *Tight candidates* condition. Once the PDFs are defined then EUML fit function can be defined as follows. The parameter to be fit is n_t .

$$L(\{n_t\}|X) = \frac{n^N e^{-n}}{N!} \prod_{x_i \in X} \left[\sum_{t=1}^3 \frac{n_t}{n} \lambda_t(x_i) \right], \quad n = \sum_{t=1}^3 n_t \quad (4.12)$$

Technically negative log likelihood (NLL) of the fit function is minimized to find the best match between the data and the fit model.

$$\text{NLL} = -\log(L(\{n_t\}|X)) \quad (4.13)$$

As explained in the previous paragraphs the PDF for muonic backgrounds is fixed as the scaled value during the fit. Following Fig. 4.22, Fig. 4.23, and Table 4.14 shows the EUML fit results for the *Tight candidates*. Note that the fit on η is usually poorer than dw_{23} : it is likely an effect from η dependence of the Overall trigger efficiency. Also as the signals in dw_{23} is relatively concentrated compared to the backgrounds, additional sidebands cut will be applied to separate backgrounds further.

This EUML fit will be repeated with various *Wness* to find optimal point with minimum A_L error.

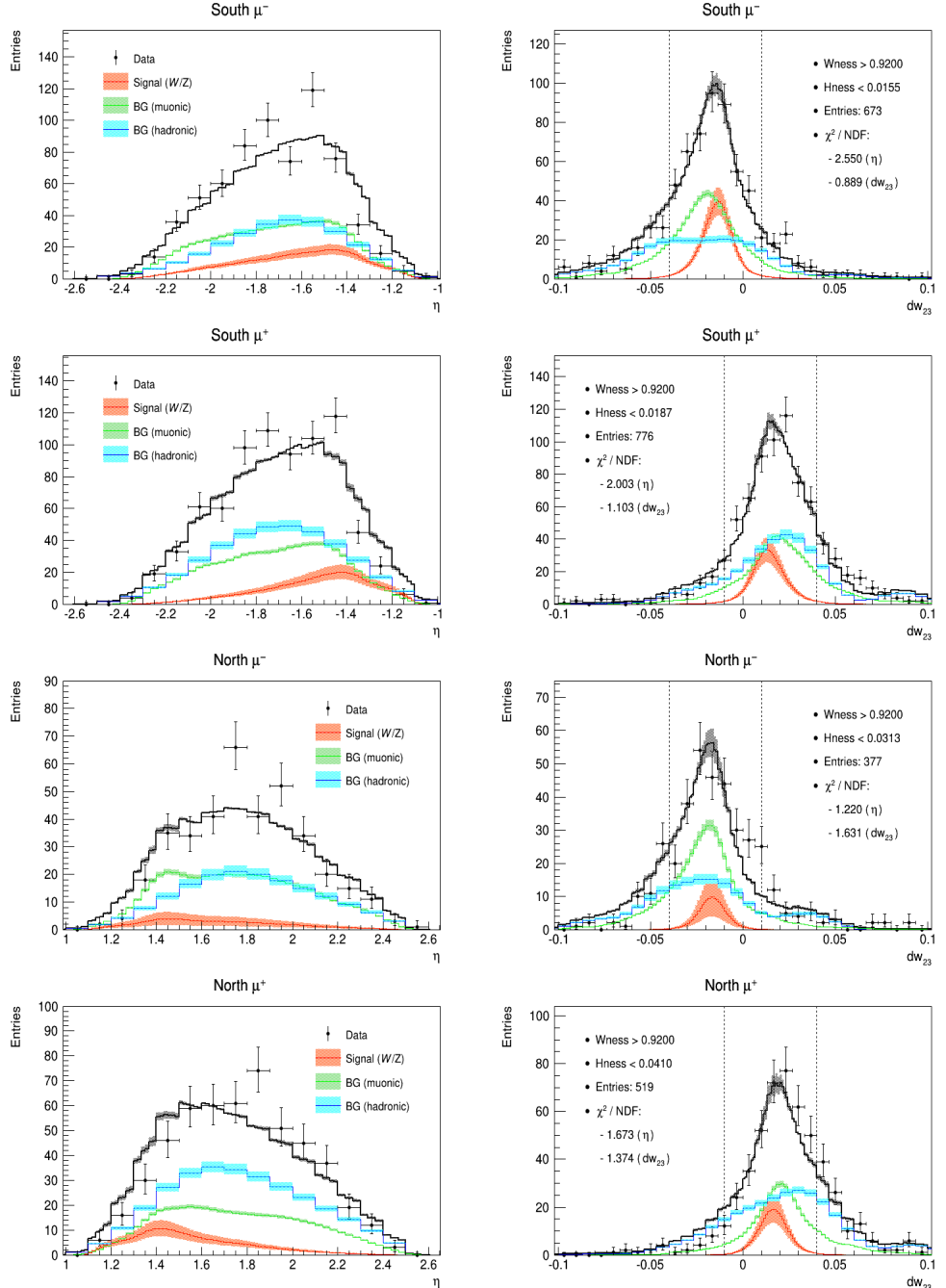


Figure 4.22: Unbinned maximum likelihood fit on data at $Wness > 0.92$ and optimal $Hness$. Each plot indicates a 2D fit's projection onto η (left) or dw_{23} (right). The dashed lines in dw_{23} projections indicate sidebands cut condition.

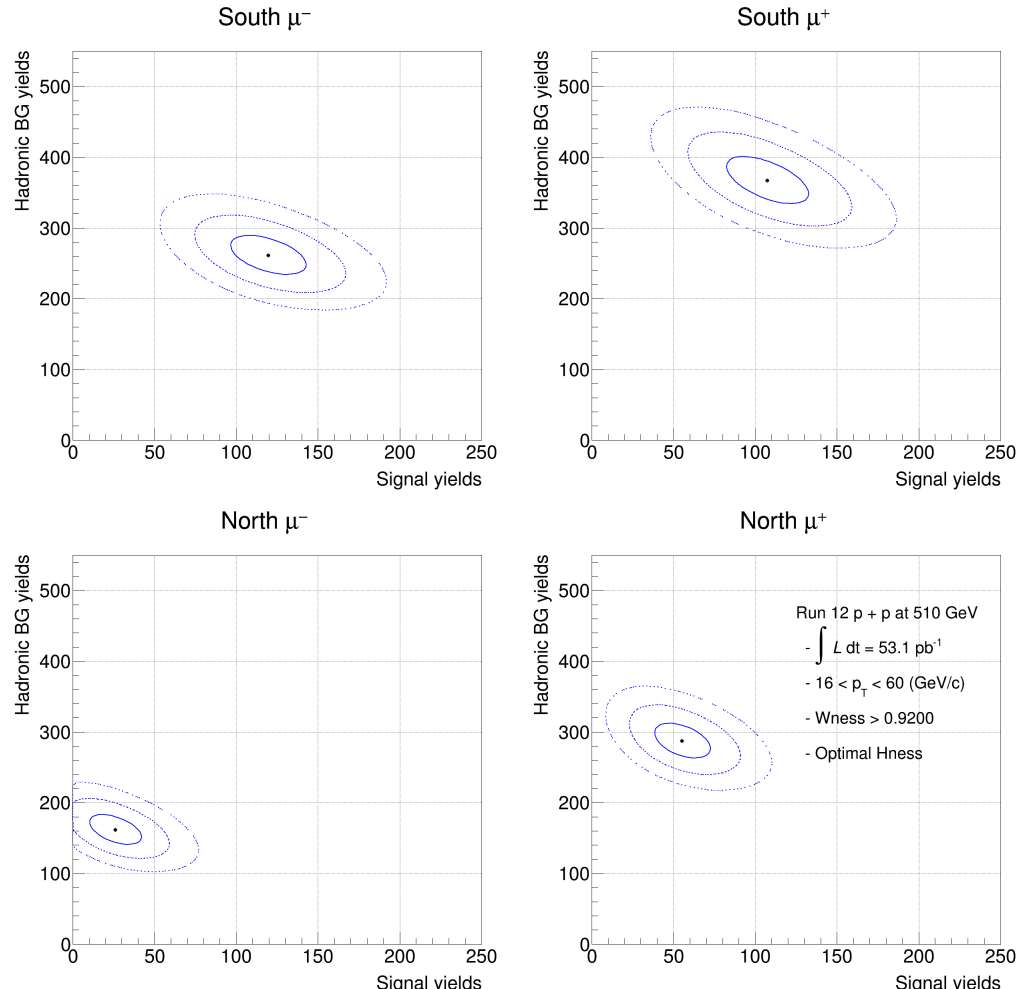


Figure 4.23: NLL contours of the unbinned max. likelihood fit in Fig. 4.22. Solid, Dashed, and Dotted line indicates 1σ , 2σ , and 3σ deviataion, respectively.

Arm and Charge	$\int \lambda_{sig} dx$	$\int \lambda_{mbg} dx$	$\int \lambda_{hbg} dx$
South μ^-	0.9645	0.7526	0.5434
South μ^+	0.9574	0.7377	0.6595
North μ^-	0.9866	0.7553	0.5608
North μ^+	0.9833	0.7657	0.5830
Sidebands cut		$\mu^- : -0.04 < dw_{23} < 0.01$	
		$\mu^+ : -0.01 < dw_{23} < 0.04$	

Table 4.13: Integrated probability density of each type of PDF after dw_{23} sidebands removal. The conditions are same to Fig. 4.22 and Fig. 4.23.

	South μ^-	South μ^+	North μ^-	North μ^+
W_{ness}		0.92		
H_{ness}	0.015530	0.018732	0.031267	0.040963
Entries	483	578	274	378
n_{sig}	115^{+23}_{-22}	103^{+24}_{-24}	26^{+16}_{-15}	54^{+17}_{-16}
n_{mbg}	209	202	133	125
n_{hbg}	142^{+15}_{-15}	242^{+22}_{-22}	91^{+12}_{-12}	167^{+15}_{-14}
S/BG	$0.328^{+0.081}_{-0.073}$	$0.231^{+0.070}_{-0.062}$	$0.114^{+0.082}_{-0.070}$	$0.186^{+0.071}_{-0.062}$

Table 4.14: Estimated number of signals and backgrounds. Note that Entries and S/BG are the values after sidebands cut. The other conditions are same to Fig. 4.22 and Fig. 4.23.

4.3 Single Spin Asymmetry Estimation

4.3.1 Introduction

A set of muon candidates defined and its S/BG is estimated. But still a few additional factors need to be considered to extract the A_L originated from W bosons. First of all, under the assumption of each beam's polarization is aligned in 100 % efficiency, the A_L and A_{LL} (double longitudinal spin asymmetry) can be expressed as follows.

$$A_L = \frac{\sigma_+ - \sigma_-}{\sigma_+ + \sigma_-}, \quad A_{LL} = \frac{\sigma_{++} - \sigma_{+-}}{\sigma_{++} + \sigma_{+-}} \quad (4.14)$$

Here the subscripts mean helicity of the polarized protons: (+) means positive (right-handed) helicity and (-) means negative (left-handed) helicity, respectively. Therefore σ_{\pm} means longitudinal cross section originated from corresponding helicity. But this relationship becomes more complicated if systematic conditions are counted in.

A collision at the PHENIX is performed by crossing a couple of beams which circulate the RHIC in clockwise or counter-clockwise direction. Thus both beam's helicities are involved in a cross section's determination. Note that each beam is composed of 107 effective bunches out of 120 which has positive or negative helicity, as explained in 2.1.2. In reality the polarization of the beam cannot be 100 %: The beam polarization fluctuate Fill by Fill, however, Fill by Fill analysis is unavailable in this analysis due to scarcity of the W s. Thus an average beam polarization for all Fills will be used. Let's put conditions so far in order as follows. Note that the notations in the list will be used hereafter to denote corresponding conditions.

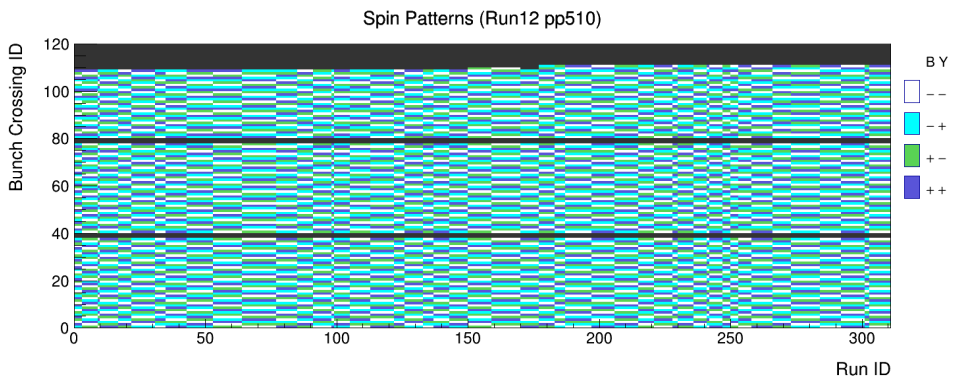


Figure 4.24: Map of the Spin patterns

- Beams: **Blue (cw)** and **Yellow (ccw)**
- Spin patterns: Combination of each beam's helicity (positive (+) or negative (-)) per bunch crossing. In this thesis always consider Blue beam's helicity first. Total four types of spin patterns exist in Run12 pp510: $(++)$, $(+-)$, $(-+)$, and $(--)$.
- Average beam polarization of both beams: $\langle P_B \rangle$ and $\langle P_Y \rangle$

Then Eq. 4.14 modified as follows.

$$\begin{aligned}
 A_{L, B} &= \frac{1}{\langle P_B \rangle} \cdot \frac{(\sigma_{++} + \sigma_{+-}) - (\sigma_{-+} + \sigma_{--})}{(\sigma_{++} + \sigma_{+-}) + (\sigma_{-+} + \sigma_{--})} \\
 A_{L, Y} &= \frac{1}{\langle P_Y \rangle} \cdot \frac{(\sigma_{++} + \sigma_{-+}) - (\sigma_{+-} + \sigma_{--})}{(\sigma_{++} + \sigma_{-+}) + (\sigma_{+-} + \sigma_{--})} \\
 A_{LL} &= \frac{1}{\langle P_B \rangle \langle P_Y \rangle} \cdot \frac{(\sigma_{++} - \sigma_{+-}) - (\sigma_{-+} - \sigma_{--})}{(\sigma_{++} + \sigma_{+-}) + (\sigma_{-+} + \sigma_{--})}
 \end{aligned} \tag{4.15}$$

The actual measurement of cross section is performed by collecting muon candidates at each Muon Arms. The position of each Muon Arm (south or north) can be either forward or backward with respect to each beam's going direction. In addition, although Spin patterns are set in almost equal ratio in Run 12, the number of muons can be different by type of the spin pattern. Lastly not all of muon candidates are originated from desired W bosons thus its ratio need to be corrected by S/BG measured by EUML fit. Let's clear these conditions up similar to the previous case.

- Muon Arm's position with respect to the beam going direction
 - Forward (FW): North (N) for Blue, South (S) for Yellow
 - Backward (BW): South (S) for Blue, North (N) for Yellow
- L_{ij} : relative luminosity in corresponding Spin pattern
(* no subscript means total luminosity: $L = L_{++} + L_{+-} + L_{-+} + L_{--}$)
- m : number of muon candidates collected in certain conditions (Arm, Spin pattern, and type).
(ex. $m_{(+-, sig)}^S$: signal muons collected in South for (+) in Blue and (-) in Yellow)
- n : m corrected by relative luminosity (ex. $n_{+-} = m \cdot \frac{L_{+-}}{L}$)

Technically what actually measured is the m . Following relationship holds between the m and the asymmetries:

$$\begin{aligned}
n_{ij} &= m_{ij} \cdot \frac{L_{ij}}{L} \\
&= (1 + i \cdot A_{L,B} P_B + j \cdot A_{L,Y} P_Y + ij \cdot A_{LL} P_B P_Y) n_{ij, sig} + n_{ij, BG}
\end{aligned} \tag{4.16}$$

where i and j means helicity of each beam. It can be unfolded by corresponding Spin pattern as follows.

$$\begin{aligned}
n_{++} &= (1 + A_{L,B} P_B + A_{L,Y} P_Y + A_{LL} P_B P_Y) n_{++, sig} + n_{++, BG} \\
n_{+-} &= (1 + A_{L,B} P_B - A_{L,Y} P_Y - A_{LL} P_B P_Y) n_{+-, sig} + n_{+-, BG} \\
n_{-+} &= (1 - A_{L,B} P_B + A_{L,Y} P_Y - A_{LL} P_B P_Y) n_{-+, sig} + n_{-+, BG} \\
n_{--} &= (1 - A_{L,B} P_B - A_{L,Y} P_Y + A_{LL} P_B P_Y) n_{--, sig} + n_{--, BG}
\end{aligned} \tag{4.17}$$

Now Eq. 4.15 modified again in following form.

$$\begin{aligned}
A_{L,B} &= \frac{1}{\langle P_B \rangle} \cdot \frac{(n_{++} + n_{+-}) - (n_{-+} + n_{--})}{(n_{++} + n_{+-}) + (n_{-+} + n_{--})} \cdot (1 + \frac{1}{S/BG}) \\
&= \frac{\epsilon_{L,B}}{\langle P_B \rangle} \cdot (1 + \frac{1}{S/BG}) \\
A_{L,Y} &= \frac{1}{\langle P_Y \rangle} \cdot \frac{(n_{++} + n_{-+}) - (n_{+-} + n_{--})}{(n_{++} + n_{-+}) + (n_{+-} + n_{--})} \cdot (1 + \frac{1}{S/BG}) \\
&= \frac{\epsilon_{L,Y}}{\langle P_Y \rangle} \cdot (1 + \frac{1}{S/BG}) \\
A_{LL} &= \frac{1}{\langle P_B \rangle \langle P_Y \rangle} \cdot \frac{(n_{++} - n_{+-}) - (n_{-+} - n_{--})}{(n_{++} + n_{+-}) + (n_{-+} + n_{--})} \cdot (1 + \frac{1}{S/BG}) \\
&= \frac{\epsilon_{LL}}{\langle P_B \rangle \langle P_Y \rangle} \cdot (1 + \frac{1}{S/BG})
\end{aligned} \tag{4.18}$$

Note that ϵ means raw asymmetry calculated directly from the number of muons. Finally the measured position with respect to the beam should be considered. The S or N indicates Muon Arm south or Muon Arm north.

$$\begin{aligned}
A_L^{FW} &= A_{L,B}^N, A_{L,Y}^S \\
A_L^{BW} &= A_{L,B}^S, A_{L,Y}^N
\end{aligned} \tag{4.19}$$

In conclusion, to estimate the A_L following four components are essentially required.

1. Average beam polarization ($\langle P \rangle$)
2. Relative luminosity by Spin pattern (L_{ij})
3. Raw asymmetry for each Arm and Charge (ϵ)
4. S/BG ratio for each Arm and Charge

Note that systematic uncertainties should be considered in addition to these essential parts. Therefore remaining sections treat each subjects in following order: section 4.3.2 explains collecting the essential components, section 4.3.3 explains sources of systematic uncertainties and its effect, and lastly section 4.3.4 explains the final results, respectively.

4.3.2 A_L Estimation

Average beam polarization Fig. 4.25 shows polarization values in the Run 12 data taking period [34]. Note that not all of the Fills during the Run are included: some fills are omitted by the Run QA.

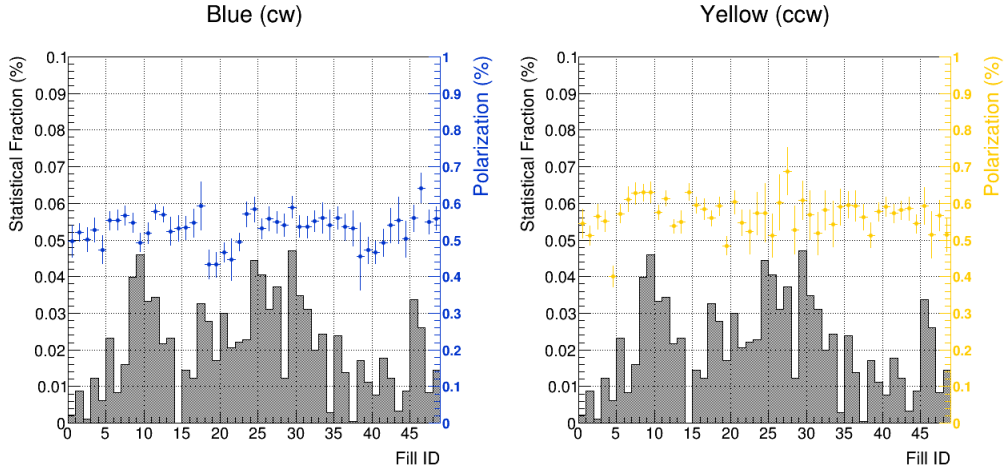


Figure 4.25: Statistical fraction under *Tight candidates* condition and Polarization of each beam.

The average beam polarization is calculated similar to the case of the Overall trigger efficiency (Eq. 4.11). However in this case the standard deviation of the mean is considered as well. For the case of strong Fill by Fill luminosity dependence, the luminosity weighted $\langle P \rangle$ is estimated in parallel to $\langle P \rangle$ without weight. Note that the Fill by Fill luminosity is the one at the *Tight candidates* condition. As Table 4.15 shows the luminosity does not affect $\langle P \rangle$ seriously, but the weighted $\langle P \rangle$ will be used as the final polarization in the remaining processes.

Fill L weighted	$\langle P_B \rangle$	$\langle P_Y \rangle$
\times	$0.530 \pm 0.039 (0.034 + 0.005)$	$0.568 \pm 0.040 (0.034 + 0.006)$
\circ	$0.536 \pm 0.041 (0.035 + 0.006)$	$0.574 \pm 0.043 (0.035 + 0.008)$

Table 4.15: Average polarization in Run 12. First type of error indicates standard deviation of the mean and Second type of error indicates propagated average of the Fill by Fill polarization error.

Relative luminosity by Spin pattern Basically four Spin patterns are supposed to have same amount of integrated luminosity. However, if there exist inequality among Spin patterns by certain systematic condition, the asymmetry must be corrected by their relative ratio to avoid bias from luminosity difference.

Therefore the relative luminosity is studied by scaler databases independent of the data. The $\text{BBC}_{\text{noVtx}}$ counts are obtained from Star Scaler and The crossing by crossing Spin patterns are obtained from Spin database. The GL1p database is also consulted but only used for the QA purpose. Note that the pileup effect from multiple collisions is corrected for the $\text{BBC}_{\text{noVtx}}$ counts. Also only 272 out of 311 physics runs are used in this study: 39 runs' scaler counts are ignored as they show suspicious behavior. The conditions for the run selection are as follows:

- $0.99 < \text{BBC}_{30\text{cm}, \text{SS}} / \text{BBC}_{30\text{cm}, \text{GL1p}} < 1.01$
- $0.99 < \text{BBC}_{15\text{cm}, \text{SS}} / \text{BBC}_{15\text{cm}, \text{GL1p}} < 1.01$
- $0.99 < \text{BBC}_{\text{South Exclusive, SS}} / \text{BBC}_{\text{North Exclusive, SS}} < 1.01$

where SS means Star Scaler. As the result shows maximum deviation for a Spin pattern is only 0.6 %. Since only a few hundreds of muons remain as *Tight candidates* additional relative luminosity correction won't be required in the estimation of A_L .

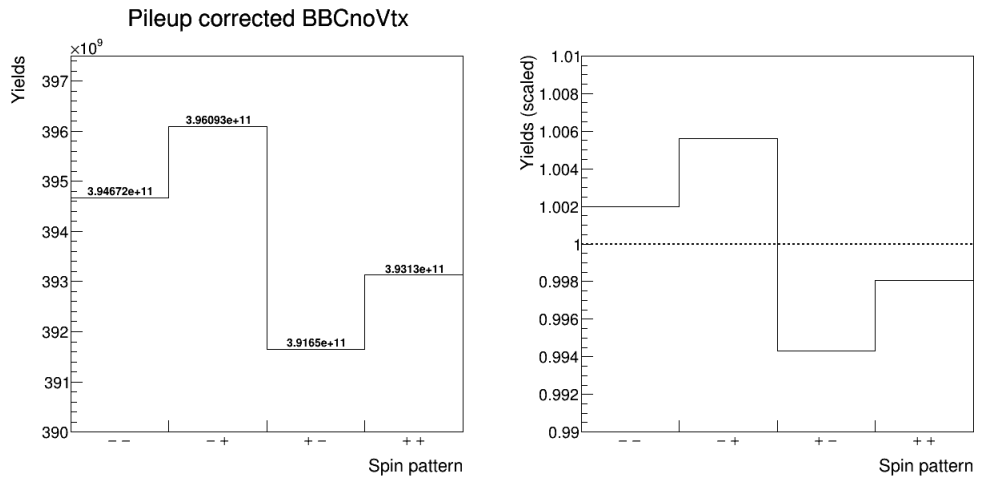


Figure 4.26: Pileup corrected $\text{BBC}_{\text{noVtx}}$ yields by Spin pattern. Left plot shows raw yields and Right plot shows scaled yields by $1/(\text{total yields} \times 0.25)$.

Raw asymmetry and S/BG As mentioned in the determination of the *Wness* for *Tight candidates* (Eq. 4.8), the optimal *Wness* for the final A_L should be determined by a FoM test. In principle by applying tighter *Wness* cut higher S/BG is expected with reduced uncertainty, however, this tighter cut will increase statistical uncertainty at the same time.

Therefore to find the optimal point with minimum uncertainty both raw asymmetry (ϵ) and S/BG measured simultaneously with various *Wness*. The scan is performed in the range of $0.92 < \text{Wness} < 0.99$ with stepsize of 0.001. Note that the Sidebands cut is applied basically in the estimation of both ϵ and S/BG. The sum of uncertainty is defined as follows:

$$\begin{aligned}\delta A_{L, \langle P \rangle} &= \left| \frac{1}{\langle P \rangle + \delta P} - \frac{1}{\langle P \rangle} \right| \cdot \epsilon_L \cdot \left(1 + \frac{1}{\text{S/BG}} \right) \\ \delta A_{L, \epsilon} &= \frac{1}{\langle P \rangle} \cdot \left| \delta \epsilon_L \right| \cdot \left(1 + \frac{1}{\text{S/BG}} \right) \\ \delta A_{L, \text{S/BG}} &= \frac{1}{\langle P \rangle} \cdot \epsilon_L \cdot \left(1 + \left| \frac{1}{\text{S/BG} + \delta(\text{S/BG})} - \frac{1}{\text{S/BG}} \right| \right)\end{aligned}\quad (4.20)$$

$$\Delta A_L = \sqrt{\sum \delta A_L^2}$$

where $\delta A_{L, \langle P \rangle}$ indicates uncertainty from the beam polarization, $\delta A_{L, \epsilon}$ indicates uncertainty from the raw asymmetry, $\delta A_{L, \text{S/BG}}$ indicates uncertainty from the S/BG, and ΔA_L indicates quadratic sum of previous three uncertainties, repectively.

Now a FoM can be set by using the ΔA_L of both beams:

$$\text{FoM} = \frac{1}{\Delta A_{L, B} + \Delta A_{L, Y}} \quad (4.21)$$

Note that the systematic unertainty is not considered at this stage. By its definition the FoM will be maximum when sum of both beam's uncertainty is minimum. The results of the scan can be seen in Fig. 4.27 and Fig. 4.28. The relevant parameters at *Wness* for the maximum FoM can be checked in Fig. 4.30 and Table 4.16.

Hereafter the muon candidates satisfying following conditions will be denoted as *Final canndidates*.

- *Wness* at maximum FoM
- $Hness_{opt}$ at maximum FoM *Wness*
- dw_{23} sidebands removed

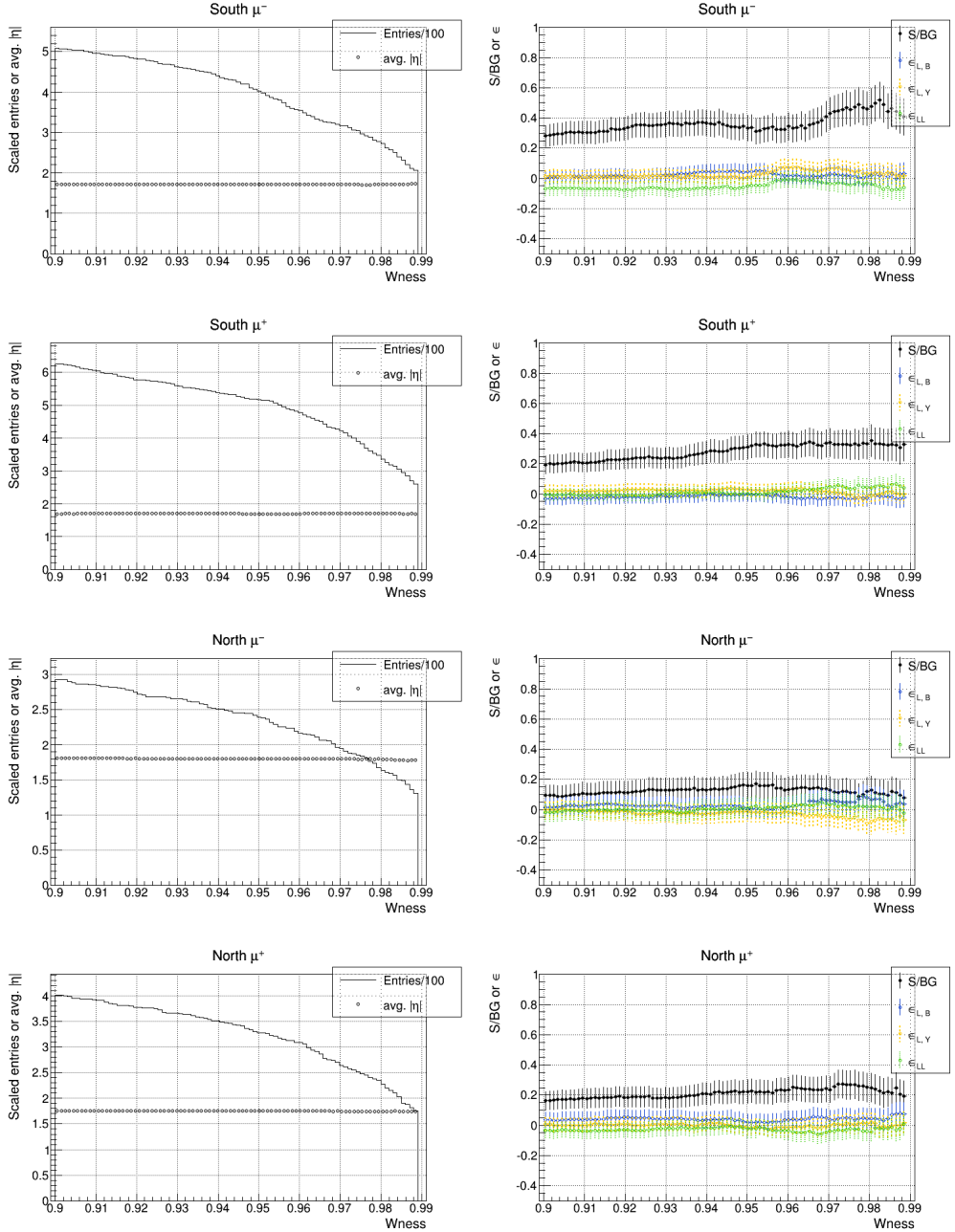


Figure 4.27: Parameters of the $Wness$ scan for each Arm and Charge. Left column shows number of muon candidates (scaled) and its average $|\eta|$ and Right column shows S/BG ratio, $\epsilon_{L,B}$, $\epsilon_{L,Y}$, and ϵ_{LL} , respectively.

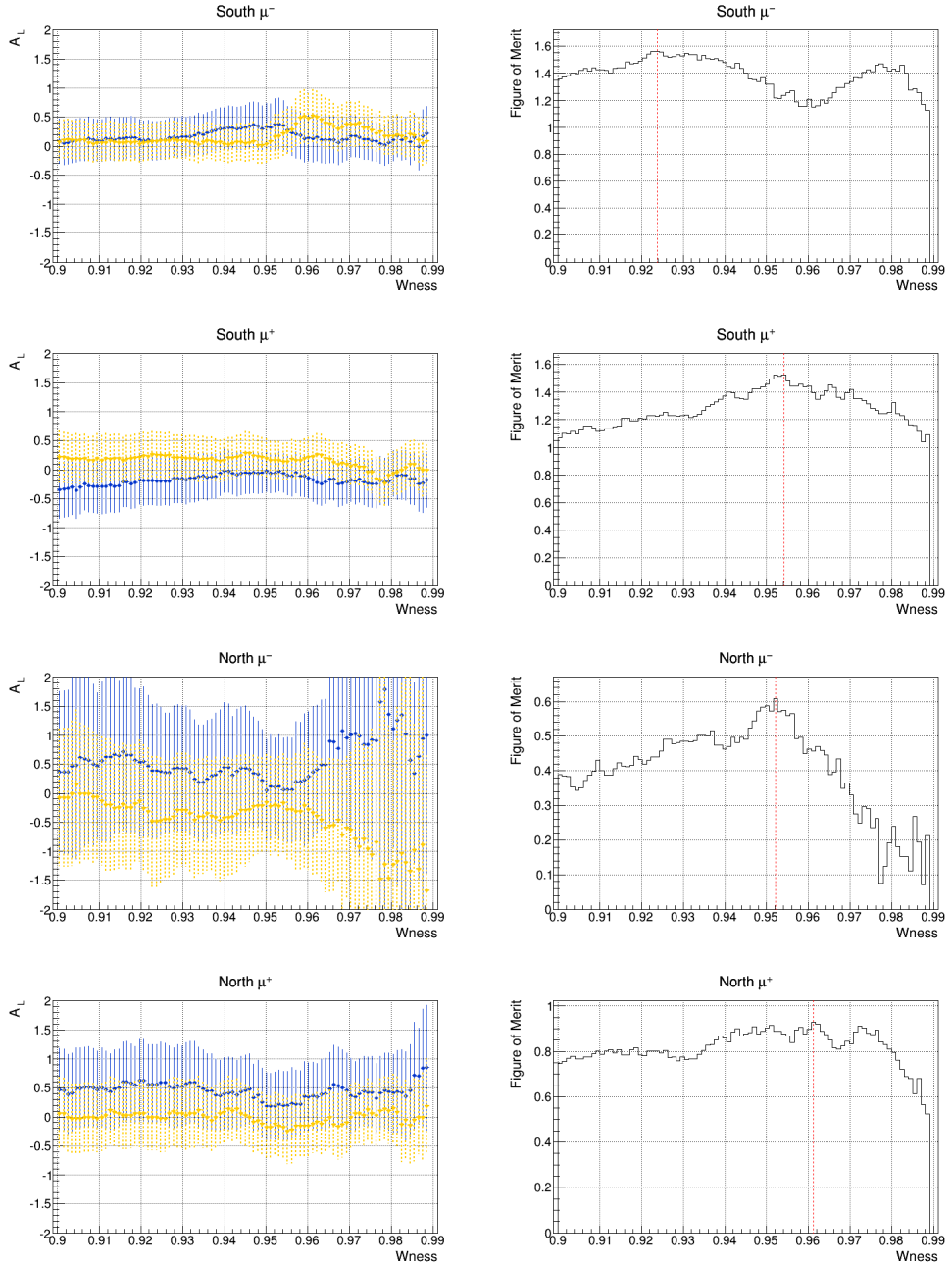


Figure 4.28: Results of the W_{ness} scan for each Arm and charge. Left column shows A_L of both beams with combined error in Eq. 4.20 and Right column shows FoM defined by Eq. 4.21. Note that systematic uncertainties are not included in the combined errors.

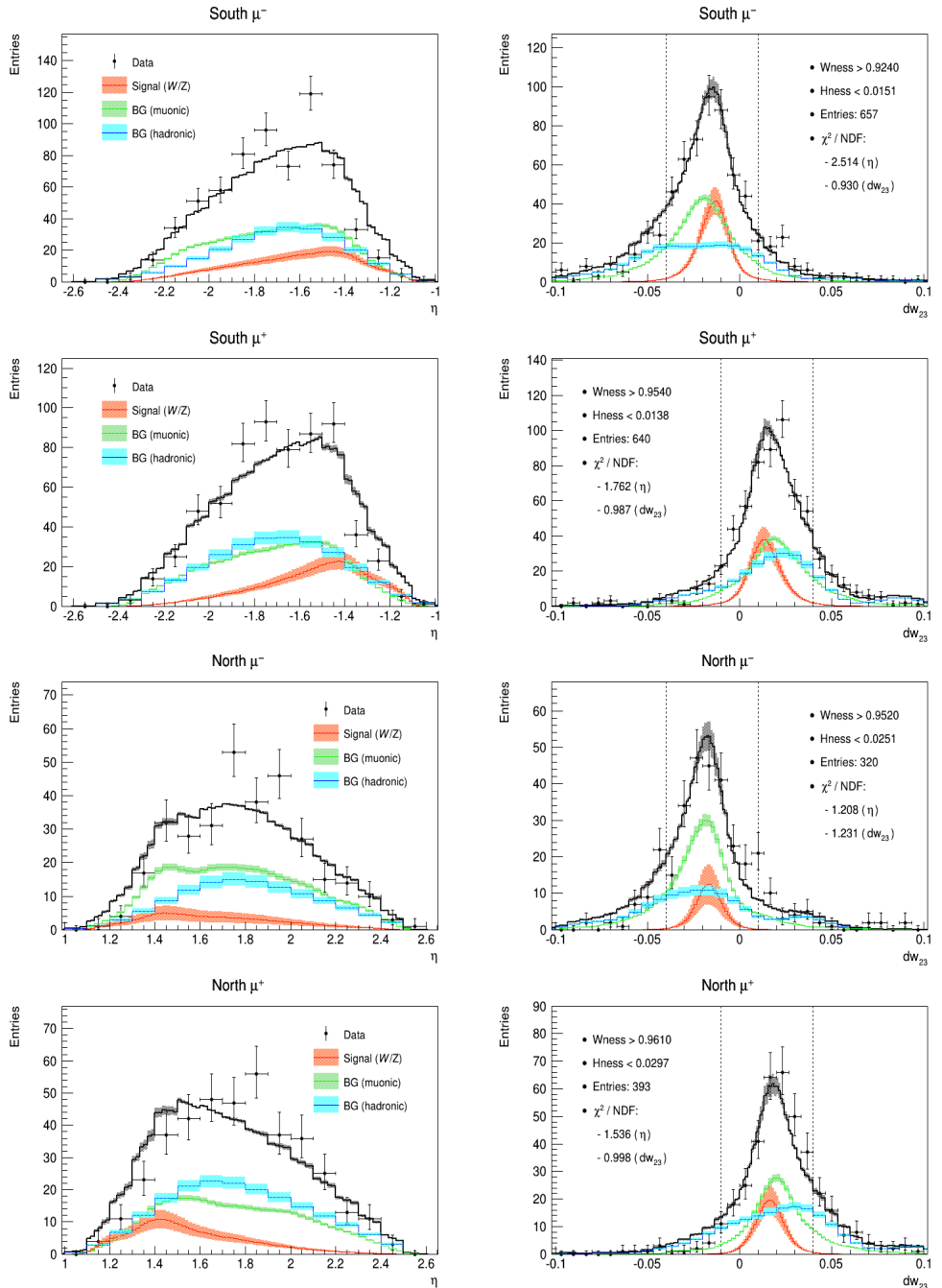


Figure 4.29: EUML fit results for the conditions at maximum FoM.

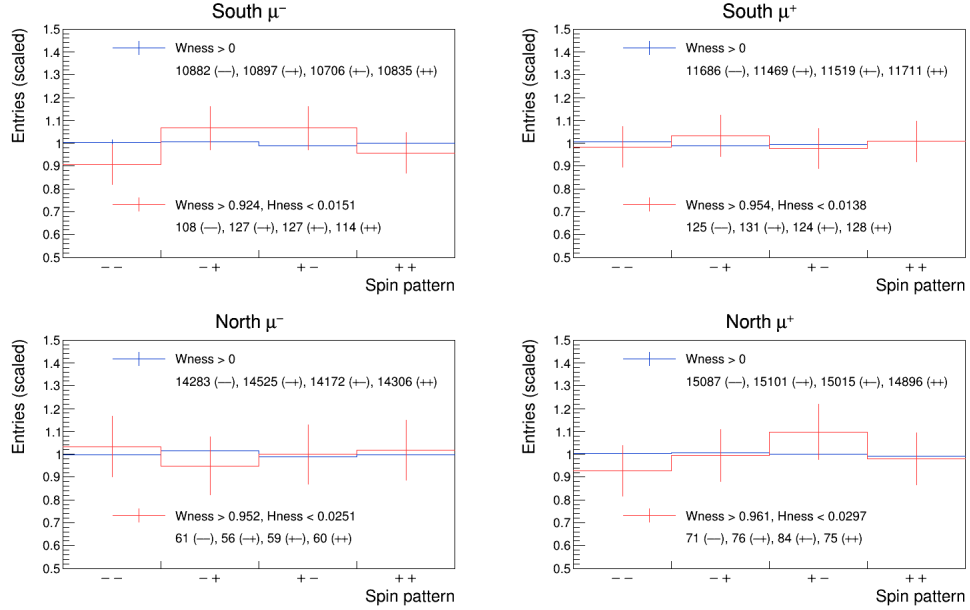


Figure 4.30: Comparison of muon yields by its spin pattern: in backgrounds dominant condition (Blue) and in *Final candidates* condition (Red), respectively.

	South μ^-	South μ^+	North μ^-	North μ^+
$Wness$	0.924	0.954	0.952	0.961
$Hness$	0.015127	0.013838	0.025144	0.029747
$\langle \eta \rangle$	-1.714	-1.693	1.798	1.759
Entries	476	508	236	306
n_{sig}	121^{+23}_{-22}	116^{+23}_{-23}	32^{+15}_{-14}	55^{+16}_{-15}
n_{mbg}	208	179	123	113
n_{hbg}	133^{+15}_{-14}	172^{+20}_{-19}	64^{+11}_{-10}	106^{+12}_{-12}
S/BG	$0.355^{+0.085}_{-0.077}$	$0.331^{+0.089}_{-0.078}$	$0.170^{+0.095}_{-0.081}$	$0.250^{+0.090}_{-0.078}$
$\epsilon_{L, B}$	$+0.0126 \pm 0.0461$	-0.0079 ± 0.0445	$+0.0085 \pm 0.0654$	$+0.0392 \pm 0.0583$
$\epsilon_{L, Y}$	$+0.0126 \pm 0.0461$	$+0.0197 \pm 0.0448$	-0.0169 ± 0.0656	-0.0131 ± 0.0575
ϵ_{LL}	-0.0672 ± 0.0474	$+0.0039 \pm 0.0445$	$+0.0254 \pm 0.0659$	-0.0458 ± 0.0585
$A_{L, B}$	$+0.0896^{+0.3301}_{-0.3307}$	$-0.0590^{+0.3347}_{-0.3351}$	$+0.1085^{+0.8385}_{-0.8431}$	$+0.3650^{+0.5635}_{-0.5802}$
$A_{L, Y}$	$+0.0838^{+0.3085}_{-0.3091}$	$+0.1380^{+0.3192}_{-0.3211}$	$-0.2028^{+0.7910}_{-0.8079}$	$-0.1136^{+0.5024}_{-0.5043}$
A_{LL}	$-0.8330^{+0.6817}_{-0.7079}$	$-0.0514^{+0.5808}_{-0.5809}$	$+0.5668^{+1.4926}_{-1.5619}$	$-0.7412^{+0.9978}_{-1.0366}$

Table 4.16: Parameters at *Final candidates* condition. Systematic uncertainties are not included.

4.3.3 Systematic Uncertainties

Residual transverse polarization The nominal direction of beam polarization in RHIC rings is vertical up or vertical down. For the longitudinal runs these vertical beam polarization is adjusted to parallel or antiparallel to the beam axis by Spin Rotators. Therefore it need to be confirmed that there's no residual transverse polarization when collision happens. For this purpose Local polarization at PHENIX is measured by ZDC and SMD. By collecting forward neutrons left-right asymmetry (A_{LR}) and up-down asymmetry (A_{UD}) can be defined as follows.

$$A_{LR} = \frac{1}{P} \cdot \frac{\sqrt{N_L^\uparrow N_R^\downarrow} - \sqrt{N_L^\uparrow N_R^\downarrow}}{\sqrt{N_L^\uparrow N_R^\downarrow} + \sqrt{N_L^\uparrow N_R^\downarrow}}, \quad A_{UD} = \frac{1}{P} \cdot \frac{\sqrt{N_U^\uparrow N_D^\downarrow} - \sqrt{N_U^\uparrow N_D^\downarrow}}{\sqrt{N_U^\uparrow N_D^\downarrow} + \sqrt{N_U^\uparrow N_D^\downarrow}} \quad (4.22)$$

$$A_N = \sqrt{A_{LR}^2 + A_{UD}^2} \quad (4.23)$$

With above asymmetries measured in longitudinal (P_{\parallel}) runs and transverse (P_{\perp}) runs, the transverse component of the beam can be extracted as follows.

$$\frac{P_T}{P} = \sqrt{\left(\frac{A_{LR,\parallel}}{A_{N,\perp}}\right)^2 + \left(\frac{A_{UD,\parallel}}{A_{N,\perp}}\right)^2} \quad (4.24)$$

Following list shows the results of Local polarimetry in recent data taking periods. The Local polarization analysis for Run 12 is currently ongoing. As the residual transverse polarization is negligibly small, it is regarded the error will be negligibaly small as well.

- 2009 ($\langle P_{\parallel} \rangle$) [35]

- o B: $0.994^{+0.006}_{-0.008}$ (stat) $^{+0.003}_{-0.010}$ (syst)
- o Y: $0.974^{+0.014}_{-0.018}$ (stat) $^{+0.019}_{-0.035}$ (syst)

- 2011 ($\langle P_{\perp} \rangle$) [35]

- o B: 0.060 ± 0.004
- o Y: 0.054 ± 0.002

- 2013 ($\langle P_{\parallel} \rangle$) [36]

- o B: $0.998814^{+0.000386}_{-0.000436}$ (stat) $^{+0.000334}_{-0.000000}$ (syst1) ± 0.000155 (syst2)
- o Y: $0.999973^{+0.000027}_{-0.000038}$ (stat) $^{+0.000000}_{-0.000043}$ (syst1) ± 0.000008 (syst2)

Transverse momentum smearing There exist large smearing in the determination of p_T^{reco} ($\sigma \Delta p_T^{reco}$) due to the limited position resolution of MuTr. Since W signals are dominant in the range of $10 < p_T^{reco} < 40$ (GeV/c), this p_T smearing induces large backgrounds in addition to the misidentification of W signals.

To quantify the size of smearing a specific analysis was performed by using cosmic muons collected in Run 11[12]. According to the analysis results the $\sigma \Delta p_T^{reco}$ increases with p_T^{reco} up to ~ 15 GeV for the range of $p_T^{reco} < 40$ GeV (Fig. 4.31).

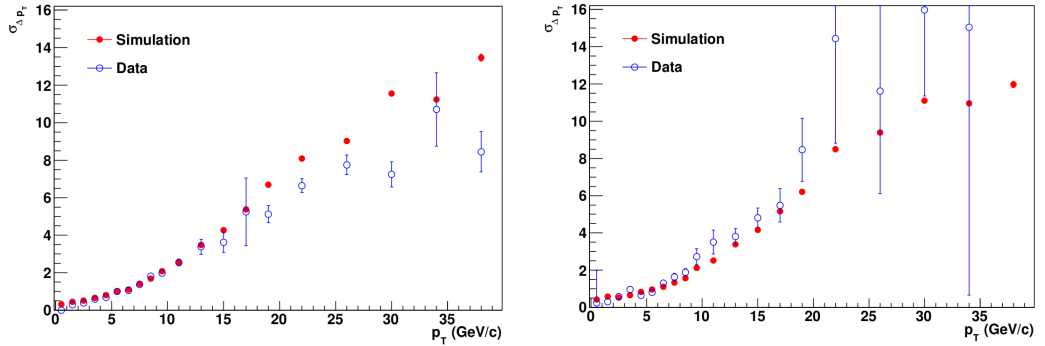


Figure 4.31: Results of transverse momentum smearing ($\sigma \Delta p_T$) study by cosmic muons collected in Run 11. Left plot shows result for the negative charged muons and Right plot shows result for the positive charged muons. These plots are quoted from [12].

The effect of the p_T smearing on the A_L can be evaluated by creating special MC samples tuned by MuTr's position resolution: the tune is done by adjusting MuTr cathode strips' noise RMS scale. The default RMS scale is 1.0 and all MC samples used in this analysis are produced by this setup, however, according to the cosmic muons study best match between the data and the MC was found in the RMS scale of 0.92. To measure the uncertainty by the smearing, one need to produce MC samples with various RMS scale factors. Once the MC samples produced the effect of smearing can be corrected by following equation [7].

$$\left(\frac{1}{p_T^{reco}} \right)_{\alpha}' = \left(\frac{1}{p_T^{true}} \right) + \alpha \left[\left(\frac{1}{p_T^{reco}} \right) - \left(\frac{1}{p_T^{true}} \right) \right] \quad (4.25)$$

$$\alpha = 0.492 + 0.507 \times \text{RMS scale (South)}, 0.482 + 0.517 \times \text{RMS scale (North)}$$

By using this setup, the effect of momentum smearing on the S/BG ratio in the $W_{ness} > 0.99$ is studied by analyzer Sanghwa Park [29]. According to the results the S/BG ratio of the dataset varies up to 0.158. By referring this result the systematic uncertainty is measured and assigned by applying ± 0.2 difference on measured S/BG ratio of *Final candidates*. The results are summarized in following Table 4.19.

	South μ^-	South μ^+	North μ^-	North μ^+
$\delta A_{L,B}$	0.0238	0.0167	0.0510	0.1296
$\delta A_{L,Y}$	0.0223	0.0391	0.0936	0.0403
δA_{LL}	0.2214	0.0146	0.2616	0.2633

Table 4.17: Systematic errors in *Final candidates* condition induced by $\sigma \Delta p_T^{reco}$.

Muonic backgrounds As explained in section 4.2.5 the yields of muonic backgrounds are fixed during the EUML fit under the assumption of dominant muonic backgrounds generation processes are well verified.

In the process of getting the muonic yields, a few additional scaling factors are applied to the muonic backgrounds MC in addition to the luminosity scaling: k factor, overall trigger efficiency (Table 4.10), and di-muon scaling factors (Table 4.11). However these additional scaling factors except k-factor are only known with uncertainties. These uncertainties propagate to the processes of A_L estimation and works as a systematic uncertainty. Especially for the case of di-muon scaling factors, each subprocess has correlation to the other processes thus covariance among the processes should be considered by following equation:

$$\delta A_{L, scale} = \sqrt{\sum_i \sum_j \delta A_{L, i} \cdot cov(i, j) \cdot \delta A_{L, j}} \quad (4.26)$$

where the $\delta A_{L, i(j)}$ indicates uncertainty of A_L induced by a process of di-muon scaling factor (ex. Υ). The covariance among each process can be found in Table 4.12.

The measured uncertainties are summarized in following Table 4.18.

	South μ^-			South μ^+		
	$\delta A_{L, B}$	$\delta A_{L, Y}$	δA_{LL}	$\delta A_{L, B}$	$\delta A_{L, Y}$	δA_{LL}
$\epsilon_{trig OA}$	0.0051	0.0048	0.0473	0.0006	0.0014	0.0005
Open b	0.0171	0.0159	0.1581	0.0048	0.0113	0.0042
Open c	0.0044	0.0041	0.0409	0.0007	0.0016	0.0006
Υ	0.0011	0.0010	0.0099	0.0002	0.0005	0.0002
$Z \rightarrow \mu, Z/DY$	0.0013	0.0012	0.0116	0.0007	0.0017	0.0006
Total	0.0139	0.0130	0.1288	0.0038	0.0089	0.0033

	North μ^-			North μ^+		
	$\delta A_{L, B}$	$\delta A_{L, Y}$	δA_{LL}	$\delta A_{L, B}$	$\delta A_{L, Y}$	δA_{LL}
$\epsilon_{trig OA}$	0.0115	0.0214	0.0598	0.0307	0.0096	0.0623
Open b	0.0546	0.1021	0.2851	0.0660	0.0206	0.1339
Open c	0.0137	0.0256	0.0713	0.0153	0.0048	0.0310
Υ	0.0024	0.0045	0.0124	0.0034	0.0011	0.0068
$Z \rightarrow \mu, Z/DY$	0.0050	0.0094	0.0261	0.0114	0.0036	0.0231
Total	0.0424	0.0791	0.2212	0.0554	0.0172	0.1123

Table 4.18: Systematic errors in *Final candidates* condition induced by muonic backgrounds scaling factors.

Hadronic backgrounds In this analysis the PDF of hadronic backgrounds for the EUML fit is driven from the data (section 4.2.5). The hadronic backgrounds is abundant in all W_{ness} : even for the $W_{ness} > 0.9$ condition the hadronic backgrounds abundance is roughly $> \sim 50\%$. In addition to this abundance, by using the $H_{ness_{opt}}$ the safe selection of hadronic backgrounds-like events is possible with small chance of signal contamination. Therefore it is assumed that the hadronic backgrounds so far is extracted with reasonable uncertainty.

However there are a couple of weaknesses in current data driven method. First, the composition of hadronic BG is based on fixed $W_{ness} > 0.9$ with its $H_{ness_{opt}}$. Though it is doubtful that the hadronic backgrounds distribution dramatically changes in the range of $W_{ness} > 0.9$, at the same time the distribution won't be exactly same for the $W_{ness} > 0.9$ and $W_{ness} > 0.99$, neither. However selective hadronic backgrounds composition by the W_{ness} is not appropriate due to the limited statistics of hadron-like events among high W_{ness} muon candidates. Second, the H_{ness} cannot distinguish muonic backgrounds due to its characteristic: as it judges only if the event is more or less likely signal or hadronic backgrounds, there is a possibility of muonic backgrounds contamination in current hadronic backgrounds PDF.

Before the current data driven method by H_{ness} , several other methods were tested to extract the reliable hadronic backgrounds distribution. One of them is getting hadronic backgrounds' distribution directly from the hadronic backgrounds MC. This methods didn't used for this analysis due to the scarce statistics of hadronic MC in $W_{ness} > 0.9$, however, it can be used in the purpose of crosscheck to the current data-driven method. Therefore this hadronic MC method is applied to the analysis chain and its effect to the A_L is estimated. The following table shows δA_L obtained by comparing central value of A_L of each methods.

	South μ^-	South μ^+	North μ^-	North μ^+
$\delta A_{L,B}$	0.0124	0.0178	0.0318	0.1186
$\delta A_{L,Y}$	0.0116	0.0417	0.0594	0.0369
δA_{LL}	0.1152	0.0155	0.1661	0.2409

Table 4.19: Systematic errors in *Final candidates* condition induced by the method of hadronic backgrounds PDF composition.

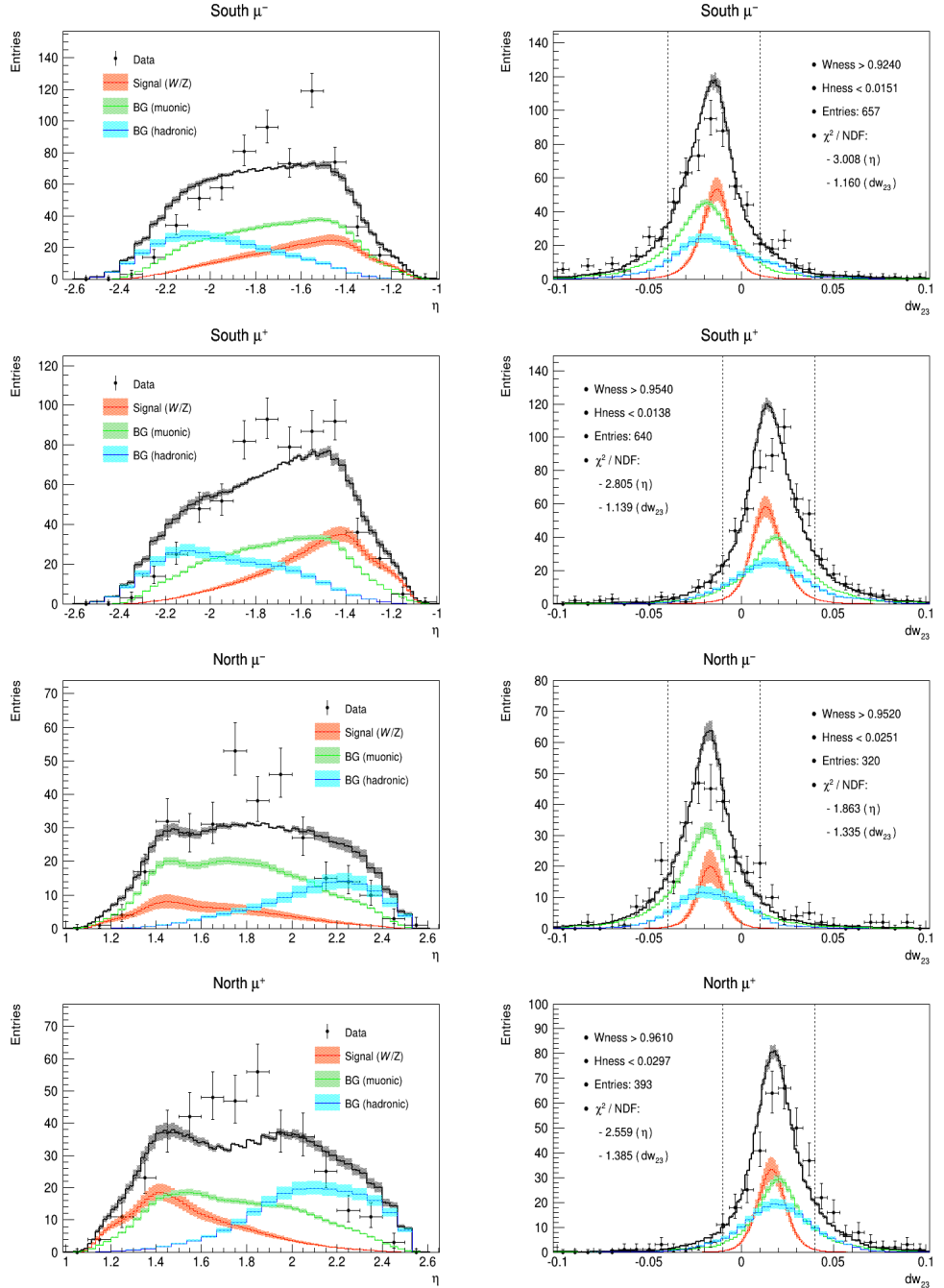


Figure 4.32: EUML fit results by hadronic backgrounds PDF composed of hadronic MC samples. The other conditions are same to the Fig. 4.29.

Intrinsic asymmetry The definition of A_L in Eq. 4.18 is based upon a premise that no intrinsic asymmetry exist in the dataset. If such intrinsic asymmetry actually exist it must be corrected in the final A_L to separate it from the A_L originated from W s. Therefore a couple of possible intrinsic asymmetry sources are tested.

First, there can be an intrinsic asymmetry from Spin patterns itself by certain systematic condition. To check this possibility the bunch shuffling technique is used. By randomizing the bunch crossing ID or Spin pattern of the events the possible A_L distribution of the dataset can be obtained. If there exist any intrinsic A_L it will arise as shifted mean position in the Gaussian distribution. At the same time the reliability of the assigned uncertainty (Eq. 4.20) can be checked as well: if the assigned uncertainty is inappropriate the FWHM of the $A_L/\Delta A_L$ distribution will be very different from 1. In conclusion the test is performed by shuffling Spin patterns of the dataset in Table 4.16 and the results can be checked in Fig. 4.33. No intrinsic asymmetry is found and it is confirmed that the uncertainties are reasonably assigned within 1σ variance (68 % C.L.).

Second, during the estimation of A_L for a beam, the other beam polarization is averaged over. For example, in the estimation of $A_{L,B}$ the polarization of Yellow beam is averaged over under the assumption of it cancel itself out. However if the magnitude of averaged beam polarization is substantial, it will affect measured A_L in the form of the A_{LL} is added on. Therefore the sum of beam polarization is checked for the dataset in Table 4.16. The results are summarized in Table 4.20. As the maximum value is smaller than the error of average beam polarization it is regarded that the effect is negligible.

	$\int \langle P_B \rangle$ in $A_{L,Y}$ estimation	$\int \langle P_Y \rangle$ in $A_{L,B}$ estimation
South μ^-	+ 0.68 (%)	+ 2.29 (%)
South μ^+	+ 1.06 (%)	- 0.11 (%)
North μ^-	- 0.91 (%)	- 0.49 (%)
North μ^+	- 0.70 (%)	+ 2.44 (%)

Table 4.20: Net remaining beam polarization in the A_L estimation.

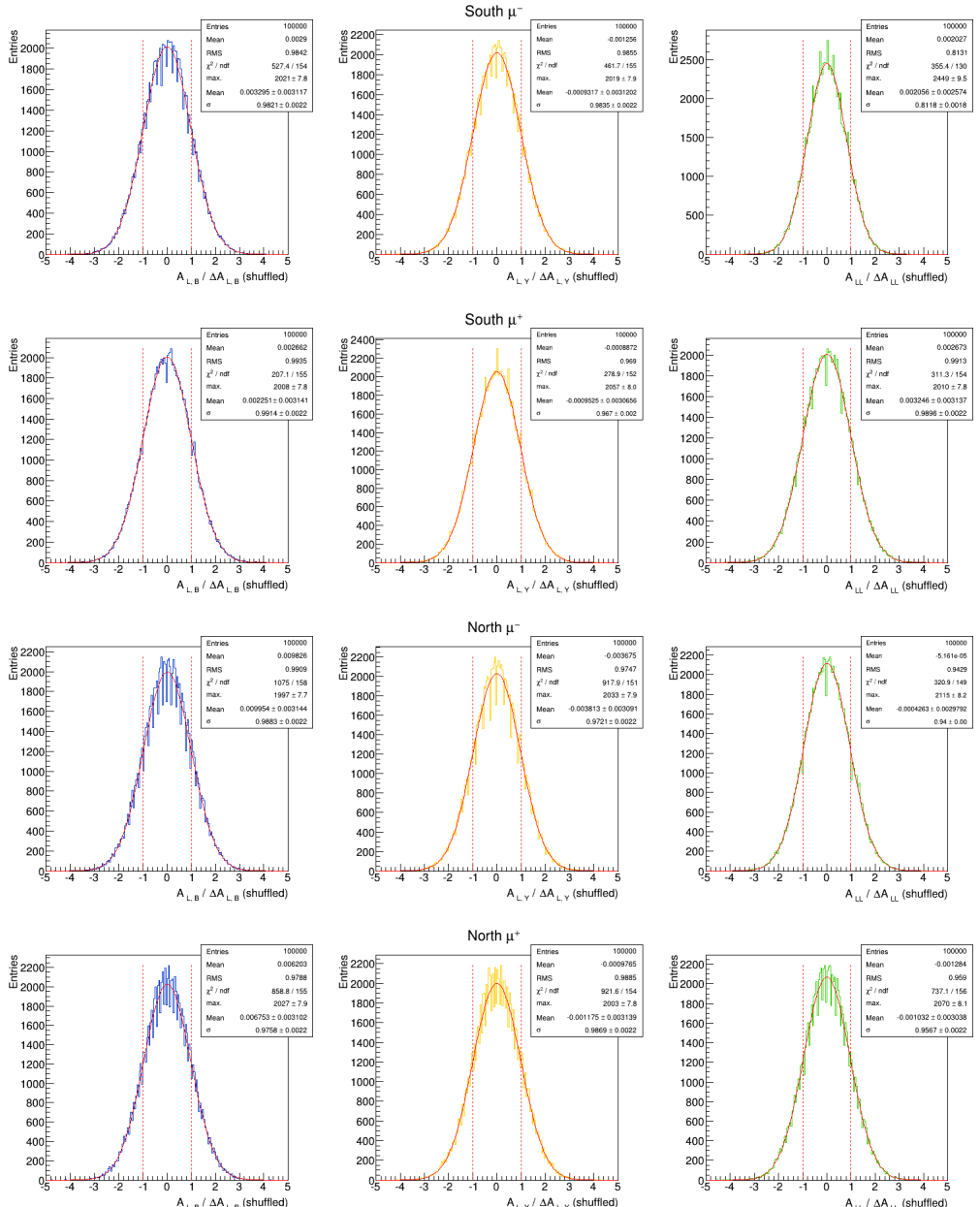


Figure 4.33: Results of spin pattern shuffling to the *Final candidates*. Each column shows shuffled $\frac{A_{L,B}}{\Delta A_{L,B}}$ (left), $\frac{A_{L,Y}}{\Delta A_{L,Y}}$ (middle), and $\frac{A_{LL}}{\Delta A_{LL}}$ (right), respectively.

4.3.4 Results

The final results of the $W \rightarrow \mu$ analysis are summarized in following two tables: Table 4.21 shows summary and synthesis of non-negligible systematic uncertainties and Table 4.22 shows summary of beam separated or combined A_L including systematic uncertainties, respectively.

Err _{syst} (S)	South μ^-			South μ^+		
	Wness > 0.924			Wness > 0.954		
	$\delta A_{L,B}$	$\delta A_{L,Y}$	δA_{LL}	$\delta A_{L,B}$	$\delta A_{L,Y}$	δA_{LL}
$\sigma \Delta p_T^{reco}$	0.0238	0.0223	0.2214	0.0167	0.0391	0.0146
Muonic BG	0.0139	0.0130	0.1288	0.0038	0.0089	0.0033
Hadronic BG	0.0124	0.0116	0.1152	0.0178	0.0417	0.0155
Total	0.0302	0.0283	0.2809	0.0247	0.0579	0.0215

Err _{syst} (N)	North μ^-			North μ^+		
	Wness > 0.952			Wness > 0.961		
	$\delta A_{L,B}$	$\delta A_{L,Y}$	δA_{LL}	$\delta A_{L,B}$	$\delta A_{L,Y}$	δA_{LL}
$\sigma \Delta p_T^{reco}$	0.0510	0.0936	0.2616	0.1296	0.0403	0.2633
Muonic BG	0.0424	0.0791	0.2212	0.0554	0.0172	0.1123
Hadronic BG	0.0318	0.0594	0.1661	0.1186	0.0369	0.2409
Total	0.0736	0.1362	0.3807	0.1842	0.0573	0.3741

Table 4.21: Summary of studied systematic errors.

Type	Arm	Beam	$\langle \eta \rangle$	$A_L \pm (stat) \pm (syst)$	Combined A_L
<i>FW</i> μ^-	South	Y	-1.714	$+0.084^{+0.309}_{-0.309} \pm 0.028$	$+0.096^{+0.445}_{-0.449} \pm 0.079$
	North	B	+1.798	$+0.109^{+0.839}_{-0.843} \pm 0.074$	
<i>BW</i> μ^-	South	B	-1.714	$+0.090^{+0.330}_{-0.331} \pm 0.030$	$-0.057^{+0.429}_{-0.436} \pm 0.140$
	North	Y	+1.798	$-0.203^{+0.791}_{-0.808} \pm 0.136$	
<i>FW</i> μ^+	South	Y	-1.693	$+0.138^{+0.319}_{-0.321} \pm 0.058$	$+0.252^{+0.324}_{-0.332} \pm 0.193$
	North	B	+1.759	$+0.365^{+0.564}_{-0.580} \pm 0.184$	
<i>BW</i> μ^+	South	B	-1.693	$-0.059^{+0.335}_{-0.335} \pm 0.025$	$-0.086^{+0.302}_{-0.303} \pm 0.062$
	North	Y	+1.759	$-0.114^{+0.502}_{-0.504} \pm 0.057$	

Table 4.22: Final A_L with systematic uncertainty.

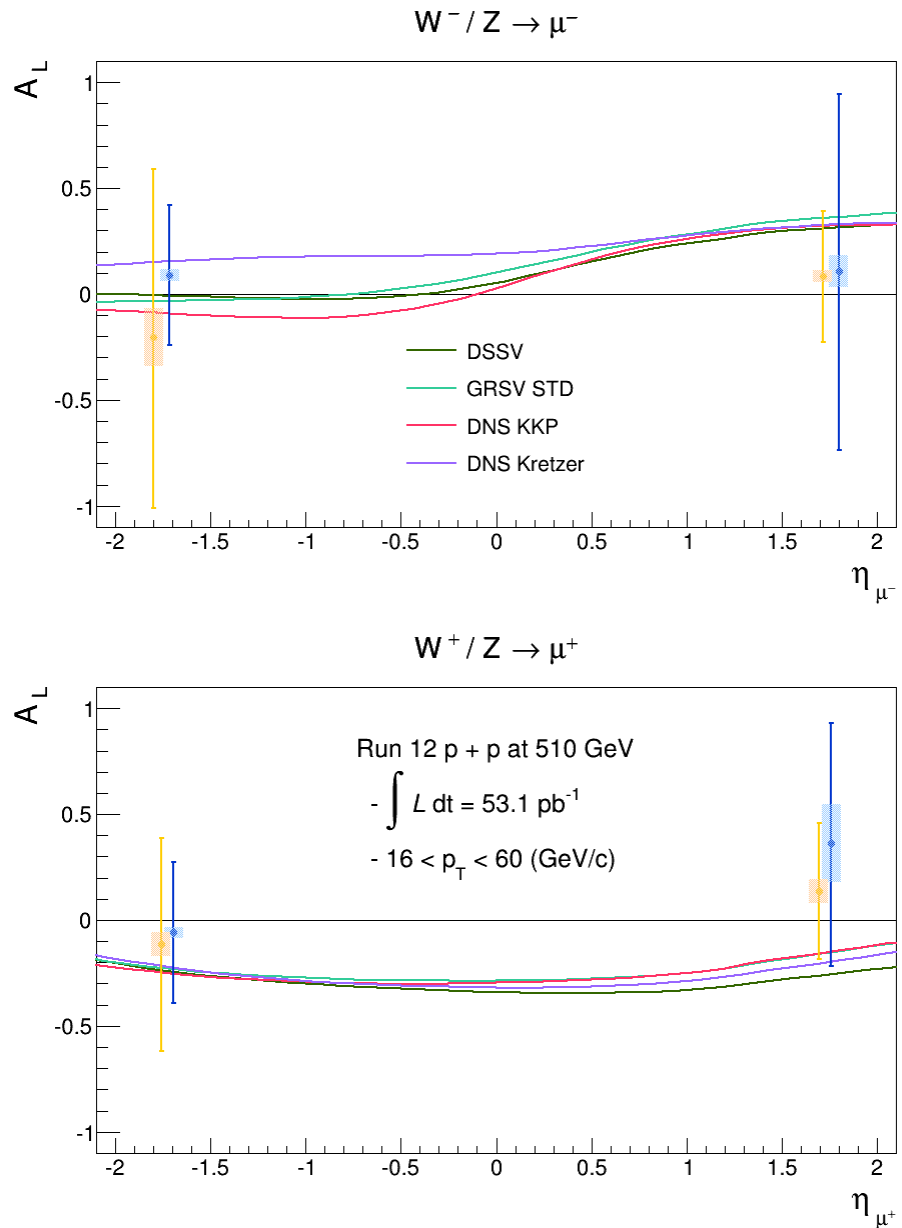


Figure 4.34: Final beam separated A_L results. The sign of horizontal axis indicates the asymmetry measured in either forward (positive) or backward (negative) with respect to the beam going direction.

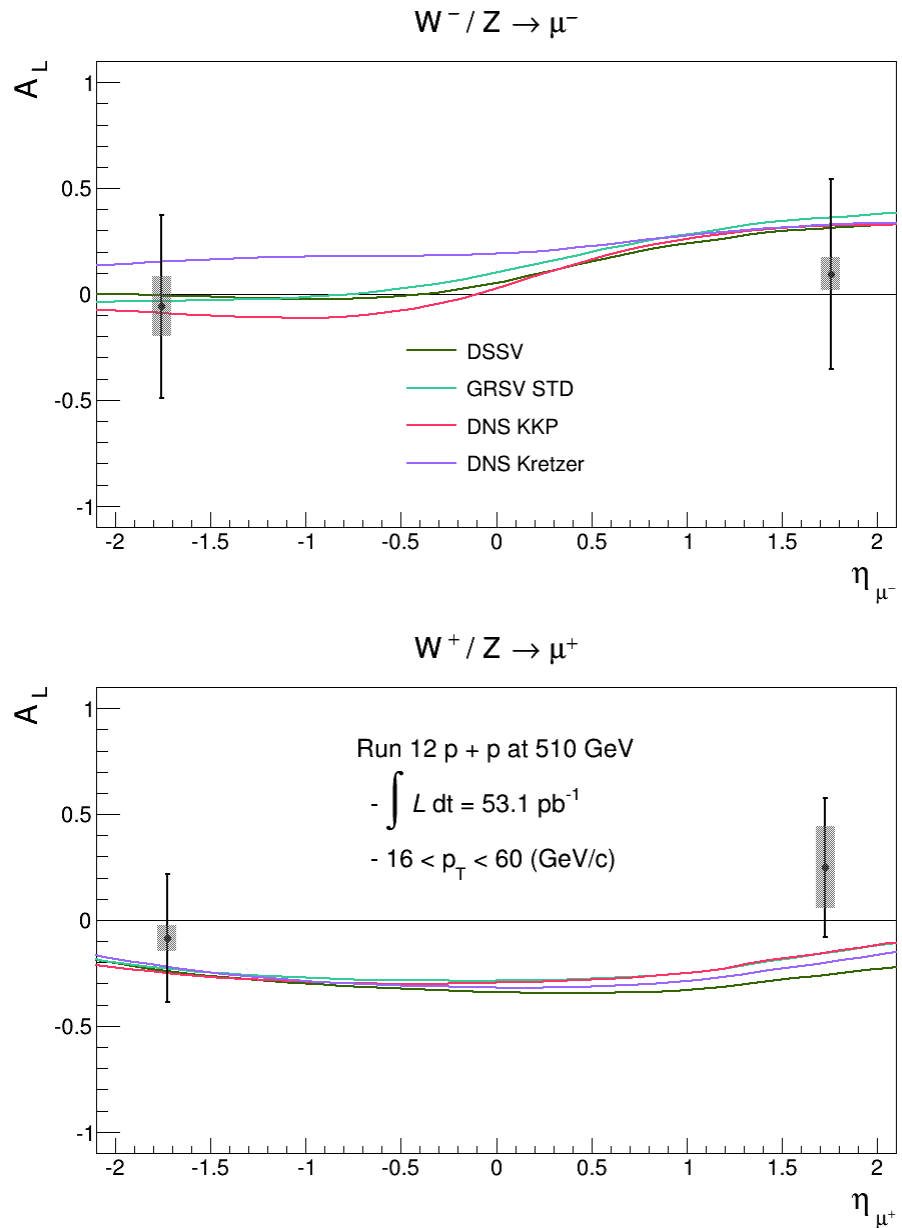


Figure 4.35: Final combined A_L results. The sign of horizontal axis indicates the asymmetry measured in either forward (positive) or backward (negative) with respect to the beam going direction.

4.4 Discussion and Conclusion

4.4.1 Discussion

Systematic uncertainties The major sources of overall systematic uncertainty are not very different from previous analysis results ([7], [29]): p_T^{reco} smearing from the MuTr's position resolution, scaling factors applied on muonic background determination, and the composition of hadronic backgrounds PDF for the EUML fit, respectively.

The MuTr's position resolution is $\sim 150 \mu\text{m}$ after the installation or MuTRG: it is $\sim 30\%$ degraded resolution compared to the one before the MuTRG upgrade [7]. So far two possible improvements are discussed in order to recover the resolution in the level of $\sim 100 \mu\text{m}$. One method is the calibration of the Mathison function: as MuTr track reconstruction relies on the charge distribution fit by using the Mathison function, if the resolution can be recovered by successful recalibration it will certainly give an edge. The other method is offline alignment of the MuTr. By the analyzer Jin Huang MuTr's alignment status was studied and re-aligned in 2014 by using the $W \rightarrow \mu$ dataset collected in 2013 Run. Although it showed noticeable improvements in kinematic variables the effect on the W_{ness} was relatively small thus application on Run 12 dataset is not clear.

For the case of muonic backgrounds' scaling factors, the precision of fit on high p_T region was relatively low due to the scarce statistics of Υ s. Though the current results already constrain muonic backgrounds fairly well, if the fit's precision can be further enhanced the overall systematic background will decrease as well.

Lastly, more than three methods were already developed and tested in order to determine reliable hadronic backgrounds distribution in signal dominant region ($W_{ness} > 0.92$). Though the H_{ness} based method adapted in this thesis shows fairly good EUML fit results, the possibility of the improvements by the other methods cannot be ignored, either. Currently 3 other methods are under the study: the traditional extrapolation method, updated extrapolation method by using non-linear fit function, and the extrapolation by using Gaussian process regression, respectively.

Originality of the analysis This analysis basically follows the same analysis framework defined in Run 11 $W^\pm \rightarrow \mu^\pm$ analysis. However, a couple of original updates were developed and tested on this analysis: multiple collision condition reflected W_{ness} and hadronic likelihood H_{ness} , respectively.

Traditional W_{ness} refers only the *high* multiple collision condition in the determination of the W_{ness} . However, as shown in Fig. 4.10 there exist apparent discrepancy in each kinematic variables' distribution by the multiple collision condition. In ad-

dition the contribution of *high* condition events among entire dataset are smaller than $\sim 25\%$. This analysis is first and only $W^\pm \rightarrow \mu^\pm$ analysis in forward Muon Arms with event by event multiple collision consideration. As a result of this update, noticeable decrease of ambiguous events ($Wness \sim 0.5$) was observed.

Define and Use of the *Hness* is another originality of this analysis. As another likelihood which can be used in both backgrounds rejection and backgrounds-like event selection, the *Hness* enables the two-dimensional judgment for an event. Especially the A_L scan vs. $Wness$ (Fig. 4.28) with peak proves reliability of the EUML fit by the *Hness* method.

Future prospects As discussed in systematic uncertainties major sources of the uncertainty are the signal-mimic backgrounds. As the statistical uncertainty is amplified by the S/BG ratio of the sample the backgrounds among the sample need to be suppressed as much as possible.

Aside from the analytical improvement discussed in systematic uncertainties additional backgrounds rejection with new detector was proposed recently [37]. The idea is install additional tungsten-scintillator sampling hadronic calorimeter at Upstream absorber's Cu nosecone. Although the design parameters need to be studied carefully, the dE/dx cut and charge isolation cut by hadronic calorimeter will give an edge on low p_T fakes' rejection as well as jet rejection.

Lastly, the 2013 data taking period at RHIC was dedicated Run for the W measurement. The total integrated luminosity of Run 13 $W^\pm \rightarrow \mu^\pm$ is 277.1 pb^{-1} , which is ~ 5.2 times rich statistics than Run 12 with fully working W triggers. Therefore a noticeable improvement in sea-quark polarization constraint can be expected with further updates from Run 13.

4.4.2 Conclusion

The sea-quark polarization of the proton is probed by measuring longitudinal single spin asymmetry (A_L) in $W/Z \rightarrow \mu$ using polarized p + p collision at $\sqrt{s} = 510$ GeV. The final results and several important parameters related to this analysis are summarized in following list.

- Final A_L (beam combined)

- $A_L^{\mu^-}$ (FW) = $0.096^{+0.445}_{-0.449}$ (stat) ± 0.079 (syst), $\langle \langle \eta \rangle \rangle = 1.76$
- $A_L^{\mu^-}$ (BW) = $-0.057^{+0.429}_{-0.436}$ (stat) ± 0.140 (syst), $\langle \langle \eta \rangle \rangle = -1.76$
- $A_L^{\mu^+}$ (FW) = $0.252^{+0.324}_{-0.332}$ (stat) ± 0.193 (syst), $\langle \langle \eta \rangle \rangle = 1.73$
- $A_L^{\mu^+}$ (BW) = $-0.086^{+0.302}_{-0.303}$ (stat) ± 0.062 (syst), $\langle \langle \eta \rangle \rangle = -1.73$

- Data

- $W^\pm/Z \rightarrow \mu^\pm$ from polarized p + p at $\sqrt{s} = 510$ GeV
- Average beam polarization: $\langle P_B \rangle = 0.536 \pm 0.041$, $\langle P_Y \rangle = 0.574 \pm 0.043$
- Detector acceptance: $1.2 < \eta < 2.2$ (S), $1.2 < \eta < 2.4$ (N) with 2ϕ in azimuth
- $\int L dt = 53.1$ (pb $^{-1}$)
- $16 < p_T^{reco} < 60$ (GeV/c)

- Major challenges

- Kinematical characteristic of W at forward rapidity
- Limited acceptance (non-hermitian structure)
- Large smearing in p_T^{reco} by low tracking resolution
- Backgrounds abundance

- Characteristics of the analysis

- Multivariate analysis based on W likelihood (W_{ness}) and hadron likelihood (H_{ness})
- S/BG extraction via extended unbinned max. likelihood fit
- Direct muonic BG yields estimation by MC
- Data driven hadronic backgrounds PDF composition
- Refined W likelihood by considering multiple collision condition

Bibliography

- [1] D. de Florian, R. Sassot, M. Stratmann, and W. Vogelsang, Phys. Rev. D **80**, 034030 (2009).
- [2] D. de Florian and W. Vogelsang, Phys. Rev. D **81**, 094020 (2010).
- [3] RHIC Spin Group - Polarimetry, <https://wiki.bnl.gov/rhicspin/Polarimetry> (2014).
- [4] T. Roser *et al.*, eds., *Accelerating and Colliding Polarized Protons in RHIC with Siberian Snakes* (EPAC Paris, France, 2002).
- [5] I. Alekseev *et al.*, *Configuration Manual Polarized Proton Collider at RHIC* (2006).
- [6] J. Tojo *et al.*, Phys. Rev. Lett **89**, 052302 (2002).
- [7] Hideyuki Oide, *Measurement of longitudinal spin asymmetry in production of muons from W/Z boson decays in polarized p+p collisions at $\sqrt{s} = 500$ GeV with the PHENIX detector at RHIC*, Ph.D. thesis, University of Tokyo (2012).
- [8] Michael Beaumier, Francesca Giordano, Richard Hollis, Chong Kim, Sanghwa Park, Ralf Seidl, PHENIX analysis note 1103 (2013).
- [9] Kenichi Karatsu, *Measurement of Cross Section and Single Spin Asymmetries of W^\pm -Boson Production in Polarized pp Collisions at $\sqrt{s} = 500$ GeV*, Ph.D. thesis, Kyoto University (2011).
- [10] P. R. . Homepage, <https://www.phenix.bnl.gov/WWW/run/12/> (2012).
- [11] Michael Beaumier, Francesca Giordano, Richard Hollis, Daniel Jumper, Abraham Meles, Ralf Seidl, PHENIX analysis note 1195 (2014).
- [12] Xiaochun He, Murad Sarsour, PHENIX analysis note 1014 (2012).
- [13] Particle Data Group, Chinese Physics C **38**, 090001 (2014).

- [14] RHIC Run Overview, <http://www.rhichome.bnl.gov/RHIC/Runs/index.html#Run-12> (2014).
- [15] Particle Data Group, <http://pdg.lbl.gov/2014/AtomicNuclearProperties/> (2015 Aug).
- [16] B. Hong, Nucl. Instrum. Meth **A602**, 644 (2009).
- [17] R. Towell, Nucl. Instrum. Meth **A602**, 705 (2009).
- [18] A. Zelenski *et al.*, Hyperfine Interactions **127**, 475 (2000).
- [19] Andrew Manion, *Double Longitudinal Helicity Asymmetries in Pion Production from Proton Collisions, Studies of Relative Luminosity Determination, and the Impact on Determination of the Gluon Spin in the Proton*, Ph.D. thesis, Stony Brook University (2014).
- [20] V. Bargmann, L. Michel, and V. L. Telegdi, Phys. Rev. Lett. **2**, 435 (1959).
- [21] A. Zelenski *et al.*, Nucl. Instrum. Meth **A536**, 248 (2005).
- [22] H. Akikawa *et al.*, Nucl. Instrum. Meth **A499**, 537 (2003).
- [23] T. Nakamura, <http://www.phenix.bnl.gov/WWW/run/03/focus/index.html> (2003).
- [24] C. Aidala *et al.*, arXiv 1311.3594 (2014).
- [25] PHENIX magnet, http://www.phenix.bnl.gov/WWW/magnet/magnet_home.html (2003 Apr).
- [26] S. Adachi *et al.*, Nucl. Instrum. Meth **A703**, 114 (2013).
- [27] Michael Beaumier, Richard Hollis, Sanghwa Park, Ralf Seidl, PHENIX analysis note 1102 (2013).
- [28] Amaresh Datta, David Kawall, PHENIX analysis note 888 (2010).
- [29] Sanghwa Park, *Measurement of the Single Spin Asymmetry in W Boson Production in Polarized p+p collisions at $\sqrt{s} = 510$ GeV with the PHENIX Muon Spectrometer*, Ph.D. thesis, Seoul National University (2015).
- [30] IhnJea Choi, Richard Hollis, Yoshimitsu Imazu, Martin Leitgab, Hideyuki Oide, Murad Sarsour, Joseph Seele, Ralf Seidl, PHENIX analysis note 1024 (2012).
- [31] Torbjorn Sjostrand, Stephen Mrenna, Peter Skands, JHEP **0605** (2006).
- [32] Elke Aschenauer, John Lajoie, Richard Seto, PHENIX analysis note 862 (2009).

- [33] Wouter Verkerke and David Kirkby, <http://roofit.sourceforge.net> (2005).
- [34] RHIC Polarimetry Results by Fill, <http://www.phy.bnl.gov/cnopol/fills/> (2015 May).
- [35] Ciprian Gal, *Measuring the anti-quark contribution to the proton spin using parity violating W production in polarized proton proton collisions*, Ph.D. thesis, Stony Brook University (2014).
- [36] Minjung Kim, PHENIX analysis note 1190 (2014).
- [37] Mickey Chiu, <https://www.phenix.bnl.gov/cdsagenda/fullAgenda.php?id=a14729> (2015 Dec).

Acknowledgement

Though there are so many good teachers and friends I want to express my sincere gratitude I want to appreciate three particular peoples in this page. For the others I plan to say thanks in person.

First of all, I appreciate my advisor Dr. Byungsik Hong. I continually received his teaching from the very start of the reaserch in this field in 2007. During the 8 years of the teachings he gave me every support I need in both materially and emotionally. All I can say about him is he is a person deserve to be a role model, not only as a scholar but also as a man of character. I hope someday I find myself became a person like him.

Also I appreciate Dr. Ralf Seidl. As a senior resercher in RIKEN he was another mentor in my Ph.D course. I learned every knowledge about the *W* analysis from him. His knowledge, initiative, and drive showed me an another model of professional researcher.

Lastly I appreciate my family, especially my mother. I'm always a brusque son to you but I really love you in my heart. Even if I don't express this in voice please know I am your proud son who loves you deeply.